Iron Based Metal Organic Frameworks as Photocatalysts for Chromium (VI) Degradation

Bachelor's Thesis

in Chemistry

Submitted to the
Faculty of Science
of the
University College Utrecht

in Partial Fulfillment of the Requirement for the Degree of
Bachelor of Science

by
Deliana Dimitrova
3901599

Supervisor
dr. Monica Barroso Silva da Cruz
Department of Inorganic Chemistry and Catalysis
University Utrecht

Spring 2015

Iron Based Metal Organic Frameworks as Photocatalysts for Chromium (VI) Degradation

Deliana Dimitrova[1]*

Abstract
The photocatalytic reduction of Cr(VI) is investigated over iron(III) based metal-organic frameworks (MOFs) with the structures NH_2-MIL-88B(Fe) and NH_2-MIL-101(Fe). The only parameter which leads to a different structure is the molar ratio of metal to ligand. If the molar ratio is the same, the structure NH_2-MIL-88B(Fe) is formed, whereas if the molar ratio is different, the structure NH_2-MIL-101(Fe) is formed. Although the photocatalysts have different structures, they are both able to reduce Cr(VI) dye under visible light irradiation. NH_2-MIL-101(Fe) has a higher efficiency compared to NH_2-MIL-88B(Fe), which is likely attributed to the MOF's higher crystallinity and different structure. Additionally, a higher metal to ligand ratio in the NH_2-MIL-101(Fe) photocatalyst leads to the highest efficiency compared to other NH_2-MIL-101(Fe) photocatalysts. NH_2-MIL-101(Fe) can be used as an efficient photocatalyst for the degradation of the toxic heavy metal, Cr(VI). This finding can ultimately lead to the development of a novel and effective method for wastewater treatment.

Keywords
MOF — Photocatalysis — Dye degradation — Environmental Remediation — Hexavalent Chromium

[1] *University College Utrecht, Utrecht, the Netherlands*
*__Supervisor__: dr. Monica Barroso Silva da Cruz, Department of Inorganic Chemistry and Catalysis, University Utrecht

Introduction

Contaminated natural wastewater with synthetic dyes as well as toxic heavy metal ions has become a prominent issue in modern society in the last few decades [1]. Hexavalent chromium, or Cr(VI), has become listed as one of the top priority pollutants by the U.S. Environmental Protection Agency [2]. This is due to the fact that this particular heavy metal ion has been found to have toxic effects [3]. Only slight levels of hexavalent chromium in the environment have been found to be directly toxic to bacteria, plants, and animals [4, 5]. Additionally, this heavy metal has been found to be carcinogenic in human beings.[2] It is mainly released into the environment by a variety of industries including steel manufacturing, leather tanning, wood preservation, fossil fuel combustion, and others. Approximately 75,000 tons (1.3 x 10^9 mol) of chromium is released into the atmosphere by these sources, and approximately one-third of this chromium is the toxic hexavalent species [6]. In effect, governmental institutions worldwide have implemented stricter laws for the control of wastewater contamination which has consequently fueled intense research into the field of novel water treatment technologies [7]. The dire need for effective water treatment technologies is also due to the fact that many of the heavy metals contaminating natural water sources have been shown to be poisonous or otherwise harmful on many forms of life [8]. The current methods for environmental rumination of Cr(VI) from wastewater are not optimal. Prior to releasing the wastewater into the environment, industries have adopted four most common methods of disposing or recovering metal ions that may be present in the water. These four techniques are chemical precipitation, membrane separation, adsorption, and ion exchange. However, these methods are costly, require large quantities of energy or chemicals, and are inefficient if used alone [9]. A preferred and more effective method for the treatment of Cr(VI) in wastewater is transforming it into its less toxic and non harmful oxidation state, Cr(III) [9, 7]. This reduction is highly attractive, since Cr(III) is mostly immobile and environmentally friendly. Its immobility allows it to be adsorbed on various substrates in neutral or alkaline solutions [10]. Additionally, Cr(III) plays an essential role in animal and plant metabolism. A dose of 0.1-0.3 ppm per day is in fact required for normal development [11, 9]. Thus, the reduction of Cr(VI) to Cr(III) has high potential in the field of industrial wastewater treatment.

A recently explored method for performing this reduction is by semiconductor photocatalysis [7]. The capability of photocatalysts to perform this reduction is based on the electron-hole pairs (e^--h^+) that are generated in the semiconductor materials when illuminated with light that is higher than the semiconductor's band gap. Once the electrons move to the surface of the semiconductor they are able to reduce Cr(VI) to Cr(III) in the solution [12]. A plethora of research for this reduction has been conducted using the semiconductor TiO_2 [13, 14, 15]. Unfortunately, TiO_2 has a wide band gap (3-3.2 eV) thus making it an inefficient photocatalyst because it can only harvest UV light[16].

Metal-organic frameworks (MOFs) are a newly explored fascinating class of porous coordination compounds. They are hybrid materials composed of metal clusters and organic link-

ers [17, 18, 19]. A wide variety of MOFs with different pore shapes, sizes, and framework compositions have been reported in the past decade. These interesting properties of MOFs allow them to have great potential in several applications such as gas storage, drug delivery, and for this research's purpose — photocatalysis [20]. MOFs are superior in comparison to traditional catalysts because of their desirable topology and high surface area which allows for accommodation of guest molecules [17]. Additionally, the HOMO-LUMO gap can easily be tuned through modification of the inorganic or organic units of the molecule during its synthesis [21]. Thus, efficient visible light harvesting can be achieved using MOFs.

The present research aims at synthesizing novel visible-light active photocatalysts with both high stability and photocatalytic activity for the reduction of Cr(VI). Little work has been done on this specific application of MOF [7]. These MOFs will be composed of an iron(III) or iron(II) metal node. Iron has recently become promising as a metal node because it is readily available, cheap, environmentally benign, non-toxic, and has redox properties [22]. In this field, the use of linear organic linkers, especially terephtalic acid, is very popular due to their ability to create open framework structures with desirable features. The presence of functional groups in the organic linkers leads to changes in the Brønsted/Lewis acid- base properties and the solubility of the starting materials [23]. In the present research, the organic linker, 2-aminoterephtalic acid (H_2N-BDC) will be utilized. It is one of the simplest aminodiacids and is well known to form zwitterions depending on the specific pH conditions [23]. Two MOFs were synthesized, NH_2-MIL-101(Fe) and NH_2-MIL-88B(Fe), which are both composed of the same metal node and organic linkers, yet differ in structure. Their photocatalytic activity was further investigated over the degradation of Cr(VI) under visible light irradiation.

Little work has been reported on this specific application of MOFs, especially using iron as a metal node. This research could further crystallize the knowledge of MOFs for photocatalytic degradation of Cr(VI) as well as provide a novel method for industrial application.

1. Methods

1.1 Chemicals

The materials used for the synthesis included 2-Aminoterephthalic acid (H_2N-BDC) (99%), iron (II) chloride ($FeCl_2$) (98%), iron (III) chloride ($FeCl_3$) (97%), *N,N*-Dimethylformamide (DMF) (99.8%), hydrochloric acid (HCl) (37%), acetic acid (CH_3CO_2H) (99.7%), sodium hydroxide (NaOH) (98%), methanol (CH_3OH) (99.9%), ethanol (C_2H_6O) (99.5%), and copper (Cu(VI)) All chemicals and solvents were purchased from Sigma-Aldrich and used without further purification.

1.2 Procedure for Synthesis

Solvothermal synthesis was used to synthesize 13 batches of MOFs. This is the most conventional method for synthesizing MOFs [24]. For the synthesis of Batch 6, for example, equimolar amounts (0.55 mmol) were weighted of the metal precursor $FeCl_3$ (0.08968 g, 0.55 mmol) and the linker H_2N-BDC (0. 0.09875 g, 0.55 mmol). Sonication was used to dissolve the metal precursor and linker in a 15 mL solution composed of DMF. The resulting solution was sealed tightly in a capped vial and heated for 24 hours in an oven at 145°C. The sample was removed after 24 hours and then cooled. Filtration was performed and the residue was collected. After filtration, the residue was washed thoroughly with 15 mL of CH_3OH. The dried powder of the filtrate was then collected. For Batches 2-4, the metal used was $FeCl_2$; however, previous studies have shown photocatalytic activity with the metal precursor $FeCl_3$ and therefore, this precursor was used for the remaining syntheses. The procedure was altered by varying the amount of linker and metal, the solvent, promoter/s, ratio of solvent to promoter and temperature. The synthesis of these hybrid solids is very sensitive to these parameters and leads to a formation of different hybrid phases and alternative structures. One study found that the nature of the reaction medium has the most profound impact on structure formation of MOFs. Additionally, the researchers reported that the concentration of the starting mixture and the temperature are both key parameters for the formation of various hybrid phases [23]. The synthesis parameters of all 14 batches is tabulated in Table 1 in the Supplementary Material.

1.3 Characterization

Powder X-ray diffraction (PXRD) for the samples which produced enough yield (Batches 3, 5, 6, 7, 8, 9, 10, 11, 12, 13, 14) were obtained with a Bruker D2 Phaser X-ray powder diffractometer using CoKα radiation (λ = 1.79Å). Data were obtained at 0.024 increments in the 2θ range of 5-50° at a scan speed of 0.30 s/step. All samples were dried overnight to remove guest solvent molecules within the pores prior to the XRD scan.

Fourier transform infrared spectra (FT-IR) of the crystalline samples (batches 3, 5, 6, 7, 8, 9, 10, 11, 12, 13, 14) were directly recorded on a Bruker Tensor 37 infrared spectrometer. The spectral range measured was set to 4000cm^{-}1-600cm^{-}1. The resolution was set to 2cm^{-}1. The back scan time was set to 32s.

Optical absorption of the different materials was investigated using Ultraviolet-visible (UV-vis) spectroscopy. UV-vis for the DD-717 batches (batches 3, 5, 6, 7, 8, 9, 10, 11, 12, 13, 14) was performed. 5.5 mg of the sample was placed into a flask along with 5.5 mL of water to obtain a 1mg/mL sample. The solution was dissolved through sonication, placed in a cuvette, and then in the UV-vis spectrophotometer. The range of wavelengths was set to 1000nm-300nm with a scan rate of 600 nm/min.

1.4 Photocatalytic Degradation

The photocatalytic activity of the various iron(III) based MOFs was evaluated with the reduction of hexavalent chromium. 4

mg of the photocatalyst were dissolved in a 10 mL aqueous solution through sonication. Previous research has used potassium dichromate ($K_2Cr_2O_7$) as a Cr(VI) compound [7]. Thus, a $K_2Cr_2O_7$ sample was prepared (80 mg L-1). A solution of the dye and photocatalyst was prepared by adding 0.5mL of the dye to 5mL of the photocatalyst. Next, the sample was placed in a cuvette and irradiated with visible monochromatic light. The UV-vis spectrum was then measured over time for a total of 75 minutes, with incremental measurements being taken every 5 minutes. The irradiation portion of the expreiment was done at AM 1.5G (1 sun) and the spectrum was measured at lower light excitation density by using a neutral density filter (20% transmittance). The following batches were measured for their photocatalytic activity: 5,6,7,9,10,11,12. Comparisons between these batches would yield useful knowledge about the synthesis procedures which yield the best photocatalyst. As a control, each batch was exposed to visible light for 20 minutes, without the dye. Additionally, the dye itself, $K_2Cr_2O_7$, was also measured as a control when it was solely exposed to visible light for 20 minutes. The data of these photocatlytic degradation experiments can be found in Figures S.4 and S.5 in the Supplementary Material.

2. Results and Discussion

2.1 Characterization of the MOF photocatalysts

2.1.1 NH_2-MIL-88B(Fe)

PXRD The metal-organic framework NH_2-MIL-88B(Fe) was produced through solvothermal synthesis with the procedure described above. This MOF corresponds to Batches 6 and 8 (see Supplementary Material, Table 1). The crystallographic structure of these 2 products was determined using PXRD. Figure 3 shows the diffractogram for Batches 6 and 8. These diffraction patterns are in good agreement with the previously reported diffraction pattern of NH_2-MIL-88B(Fe)[23]. Additionally, the degree of crystallinity was examined for the MOFs, Batch 6 and Batch 8. Once again, Figure 3 shows that the crystal has 2 distinct peaks with one of particularly high intensity suggesting high crystallinity. The rest of the XRD shows some broader peaks with lower intensity indicating that the material is amorphous. Thus, the structure does not have perfect crystallinity.

FT-IR Next, in order to confirm that Batches 6 and 8 are indeed NH_2-MIL-88B(Fe), FT-IR was performed on both MOFs. From Figure 4, it is clear that these batches have very similar FT-IR spectra. These FT-IR spectra were compared with previously reported FT-IR spectra of NH_2-MIL-88B(Fe)[23, 7, 25] and were found to be almost identical. In fact, the MOF fingerprint region aligns for Batches 6, 8, and NH_2-MIL-88B(Fe). Since every MOF has a distinct fingerprint region, a high similarity between the MOFs synthesized in the present research and NH_2-MIL-88B(Fe) gives further confirmation that Batches 6 and 8 are indeed NH_2-MIL-88B(Fe) Therefore, both PXRD and FT-IR data provide clear evidence that the MOFs synthesized and labeled as Batches 6 and 8 are NH_2-MIL-88B(Fe).

Not only does the FT-IR data provide a confirmation of the characterization of Batches 6 and 8, but it also allows for further structure and functional group determination of this MOF. The FT-IR analysis is illustrated in Figure S.7 in the Supplementary Material. From the FT-IR spectrum, several conclusions can be drawn. The region between 1300 cm^{-1} and 1700cm^{-1} is related to the carboxylate groups of the ligands and thus gives an indication of the coordination of these groups to the metallic sites of the MOF. More precisely, two bands exist at 1585cm^{-1} and 1435cm^{-1} which correspond to the symmetric and asymmetric stretching vibrations of carboxylate groups. These peaks indicate the presence of H_2N-BDC anions in the structure. A band at around 1700 cm^{-1} is characteristic of protonated carboxylic groups, but it was not observed in the FT-IR of Batches 6 and 8 thus indicating the absence of protonated carboxylic groups [26]. This indicates that H_2N-BDC was incorporated into the MOF framework and that there are no free H_2N-BDC molecules within the pores. A medium strength band is found at 1269cm^{-1} which is associated with the C-O stretch of H_2N-BDC. Furthermore, the wide band around 3000 cm^{-1} indicates a carboxylic acid O-H stretch from the H_2N-BDC. Lastly, the doublet around 3400 cm^{-1} corresponds to the asymmetrical and symmetrical stretching of the amine moieties in H_2N-BDC.

2.1.2 NH_2-MIL-101(Fe)

PXRD The Batches 9, 10, 11, and 12 were synthesized through solvothermal synthesis with the parameters described in Table 1 in the Supplementary Material. All of these batches were characterized to be the MOF known as NH_2-MIL-101(Fe). The crystal structure of all four of these batches was gathered and analyzed with PXRD. Figure 5 shows the resulting diffraction patterns for Batches 9, 10, 11, and 12. All four batches have extremely similar diffraction patterns, providing evidence that they all have the same crystal structure. The peaks in the XRD correspond to the previously reported diffraction pattern of NH_2-MIL-101(Fe) [23, 18, 27]. Thus, the PXRD gives the first indication that these batches can be classified as NH_2-MIL-101(Fe). From the PXRD, the level of crystallinity of the MOFs can also be determined. The diffraction pattern for NH_2-MIL-101(Fe) shows more peaks than the one for NH_2-MIL-88B(Fe). The novel peaks in this structure are of medium intensity, indicating the higher crystallinity for NH_2-MIL-101(Fe) in comparison to NH_2-MIL-88B(Fe).

FT-IR The FT-IR spectrum of Batches 9, 10, 11, and 12 are overlaid and shown in Figure 6. First, the fingerprint region corresponds to that of previously reported spectra of NH_2-MIL-101(Fe) thus confirming the characterization made with the PXRD in the previous paragraph [23, 18, 27].

The FT-IR is useful in determining other aspects of the structure of the MOF, including its functional groups. Figure S.6 in the Supplementary Material provides an assignment of the peaks for the batches that were previously clas-

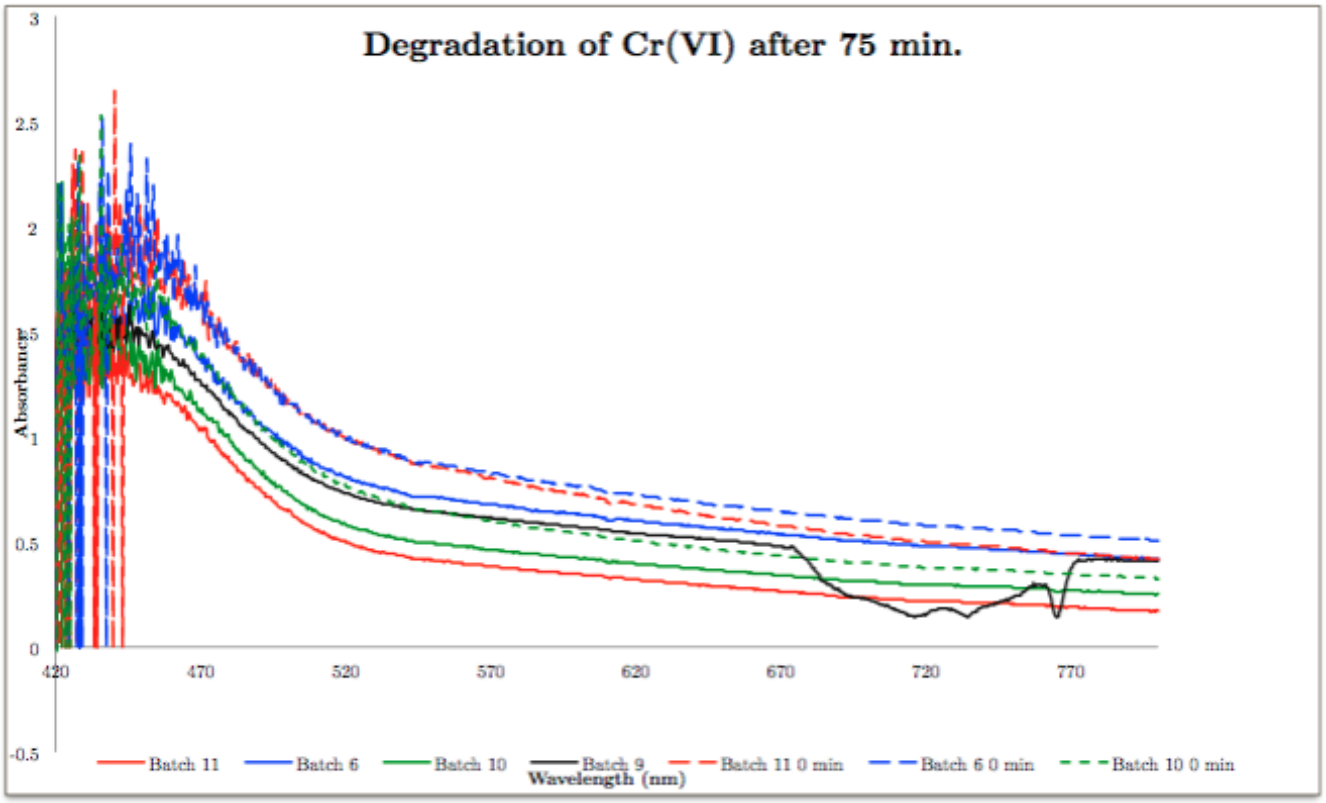

Figure 1. Photocatalytic degradation of hexavalent chromium after 75 minutes of exposure of the photocatalyst and dye to visible light. NH_2-MIL-101(Fe) (Batches 9, 10, 11) shows a better degradation ability than NH_2-MIL-88B(Fe) (Batch 6)

sified as NH_2-MIL-101(Fe). As with NH_2-MIL-88B(Fe), there are once again two bands at 1585cm^{-1} and 1435cm^{-1} in NH_2-MIL-101(Fe). They correspond to the asymmetric and symmetric C-O stretching vibrations of carboxylates and give a clear indication that there are H_2N-BDC anions in the MOF structure. Figure S.8 in the Supplementary Material shows the FT-IR spectra of NH_2-MIL-101(Fe) and NH_2-MIL-88B(Fe) and their main differences. It is important to note that there is a difference in intensity in the bands aforementioned (i.e. 1585cm^{-1} and 1435cm^{-1}); namely, they are both more intense in the NH_2-MIL-101(Fe) spectrum. This change in intensity may be related to a change in the coordination of the carboxylate ligands from the H_2N-BDC in NH_2-MIL-101(Fe). Another difference between NH_2-MIL-101(Fe) and NH_2-MIL-88B(Fe) is the characteristic strong band at 1652cm^{-1} in the spectrum of NH_2-MIL-101(Fe) which has a very low intensity in the NH_2-MIL-88B(Fe) FT-IR spectrum. This band indicates a C=O stretch, thus showing the presence of DMF molecules in this structure. One similarity between the FT-IR spectra of NH_2-MIL-101(Fe) and NH_2-MIL-88B(Fe) is the doublet around 3400cm^{-1} corresponding to the asymmetrical and symmetrical stretching of the amine moieties in H_2N-BDC.These bands indicate the presence of amino groups in the MOF crystal. The wide band around 3000cm^{-1} is present for both NH_2-MIL-101(Fe) and NH_2-MIL-88B(Fe) and corresponds to the O-H stretch

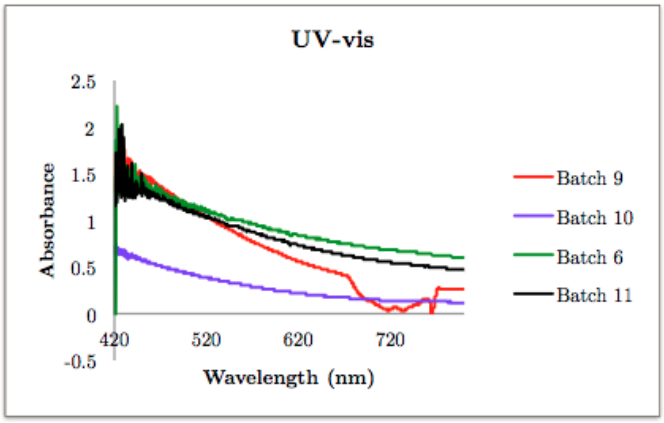

Figure 2. UV-vis of Batch 6 (NH_2-MIL-88B(Fe)) and Batches 9, 10, 11 (NH_2-MIL-88B(Fe))

also from H_2N-BDC. Importantly, the IR spectrum of NH_2-MIL-101(Fe) shows no band at 1700cm^{-1} corresponding to the C=O stretching vibration of hydrogen bonded carboxylic acids. This indicates that H_2N-BDC was incorporated into the MOF framework and there are no free H_2N-BDC molecules within the pores.

2.1.3 UV-vis of NH_2-MIL-101(Fe) and NH_2-MIL-88B(Fe)

The UV-specta of all batches that were tested for their photocatalytic activity in the next section are illustrated in the Sup-

plementary Material Figure S.3. In Figure 2, the UV-vis spectra of NH_2-MIL-88B(Fe) (Batch 6) and NH_2-MIL-88B(Fe) (Batches 9, 10, 11) is overlaid and compared. The spectra show that all 4 of these MOFs have a clear optical response in the visible light region. All of these iron(III) based MOFs have an absorbance peak at approximately 420nm, which is in the visible light region of the spectrum. Thus, they can all be further tested for their photocatalytic capability under visible light irradiation in the following section: "Evaluation of Photocatalytic Activity".

2.1.4 Other characterizations

Batch 7 was different in its synthesis, since its solvent was water instead of DMF. The XRD (Figure S.1 in Supplementary Material) shows broad peaks with very low intensity. Therefore, the structure has very low crystillinity. When comparing the data from the XRD and FT-IR (Figure S.1 and S.2 respectively in Supplementary Material) with previous research, Batch 7 also resembles NH_2-MIL-88B(Fe) just like Batches 6 and 8 [23, 7]. The FT-IR thus has similar characteristics as described previously for NH_2-MIL-88B(Fe). The fingerprint region once again is similar to NH_2-MIL-88B(Fe). In addition, the two bands around 1585cm^{-1} and 1435cm^{-1} exist that are associated with the stretching vibrations of the carboxylate groups. Similarly to the previous FT-IR of NH_2-MIL-88B(Fe), a medium strength band is found at 1269cm^{-1}, which is associated with the C-O stretch of H_2N-BDC. Another similarity is the wide band around 3000 cm^{-1} associated with a carboxylic acid O-H stretch from H2N-BDC. In Batch 7, however, unlike in the previous batches which were also characterized as NH_2-MIL-88B(Fe) (Batches 6 and 8), there is a band at 1700cm^{-1}. This indicates that H_2N-BDC was not fully incorporated into the MOF framework and that there still remain some free H_2N-BDC molecules within the pores of the MOF.

2.2 Evaluation of Photocatalytic Activity

2.2.1 NH_2-MIL-88B(Fe) vs. NH_2-MIL-101(Fe)

The photocatalytic reduction of hexavalent chromium was performed over NH_2-MIL-88B(Fe) and NH_2-MIL-101(Fe) under visible light irradiation as described previously. The photocatalytic reduction was evaluated by monitoring the decolorization of the UV-vis adsorption spectra of a solution of the photocatalyst and the dye, $K_2Cr_2O_7$, over 75 minutes as illustrated in Figure 1. First, the figure illustrates that all of these iron(III) based photocatalysts were successfully able to degrade the chromium dye over time under visible light irradiation. Thus, both NH_2-MIL-88B(Fe) and NH_2-MIL-101(Fe) are efficient photocatalysts for this reduction.

Next, the efficiency of the photocatalyst was quantified and evaluated. In order to quantify the efficiency of the photocatalysts (NH_2-MIL-88B(Fe) and NH_2-MIL-101(Fe), the difference in the adsorption spectra (75 min. - 0 min) of each MOF in solution with dye was calculated. This difference was calculated for the absorbance peak at 470 nm. since this peak is ascribed to the chromium dye, $K_2Cr_2O_7$ (see Supplementary Material, Figure S.4). Figure 1 illustrates the adsorption spectra of Batch 6 (NH_2-MIL-88B(Fe) in solution with the dye at both 0 minutes and 75 minutes. The absorbance at 470 nm. for Batch 6 in solution with the dye at 0 minutes is 1.639, while at 75 minutes the absorbance drops to 1.371. Thus, the difference between the absorbance (75 min - 0 min) at 470nm. is 0.268. The same calculation was performed for NH_2-MIL-101(Fe) or Batches 9, 10, 11. The difference of the absorbance at 75 minutes and 0 minutes at an absorbance peak of 470 nm. for Batch 9 is 0.786, for Batch 10 is 0.274, and for Batch 11 is 0.607. The efficiency of the photocatalysts is thus Batch 9 (NH_2-MIL-101(Fe) > Batch 11 (NH_2-MIL-101(Fe) > Batch 10 (NH_2-MIL-101(Fe) > (Batch 6 (NH_2-MIL-88B(Fe). This illustrates that all of the NH_2-MIL-101 photocatalysts (Batches 9, 10, 11) were more efficient in the degradation of Cr(VI) compared to NH_2-MIL-88B(Fe) (Batch 6). This result leads to several conclusions. First, the synthesis was a deciding factor which influenced which MOF was formed. If the molar ratio of the ligand and metal were the same, then NH_2-MIL-88B(Fe) was formed. However, if the molar ratio of the ligand and metal were different (2:1 or 1:2), then NH_2-MIL-101(Fe) was formed. This molar ratio may be the main contributing factor to the structural differences between the two photocatalysts and in turn, NH_2-MIL-101(Fe)'s enhanced photocatalytic activity. Secondly, the photocatalytic activity may be enhanced for NH_2-MIL-101(Fe) because of its crystallinity. In fact, it was previously concluded that NH_2-MIL-101(Fe) has a higher crystallinity than NH_2-MIL-88B(Fe) (see Figures 5 and 3). Third, the photocatalytic activity may be enhanced for NH_2-MIL-101(Fe) because of its structure as found in the FT-IR study previously. One main differences were highlighted in the FT-IR spectra for NH_2-MIL-101(Fe) and NH_2-MIL-88B(Fe); namely, the intensity of the bands corresponding to the symmetric and asymmetric stretching vibrations of the carboxylate groups is higher for NH_2-MIL-101(Fe) as compared to NH_2-MIL-88B(Fe) (Supplementary Material, Figure S.8). This change in intensity may be related to a change in the coordination of the carboxylate ligands from the H_2N-BDC in NH_2-MIL-101(Fe) which may in turn change the structure of the MOF enhancing its photocatalytic activity. Thus, the synthesis, crystallinity, and structure of NH_2-MIL-101(Fe) may all be involved in its enhanced photocatalytic activity as compared to NH_2-MIL-88B(Fe).

Thus far, only the photocatalytic activity of NH_2-MIL-101(Fe) and NH_2-MIL-88B(Fe) were compared and NH_2-MIL-101(Fe) was found to have superior activity. Next, all of the NH_2-MIL-101(Fe) MOFs (Batches 9, 10, and 11) can be compared to find which Batch has the most efficient photocatalytic activity and relate it to its synthesis. The differences in the synthesis of these MOFs can be seen in Table 1 in the Supplementary Material. First of all, they all have non-equimolar ratios of ligand and metal, which as mentioned previously, makes them NH_2-MIL-101(Fe) rather than NH_2-MIL-88B(Fe). Batch 9 had the highest efficiency (0.786) and

it was synthesized with DMF and acetic acid in a 2:1 metal to ligand ratio. Batch 11 had the second highest efficiency (0.607) and it was solely synthesized with DMF in a 2:1 metal to ligand ratio. Batch 10 had the lowest efficiency (0.274) and it was synthesized with DMF and acetic acid in a 2:1 ligand to metal ratio. Thus, if 9 and 10 are compared, it can be concluded that the molar ratio of ligand to metal has the highest significance in determining the photocatalytic efficiency. In fact, a higher ratio of metal to ligand corresponds to a higher photocatalytic efficiency, whereas a higher ratio of ligand to metal corresponds to a lower photocatalytic efficiency. From these results, acetic acid does not have an effect on the efficiency of the photocatalysts. The molar ratio is the determining factor. The enhanced photocatalytic activity may also be explained by the level of crystallinity of the Batches 9, 10, 11 (see Figure 5). The photocatalyst with the highest activity (Batch 9) is indeed the most crystalline since it has the sharpest and highest peaks, whereas the photocatalyst with the lowest activity (Batch 10) has lower crystallinity as defined by lower intensity peaks. When comparing the FT-IR spectra of Batches 9, 10, 11 (Figure 6), there are no major differences. Thus, the photocatalytic activity of Batch 9 is superior to the rest of the NH_2-MIL-101(Fe) because of its synthesis (higher metal to ligand ratio) and higher crystallinity.

2.2.2 Other Batches

The photocatalytic activity of Batch 5, 7, and 12 was also investigated. The results of these experiments are illustrated in Figure S.4 in the Supplementary Material. The results for Batches 5 and 12 were not analyzed due to the fact that these photocatalysts were unable to fully dissolve in the water solution. In turn, they precipitated as they were irradiated by light on their own. Thus, the results may show degradation, even if there is not any. This limitation could have been avoided if the samples of the dye and photocatalyst as well as the samples of the photocatalyst in aqueous solution were constantly stirred as they were irradiated by light. This would ensure that there would be no precipitate formed. Thus, these Batches were excluded from further analysis.

Batch 7 was also investigated for its photocatalytic activity. The results of these experiments can be found in Figure S.4 in the Supplementary Material. Fortunately, the photocatalyst on its own did not precipitate when it was irradiated with light, thus it could be analyzed. However, this Batch showed no photocatalytic degradation of the Cr(VI) dye after 75 minutes. It was previously characterized as NH_2-MIL-88B(Fe), but when the XRD was analyzed it was found to be amorphous. Thus, perhaps due to the low crystallinity of this MOF, it was unable to be an efficient photocatalyst. Additionally, Batch 7 was the only one that was synthesized with water as the solvent, whereas the other NH_2-MIL-88B(Fe) photocatalysts (Batch 6 and 8) were synthesized with DMF. From these results, it is clear that water is a poor solvent. It does form crystals with the NH_2-MIL-88B(Fe) structure, but they are amorphous and thus inefficient for photocatalysis.

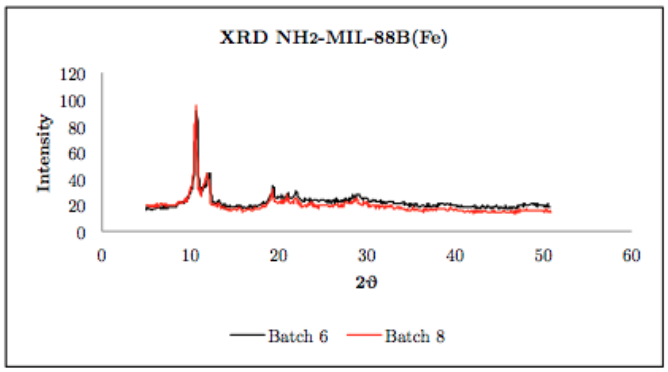

Figure 3. XRD of Batches 6 and 8, characterizing them as NH_2-MIL-88B(Fe)

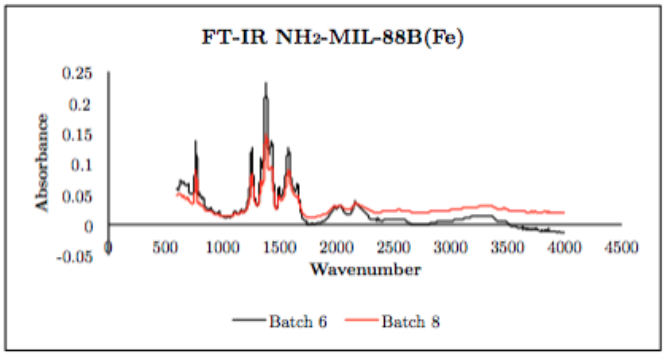

Figure 4. FT-IR of Batches 6 and 8 further confirming their structure to be NH_2-MIL-88B(Fe).

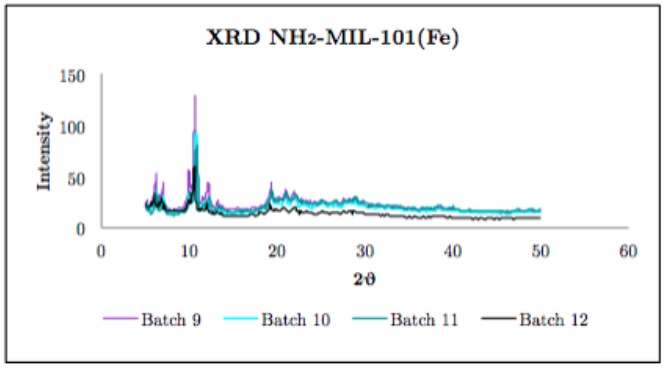

Figure 5. XRD of Batches 9, 10, 11, 12 characterizing them as NH_2-MIL-101(Fe)

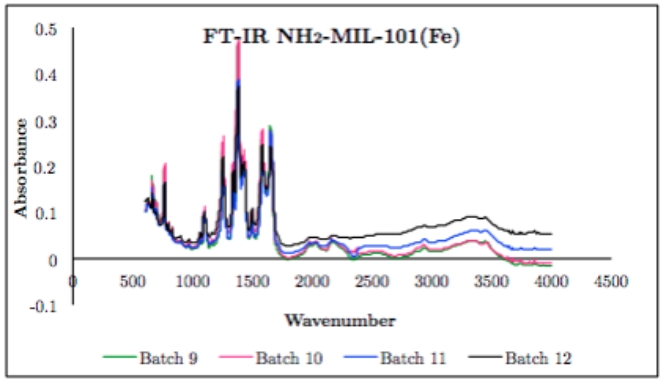

Figure 6. FT-IR of Batches 9, 10, 11, and 12 further supporting that they are NH_2-MIL-101(Fe)

3. Conclusion

To conclude, the present research aimed at investigating the photocatalytic activity of iron(III) based MOFs under visible light irradiation by testing their ability to degrade hexavalent chromium. Although all MOFs were synthesized with an iron node and a 2-aminoterephtalic acid linker, there were different structures formed; namely, NH_2-MIL-101(Fe) and NH_2-MIL-88B(Fe). The only difference in the synthesis which led to a formation of a different structure was the molar ratio of the metal and linker. If the molar ratio was the same, then NH_2-MIL-88B(Fe) was formed. However, if the molar ratio between the metal and linker was either 2:1 or 1:2, NH_2-MIL-101(Fe) was formed. This finding can be supported by previous research that has found that increasing the iron(III) concentration favored the production of MIL-101 crystals rather than MIL-88B crystals [28]. Thus, the first finding of the present study is that the molar ratio between metal and ligand is a deciding factor in the formation of different MOF structures.

The second finding of the present research is that water was not a good choice for a solvent. Although a MOF which was characterized as NH_2-MIL-88B(Fe) was synthesized (Batch 7), it was unable to degrade hexavalent chromium due to its amorphous nature. Thus, using DMF as a solvent for the synthesis of NH_2-MIL-88B(Fe) and NH_2-MIL-101(Fe) is ideal, since it leads to a crystalline structure, which in turn allows for photocatalysis.

The most important finding of this research is that amino-substituted MIL-101 is a much more efficient photocatalyst for the reduction of Cr(VI) compared to amino-substituted MIL-88B. This is likely to be due to differences in crystallinity of the two structures or differences in the structures themselves. NH_2-MIL-101(Fe) was found to be much more crystalline and it had a change in the coordination of the carboxylate ligands from the H_2N-BDC. Thus, both the structure and crystallinity of this MOF could be the potential factors that led to an increased efficiency in comparison to NH_2-MIL-88B(Fe). However, the present research does not provide enough information for the deduction of the precise mechanism of degradation of Cr(VI) by the two MOFs. Further research needs to be conducted in order to understand precisely why the structure of NH_2-MIL-101(Fe) is better able to perform photocatalytic degradation of hexavalent chromium under visibile light irradiation. Lastly, the efficiency of the three NH_2-MIL-101(Fe) photocatalysts was evaluated. The results indicate that a higher metal to ligand ratio of NH_2-MIL-101(Fe) consequently led to higher photocatalytic efficiency, whereas a higher ligand to metal ratio had the opposite effect. Acetic acid was found to have no effect on the photocatalytic efficiency.

To conclude, the photocatalyst NH_2-MIL-101(Fe) has high potential for cleaning textile wastewater of the toxic heavy metal, Cr(VI). However, further research should be conducted to find ways of enhancing its photocatalytic efficiency even more by modifying more aspects of the synthesis. The present research gives a good starting point for the synthesis of this MOF which makes it an efficient visible-light photocatalyst.

Acknowledgments

A special thank you to my supervisor, Monica Barroso, for helping extensively with this research project. Additionally, a special thank you to Jochem Wijten and Zafer Ozturk for helping with the practical lab work.

References

[1] FN Acar and E Malkoc. The removal of chromium (vi) from aqueous solutions by fagus orientalis l. *Bioresource technology*, 94(1):13–15, 2004.

[2] Juan J Testa, María A Grela, and Marta I Litter. Heterogeneous photocatalytic reduction of chromium (vi) over tio2 particles in the presence of oxalate: involvement of cr (v) species. *Environmental science & technology*, 38(5):1589–1594, 2004.

[3] Jerome O Nriagu and Evert Nieboer. *Chromium in the natural and human environments*, volume 20. John Wiley & Sons, 1988.

[4] Arun K Shanker, Carlos Cervantes, Herminia Loza-Tavera, and S Avudainayagam. Chromium toxicity in plants. *Environment international*, 31(5):739–753, 2005.

[5] Venkatramreddy Velma, SS Vutukuru, and Paul B Tchounwou. Ecotoxicology of hexavalent chromium in freshwater fish: a critical review. *Reviews on environmental health*, 24(2):129–146, 2009.

[6] Robert J Kieber, Joan D Willey, and Suzanne D Zvalaren. Chromium speciation in rainwater: temporal variability and atmospheric deposition. *Environmental science & technology*, 36(24):5321–5327, 2002.

[7] Li Shi, Tao Wang, Huabin Zhang, Kun Chang, Xianguang Meng, Huimin Liu, and Jinhua Ye. An amine-functionalized iron (iii) metal–organic framework as ef-

ficient visible-light photocatalyst for cr (vi) reduction. *Advanced Science*, 2(3), 2015.

[8] Anna L Rowbotham, Leonard S Levy, and Linda K Shuker. Chromium in the environment: an evaluation of exposure of the uk general population and possible adverse health effects. *Journal of Toxicology and Environmental Health Part B: Critical Reviews*, 3(3):145–178, 2000.

[9] S Rengaraj, S Venkataraj, Jei-Won Yeon, Younghun Kim, XZ Li, and GKH Pang. Preparation, characterization and application of nd–tio 2 photocatalyst for the reduction of cr (vi) under uv light illumination. *Applied Catalysis B: Environmental*, 77(1):157–165, 2007.

[10] James A Jacobs and Stephen M Testa. Overview of chromium (vi) in the environment: background and history. *Chromium (VI) handbook*, pages 1–21, 2005.

[11] Françoise C Richard and Alain CM Bourg. Aqueous geochemistry of chromium: a review. *Water Research*, 25(7):807–816, 1991.

[12] LB Khalil, WE Mourad, and MW Rophael. Photocatalytic reduction of environmental pollutant cr (vi) over some semiconductors under uv/visible light illumination. *Applied Catalysis B: Environmental*, 17(3):267–273, 1998.

[13] SG Schrank, HJ José, and RFPM Moreira. Simultaneous photocatalytic cr (vi) reduction and dye oxidation in a tio 2 slurry reactor. *Journal of photochemistry and photobiology A: Chemistry*, 147(1):71–76, 2002.

[14] G Colon, MC Hidalgo, and JA Navio. Influence of carboxylic acid on the photocatalytic reduction of cr (vi) using commercial tio2. *Langmuir*, 17(22):7174–7177, 2001.

[15] Hyunsook Kyung, Jaesang Lee, and Wonyong Choi. Simultaneous and synergistic conversion of dyes and heavy metal ions in aqueous tio2 suspensions under visible-light illumination. *Environmental science & technology*, 39(7):2376–2382, 2005.

[16] Hua Tong, Shuxin Ouyang, Yingpu Bi, Naoto Umezawa, Mitsutake Oshikiri, and Jinhua Ye. Nano-photocatalytic materials: possibilities and challenges. *Advanced Materials*, 24(2):229–251, 2012.

[17] A Corma, H Garcia, and FX Llabrés i Xamena. Engineering metal organic frameworks for heterogeneous catalysis. *Chemical Reviews*, 110(8):4606–4655, 2010.

[18] Katrien GM Laurier, Frederik Vermoortele, Rob Ameloot, Dirk E De Vos, Johan Hofkens, and Maarten BJ Roeffaers. Iron (iii)-based metal–organic frameworks as visible light photocatalysts. *Journal of the American Chemical Society*, 135(39):14488–14491, 2013.

[19] Chong-Chen Wang, Jian-Rong Li, Xiu-Liang Lv, Yan-Qiu Zhang, and Guangsheng Guo. Photocatalytic organic pollutants degradation in metal–organic frameworks. *Energy & Environmental Science*, 7(9):2831–2867, 2014.

[20] Christoph Janiak and Jana K Vieth. Mofs, mils and more: concepts, properties and applications for porous coordination networks (pcns). *New Journal of Chemistry*, 34(11):2366–2388, 2010.

[21] MA Nasalevich, M Van der Veen, Freek Kapteijn, and Jorge Gascon. Metal–organic frameworks as heterogeneous photocatalysts: advantages and challenges. *CrystEngComm*, 16(23):4919–4926, 2014.

[22] Patricia Horcajada, Suzy Surblé, Christian Serre, Do-Young Hong, You-Kyong Seo, Jong-San Chang, Jean-Marc Greneche, Irene Margiolaki, and Gérard Férey. Synthesis and catalytic properties of mil-100 (fe), an iron (iii) carboxylate with large pores. *Chemical Communications*, (27):2820–2822, 2007.

[23] Sebastian Bauer, Christian Serre, Thomas Devic, Patricia Horcajada, Jerome Marrot, Gérard Férey, and Norbert Stock. High-throughput assisted rationalization of the formation of metal organic frameworks in the iron (iii) aminoterephthalate solvothermal system. *Inorganic chemistry*, 47(17):7568–7576, 2008.

[24] David J Tranchemontagne, Joseph R Hunt, and Omar M Yaghi. Room temperature synthesis of metal-organic frameworks: Mof-5, mof-74, mof-177, mof-199, and irmof-0. *Tetrahedron*, 64(36):8553–8557, 2008.

[25] Ya Li Liu, Xi Juan Zhao, Xiao Xi Yang, and Yuan Fang Li. A nanosized metal–organic framework of fe-mil-88nh 2 as a novel peroxidase mimic used for colorimetric detection of glucose. *Analyst*, 138(16):4526–4531, 2013.

[26] Camille Petit. *Factors Affecting the Removal of Ammonia from Air on Carbonaceous Materials: Investigation of Reactive Adsorption Mechanism*. Springer Science & Business Media, 2012.

[27] Bin Wu, Xiaocheng Lin, Liang Ge, Liang Wu, and Tongwen Xu. A novel route for preparing highly proton conductive membrane materials with metal-organic frameworks. *Chemical Communications*, 49(2):143–145, 2013.

[28] Mingyan Ma, Angelique Betard, Irene Weber, Noura Saad Al-Hokbany, Roland A Fischer, and Nils Metzler-Nolte. Iron-based metal–organic frameworks mil-88b and nh2-mil-88b: High quality microwave synthesis and solvent-induced lattice "breathing". *Crystal Growth & Design*, 13(6):2286–2291, 2013.

Iron Based Metal Organic Frameworks as Photocatalysts for Chromium (VI) Degradation

Supplementary Material

Table 1: Parameters for the various syntheses of the Batches.

Batch DD-717	Linker (mmol.) (g.)	Metal (mmol.) (g.)	Solvent: Promoter/s Ratio (mL)	Temperature (°C) Time (hrs.)
2	H2N-BDC 0.55mmol. 0.09629 g,	FeCl2 0.55mmol.0.07232 g.	DMF:HCL 14:1	145 °C 24 hrs.
3	H2N-BDC 0.55mmol. 0.0971 g.	FeCl2 0.55mmol. 0.06806 g.	DMF 15	145 °C 24 hrs.
4	H2N-BDC 0.55mmol. 0.0978 g	FeCl2 0.55mmol. 0.07093 g.	H2O:HCl: C2H6O 7.5:7.5:1	60 °C (oil bath) 24 hrs.
5	H2N-BDC 0.55mmol. 0.09665g	FeCl3 0.55mmol. 0.085 g.	DMF:C2H4O2 14:1	145 °C 24 hrs.
6	H2N-BDC 0.55mmol. 0.09875 g.	FeCl3 0.55mmol.0.08968 g.	DMF 15	145 °C 24 hrs.
7	H2N-BDC 0.55mmol. 0.10245 g.	FeCl3 0.55mmol. 0.08887 g.	H2O:CH6O:C2H4O2 7:7:1	65 °C 24 hrs.
8	H2N-BDC 0.55mmol. 0.09636 g.	FeCl3 0.55mmol. 0.0879 g.	DMF:C2H4O2 14:1	145 °C 24 hrs.
9	H2N-BDC 0.55mmol. 0.09889 g.	FeCl3 1mmol.0.16661 g.	DMF:C2H4O2 14:1	145 °C 24 hrs.
10	H2N-BDC 1mmol. 0.18231 g.	FeCl3 0.55mmol.0.09063 g.	DMF:C2H4O2 14:0.5	145 °C 24 hrs.
11	H2N-BDC 0.55mmol. 0.09798 g.	FeCl3 1mmol. 0.16260 g.	DMF 15	145 °C 24 hrs.
12	H2N-BDC 1mmol. 0.18293 g.	FeCl3 0.55mmol. 0.08901 g.	DMF 15	145 °C 24 hrs.
13	H2N-BDC 1mmol. 0.18259 g.	Iron (III) Chloride 1 mmol. 0.16517 g.	DMF:NaOH 14.5:0.5	140 °C 24 hrs.

Batch DD-717	Linker (mmol.) (g.)	Metal (mmol.) (g.)	Solvent: Promoter/s Ratio (mL)	Temperature (°C) Time (hrs.)
14	H2N-BDC 1 mmol. 0.17976 g.	Iron (III) Chloride 1mmol. 0.16286 g.	DMF:C2H4O2 14:1	140 °C 24 hrs.

XRD Data for all Batches

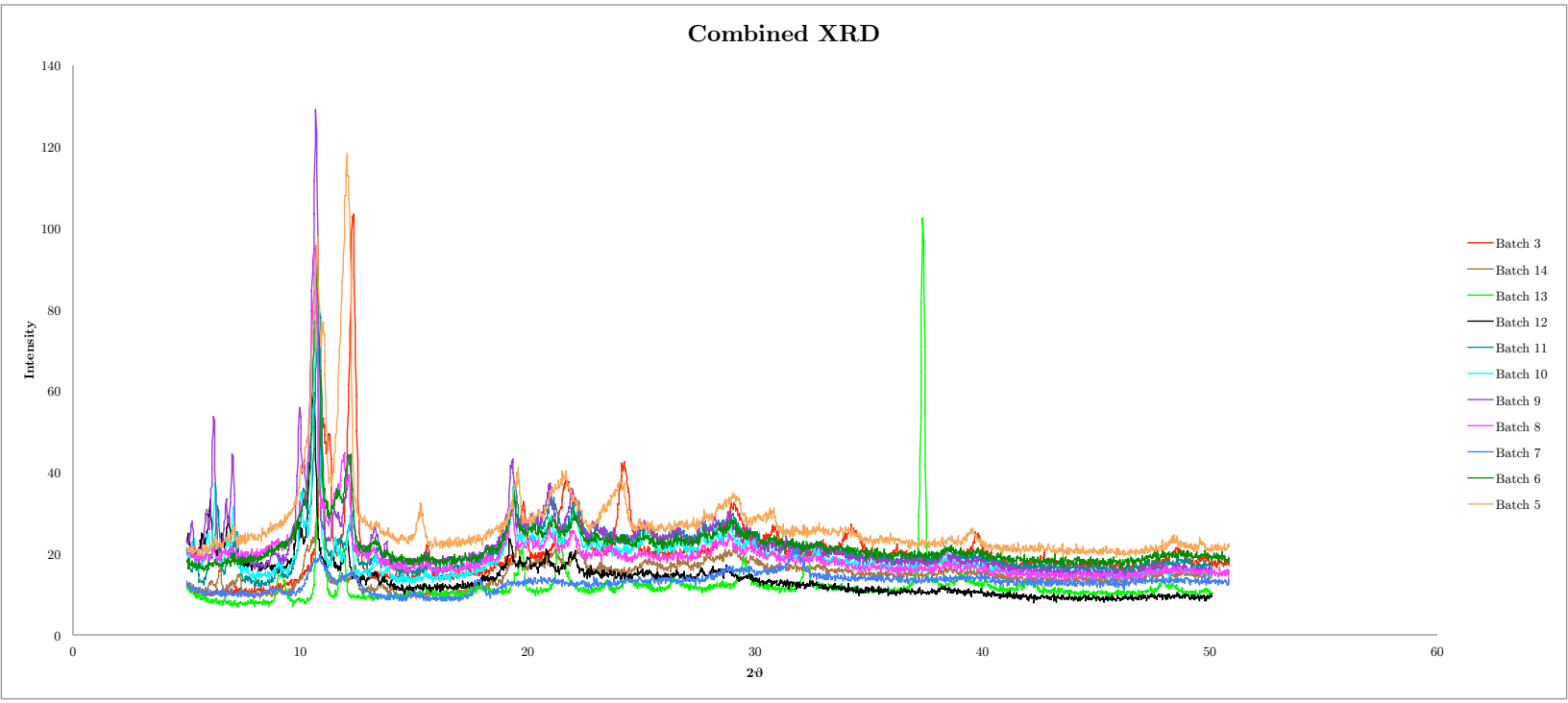

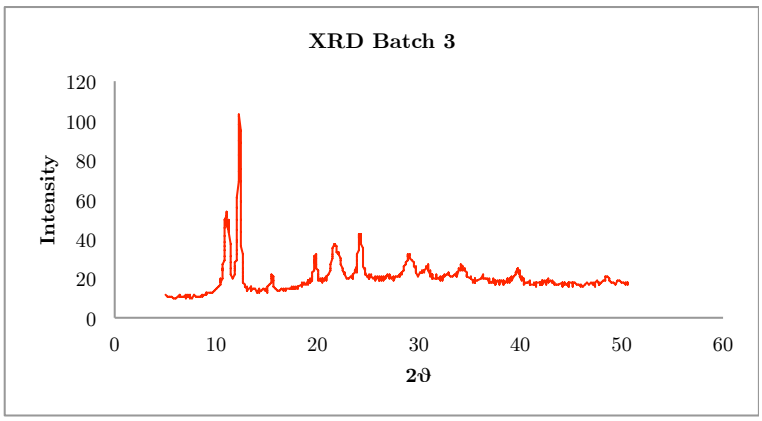

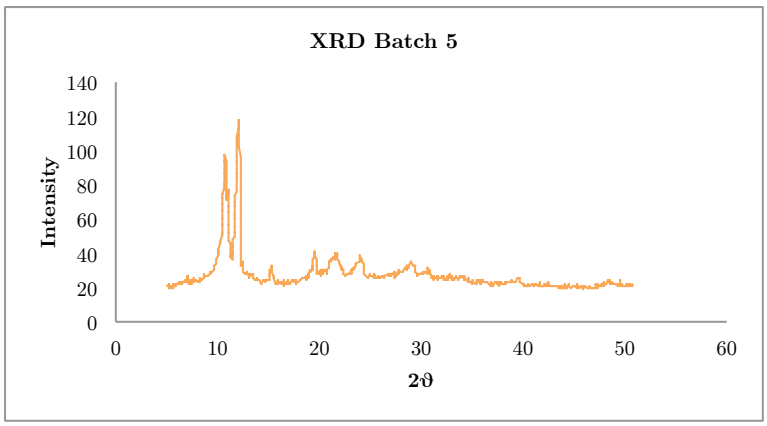

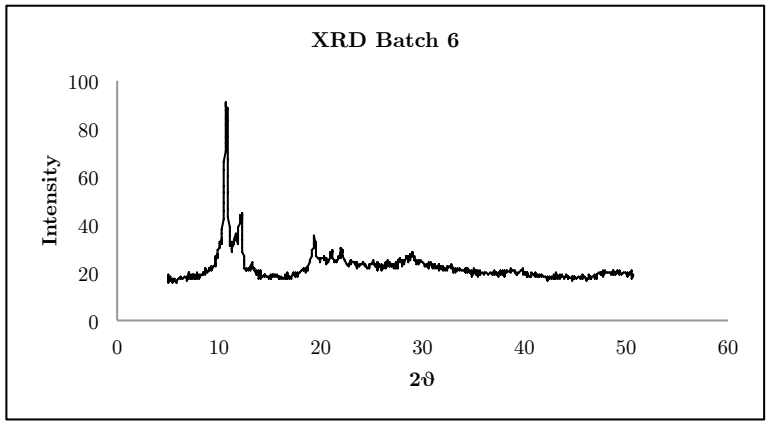

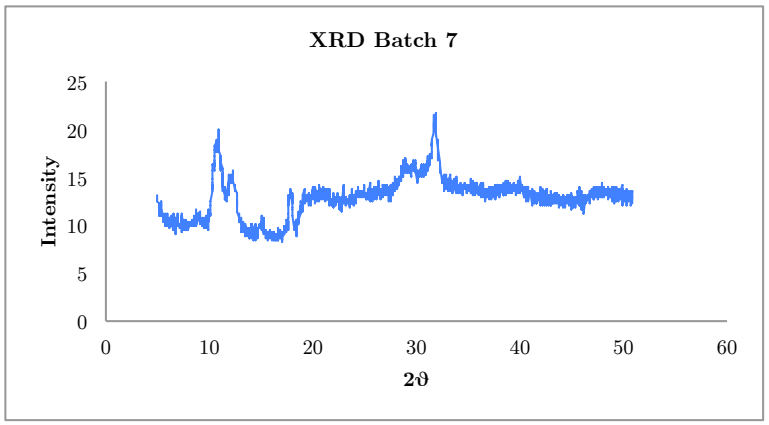

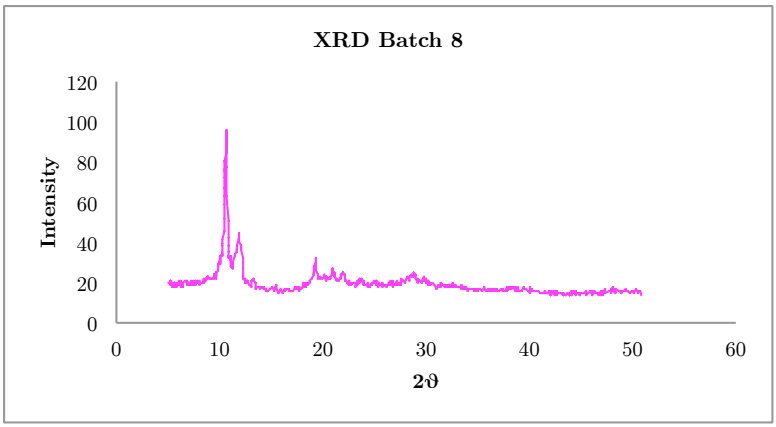

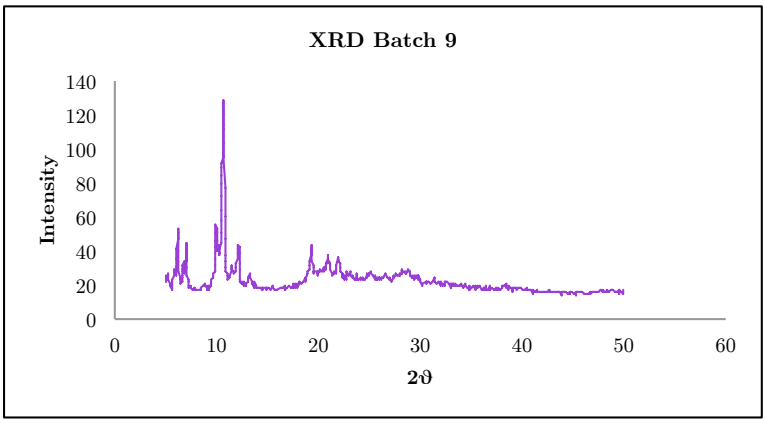

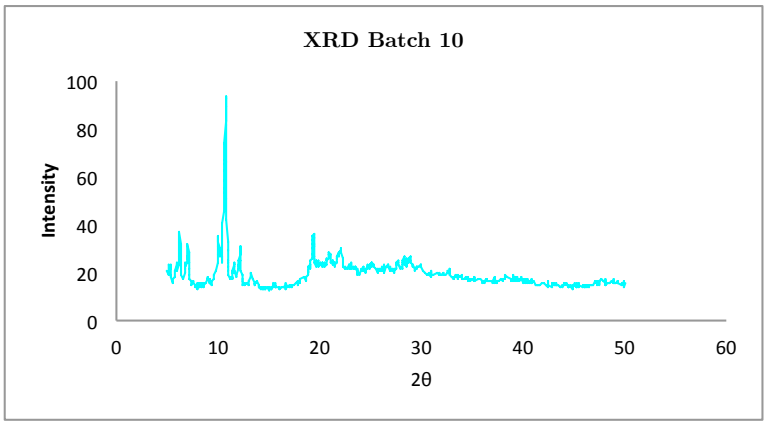

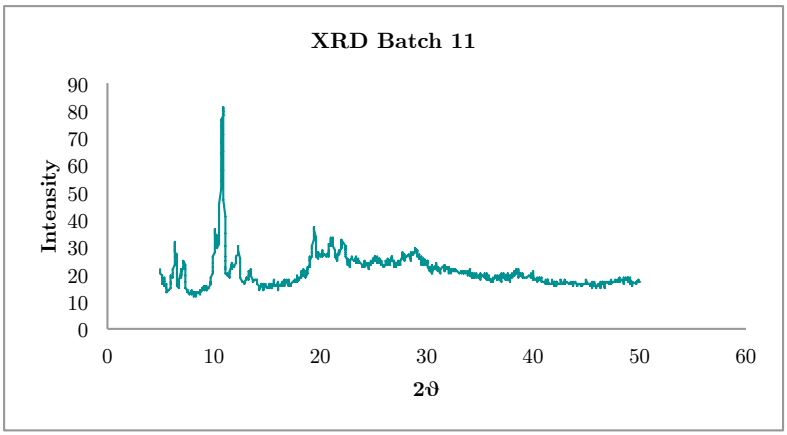

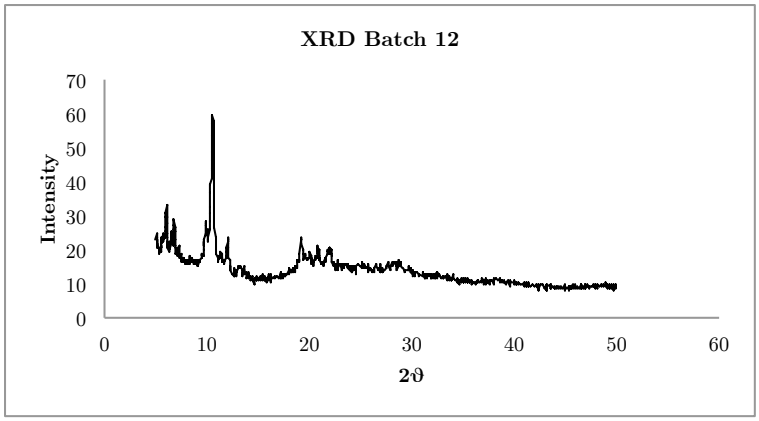

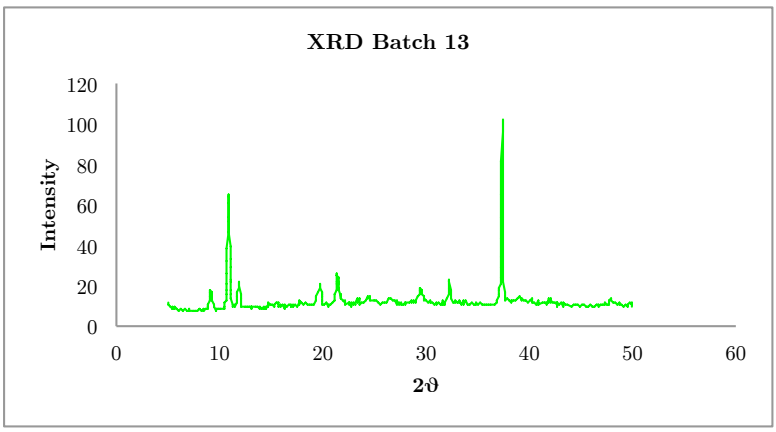

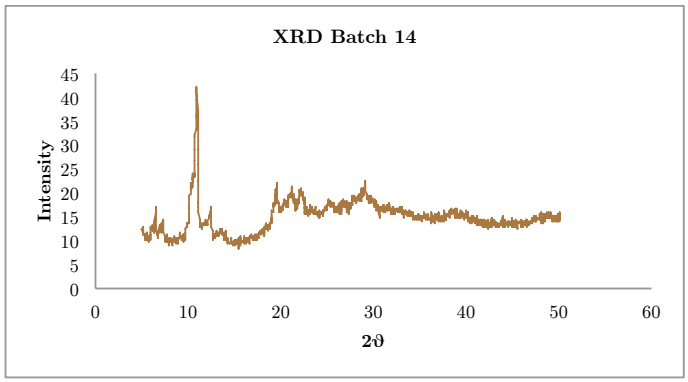

Figure S.1: XRD data for all batches. Batch 6 and 8 have been characterized as NH2-MIL-88B(Fe) and Batches 9, 10, 11, 12 have been characterized as NH2-MIL-101B(Fe).

FT-IR Data for all batches:

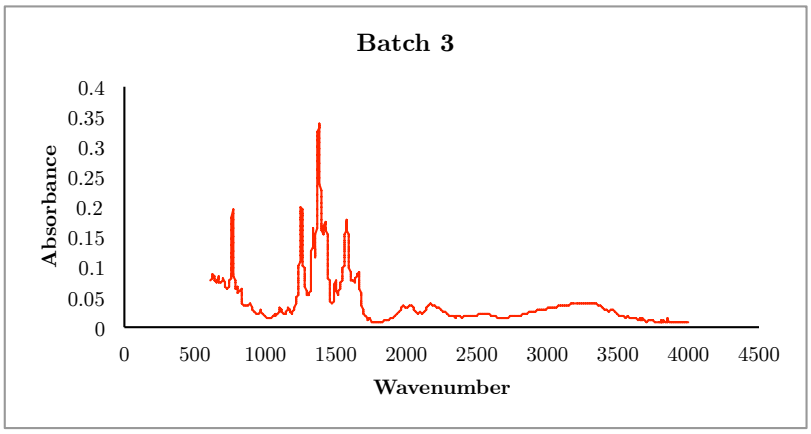

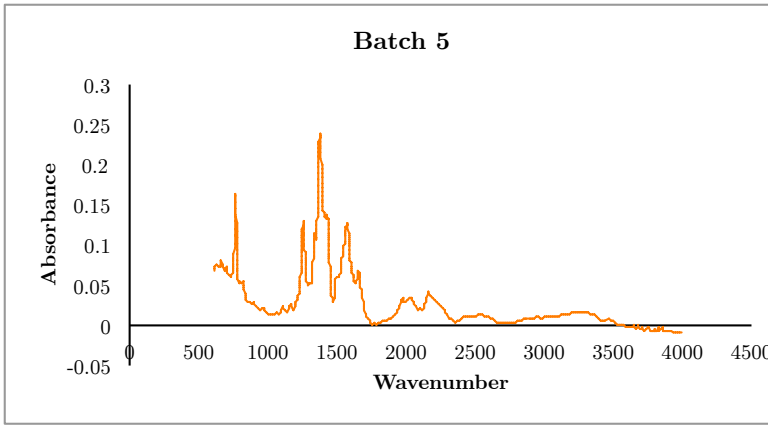

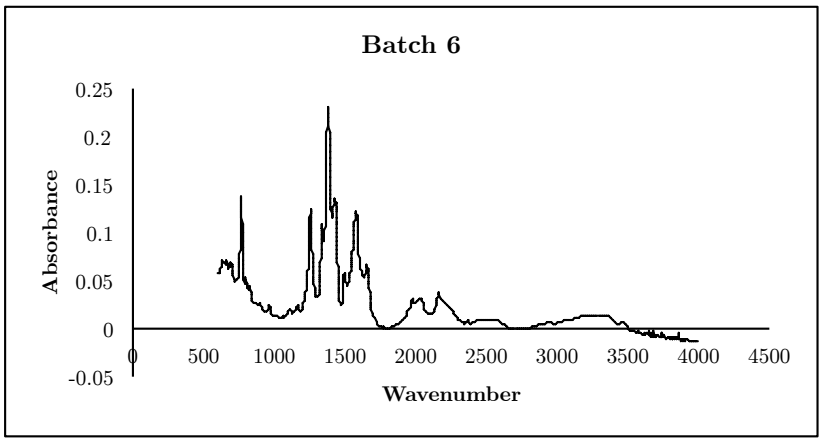

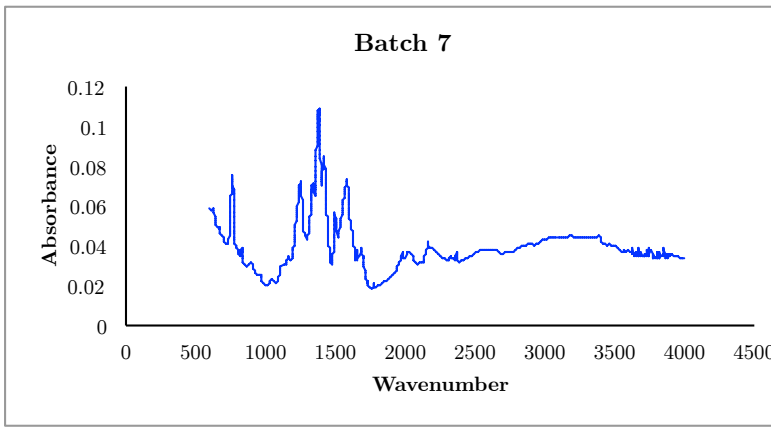

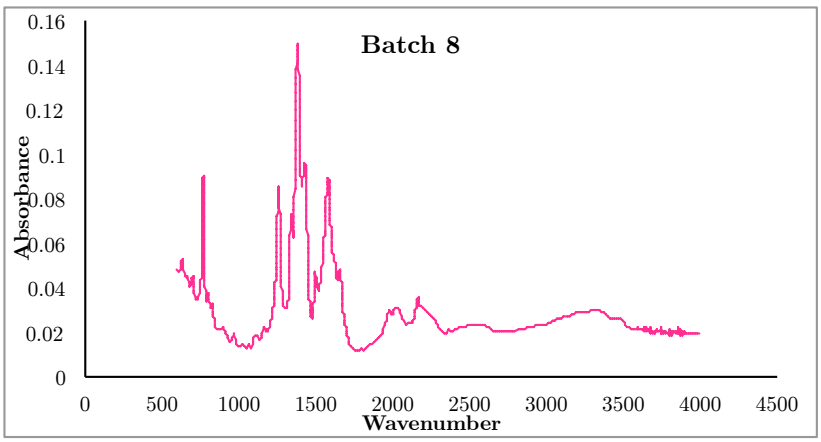

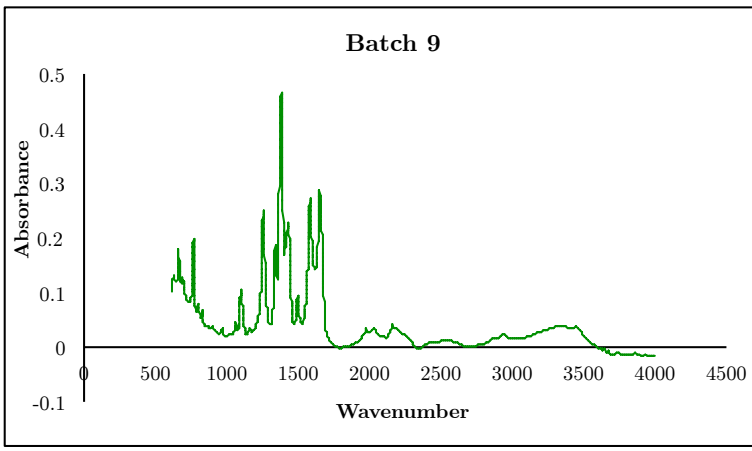

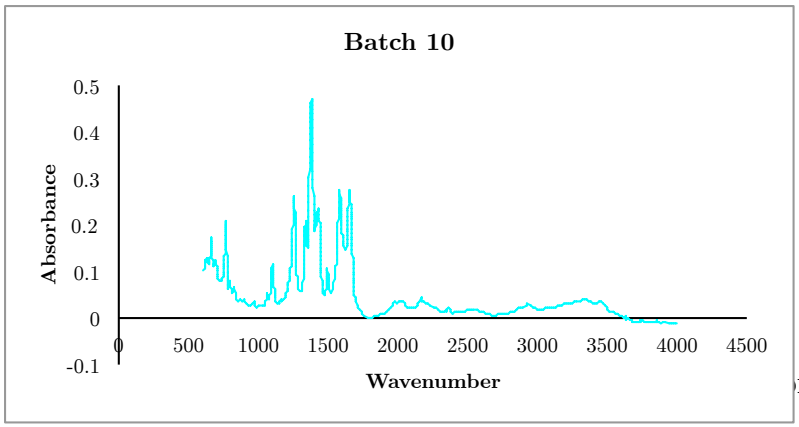

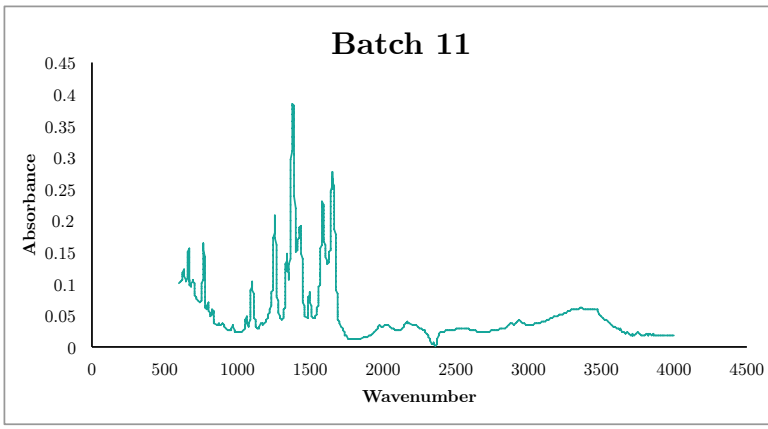

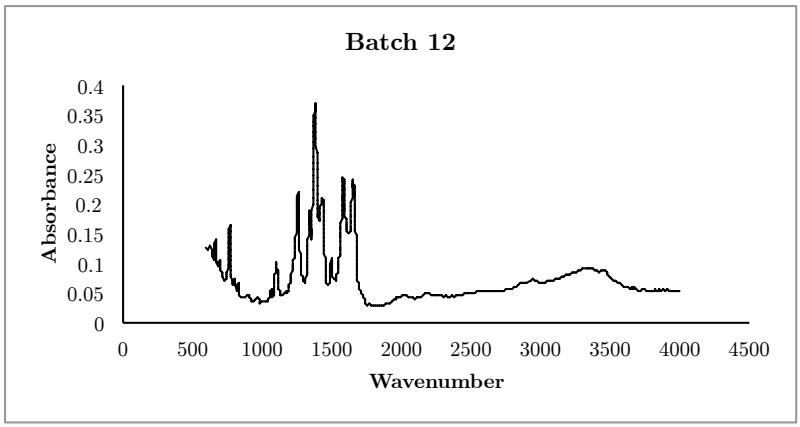

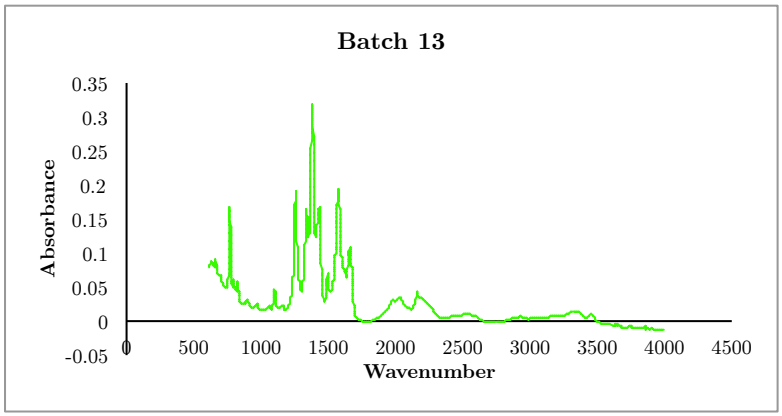

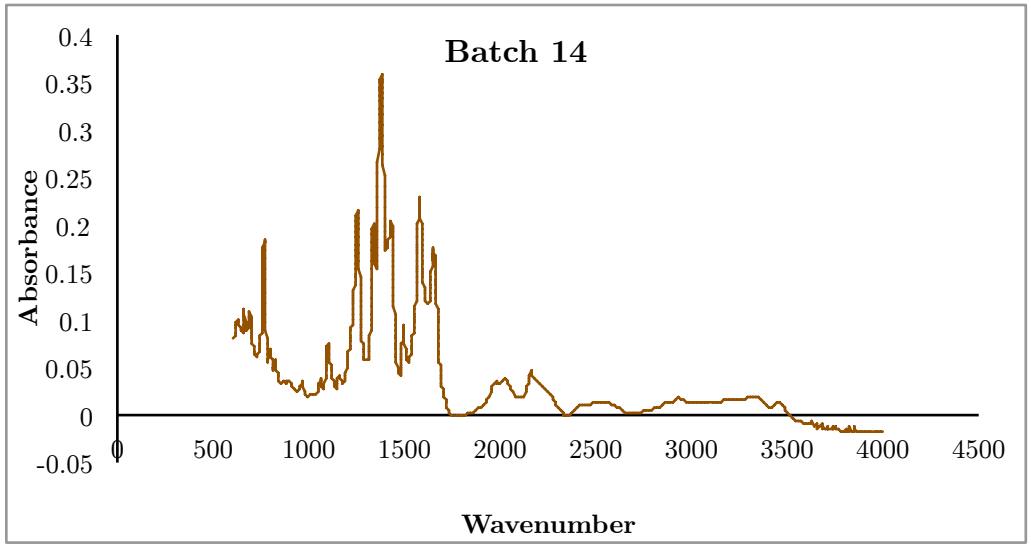

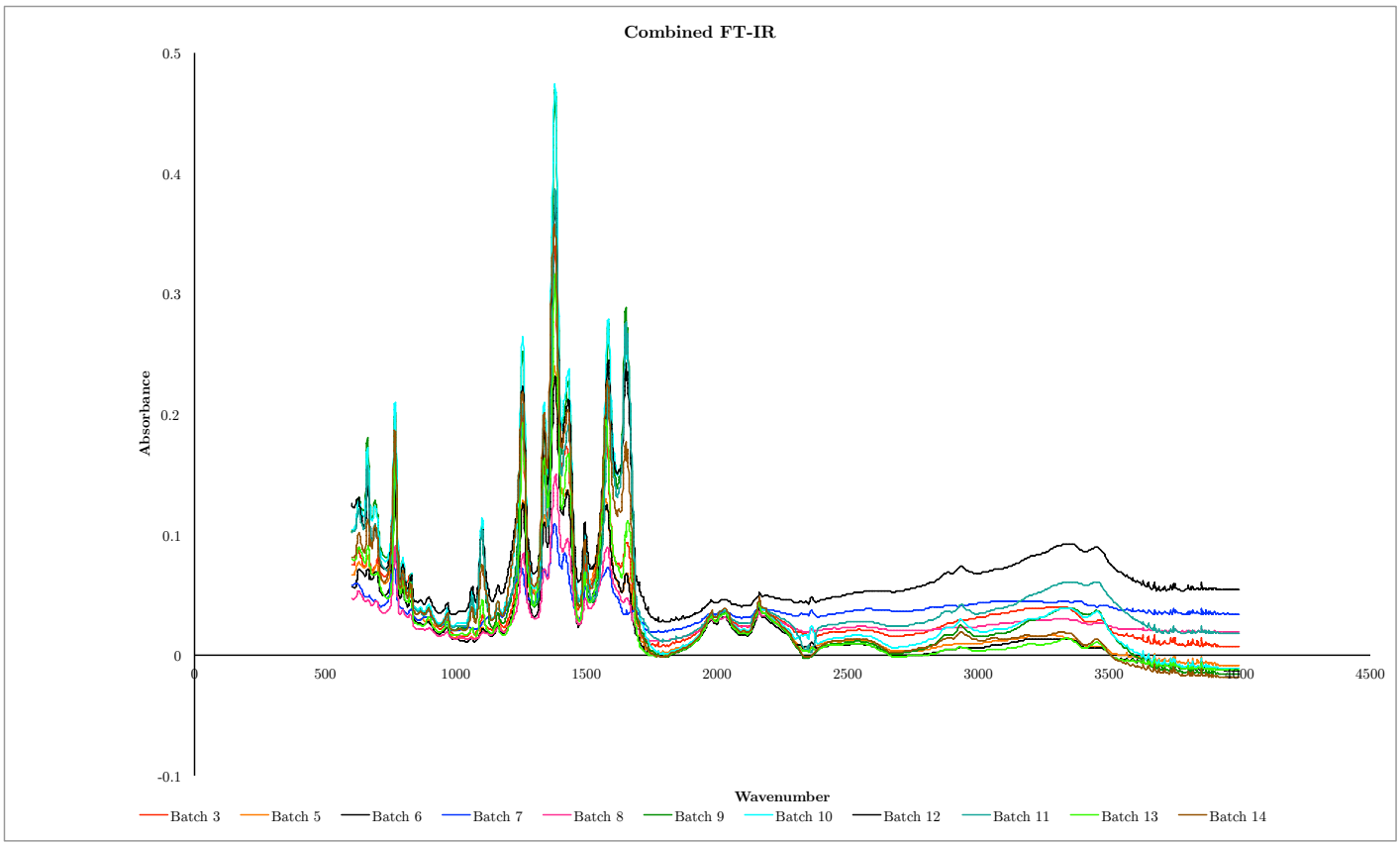

Figure S.2: FT-IR for all batches. Batches 6 and 8 have been characterized as NH2-MIL-88B(Fe). Batches 9, 10, 11, 12 have been characterized as NH2-MIL-101(Fe).

UV-vis Data

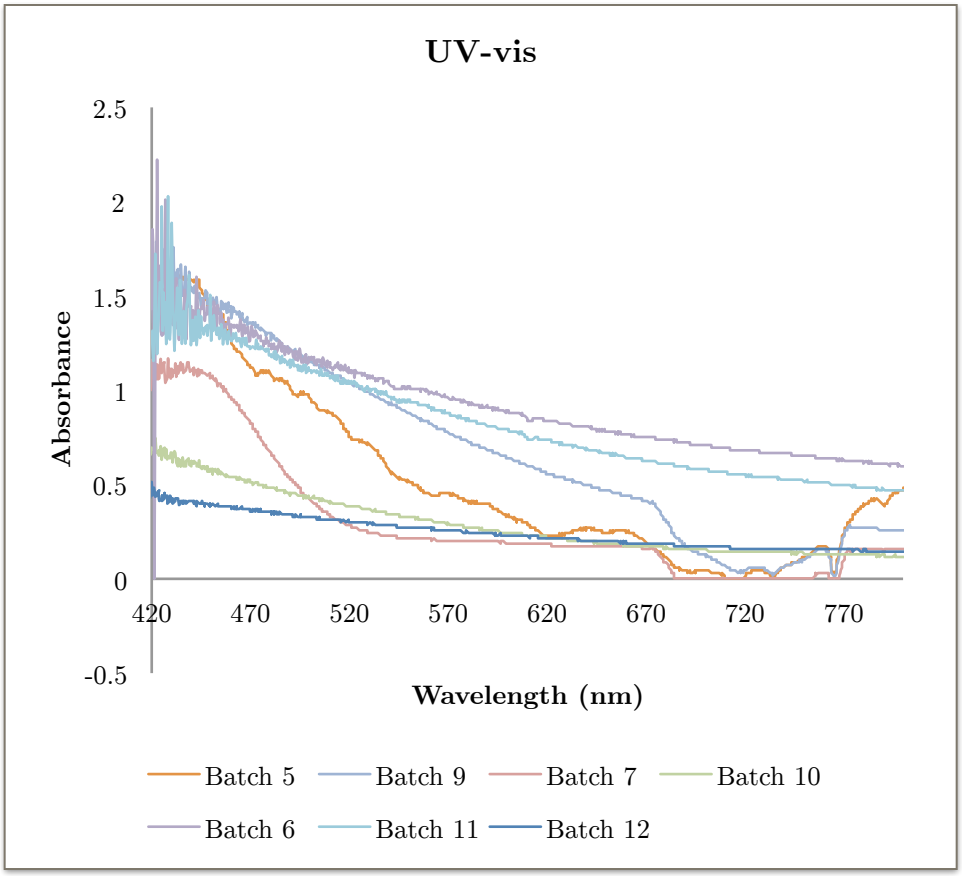

Figure S.3: UV-vis data for batches 5, 6, 9, 10, 11, and 12.

Photocatalytic Degradation

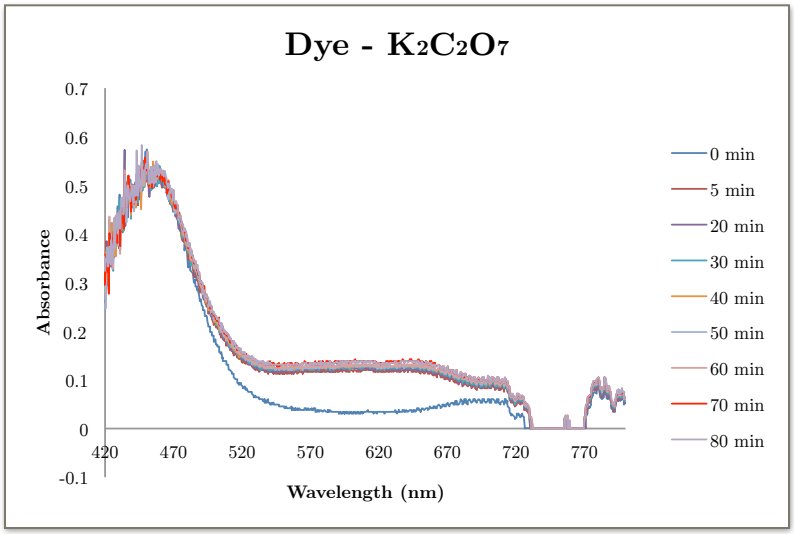

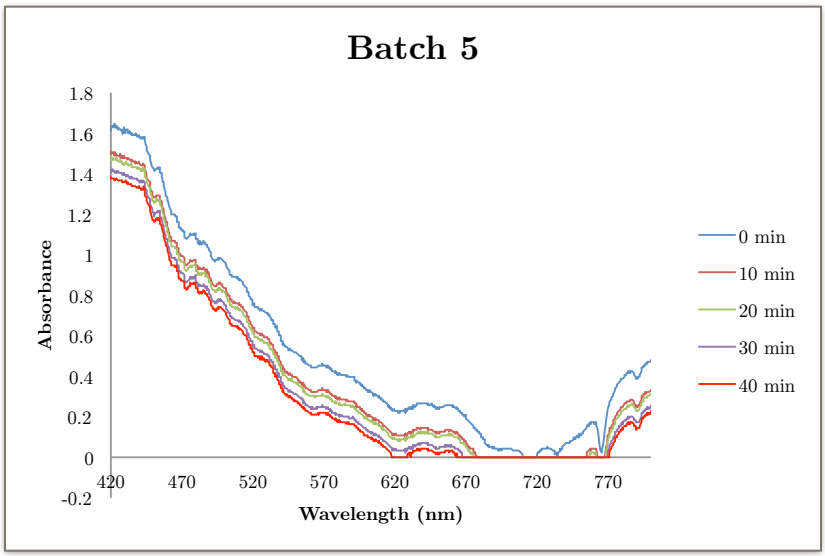

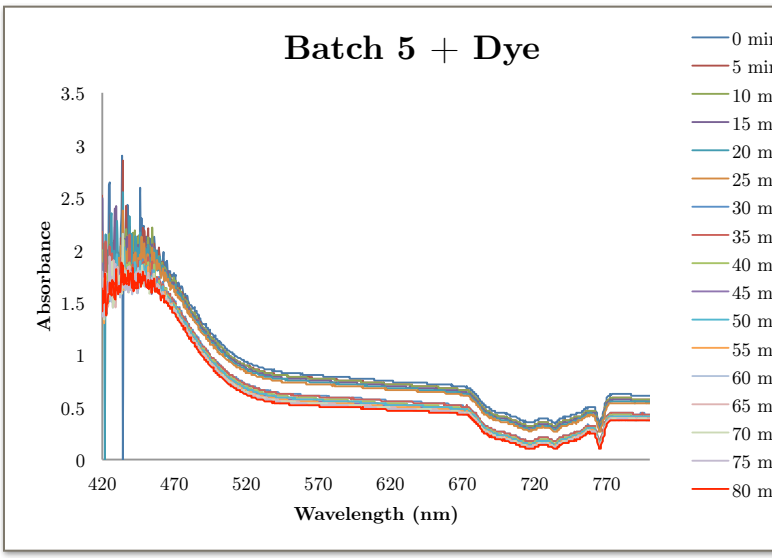

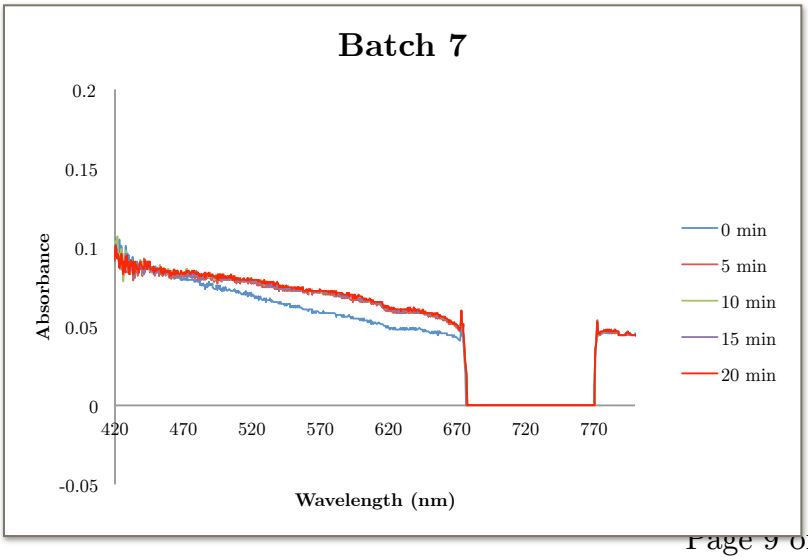

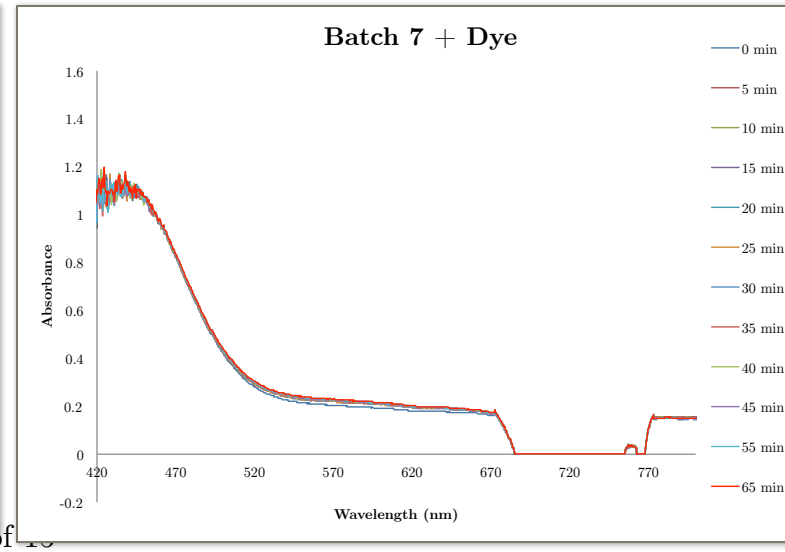

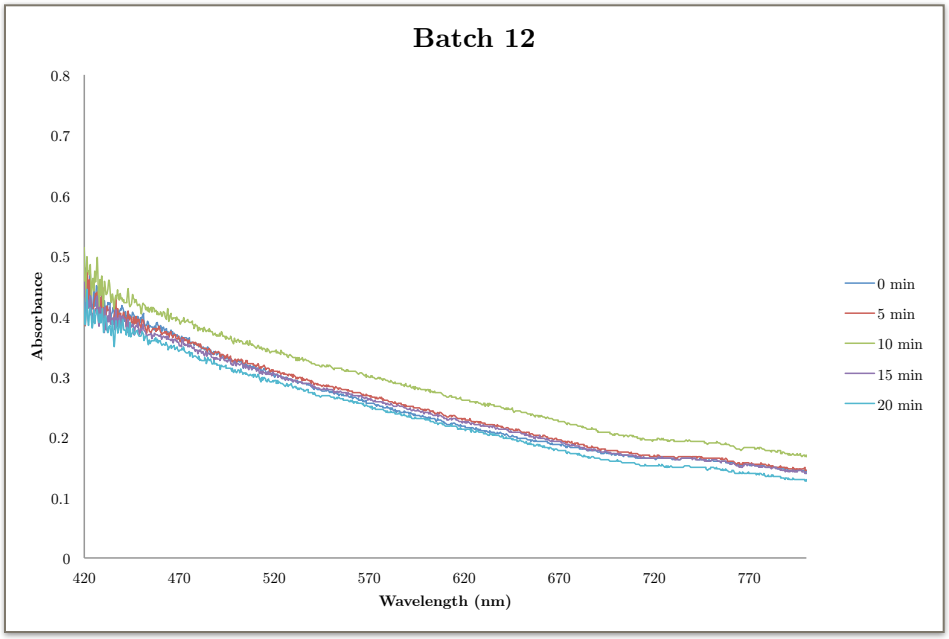

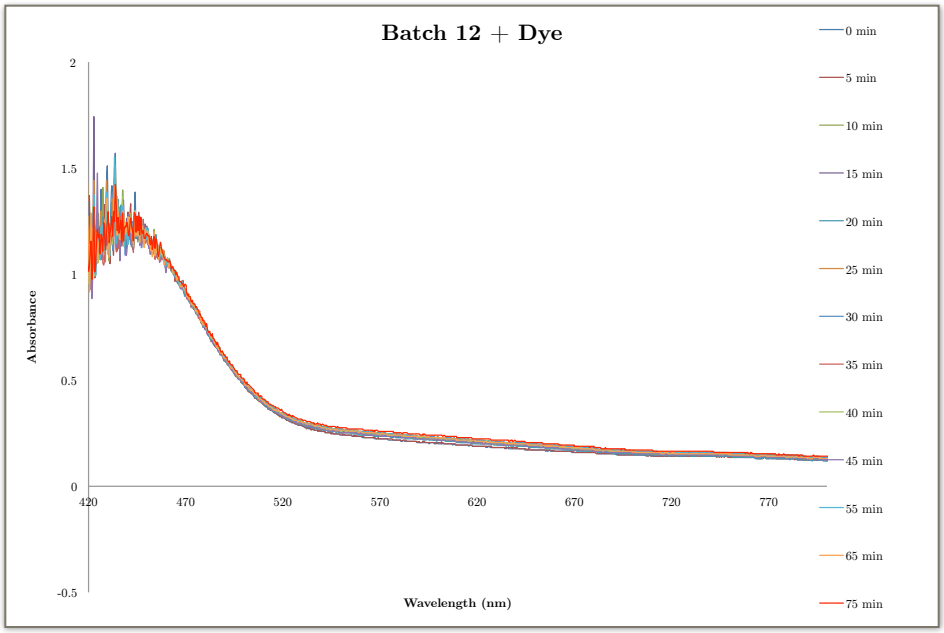

Figure S.4: Photocatalytic degradation of the photocatalyst alone and the photocatalyst with the dye for the batches that were discarded due to the formation of a precipitate.

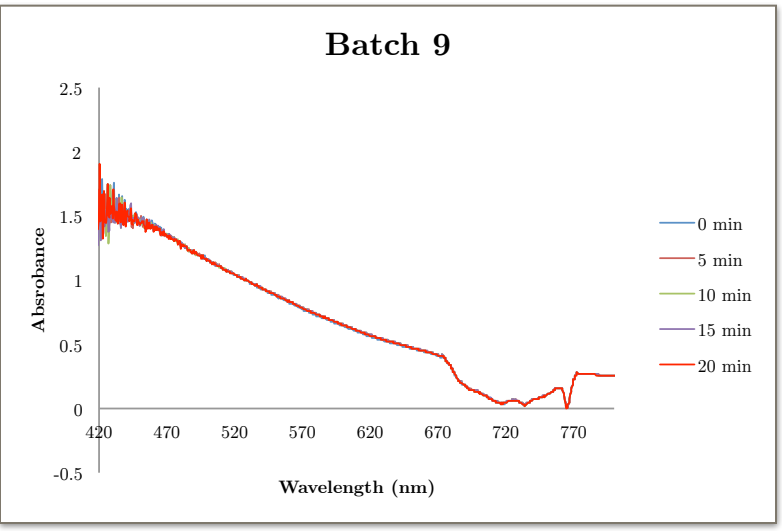
Batch 9
Absrobance
Wavelength (nm)
0 min
5 min
10 min
15 min
20 min

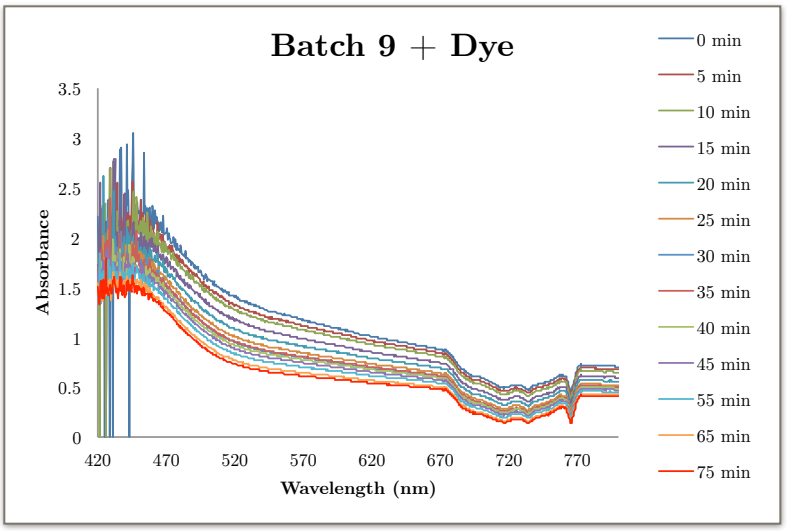
Batch 9 + Dye
Absorbance
Wavelength (nm)
0 min
5 min
10 min
15 min
20 min
25 min
30 min
35 min
40 min
45 min
55 min
65 min
75 min

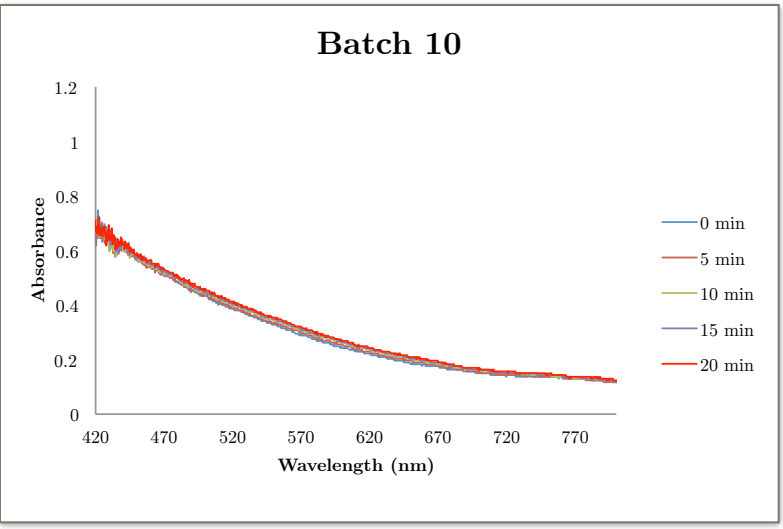
Batch 10
Absorbance
Wavelength (nm)
0 min
5 min
10 min
15 min
20 min

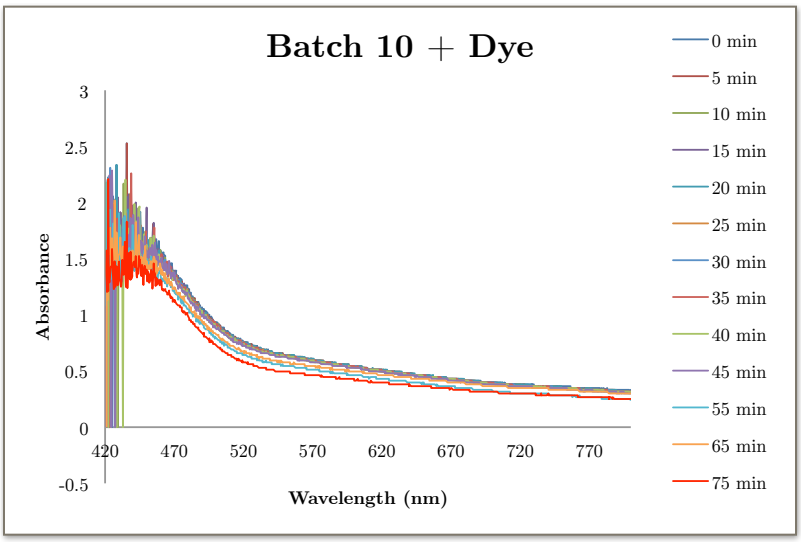
Batch 10 + Dye
Absorbance
Wavelength (nm)
0 min
5 min
10 min
15 min
20 min
25 min
30 min
35 min
40 min
45 min
55 min
65 min
75 min

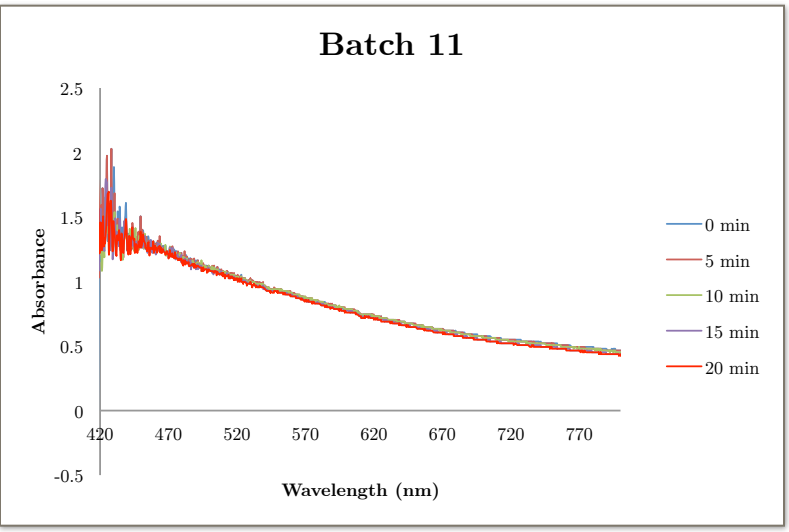
Batch 11
Absorbance
Wavelength (nm)
0 min
5 min
10 min
15 min
20 min

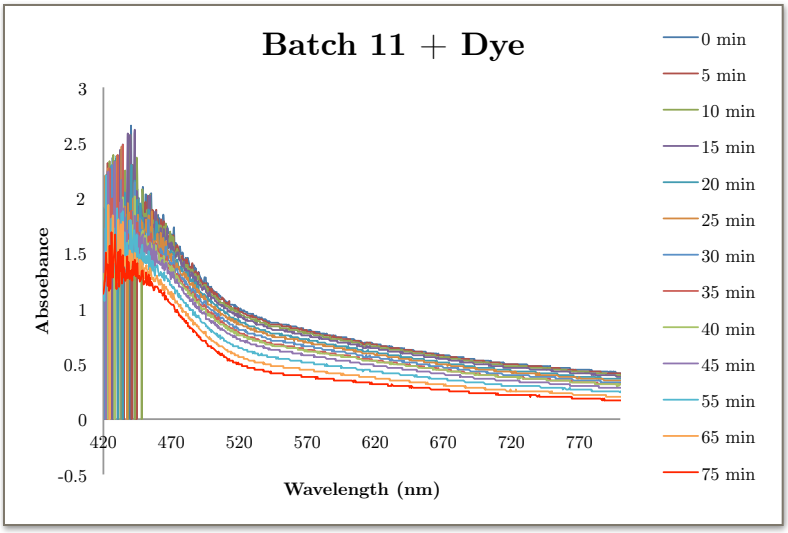
Batch 11 + Dye
Absoebance
Wavelength (nm)
0 min
5 min
10 min
15 min
20 min
25 min
30 min
35 min
40 min
45 min
55 min
65 min
75 min

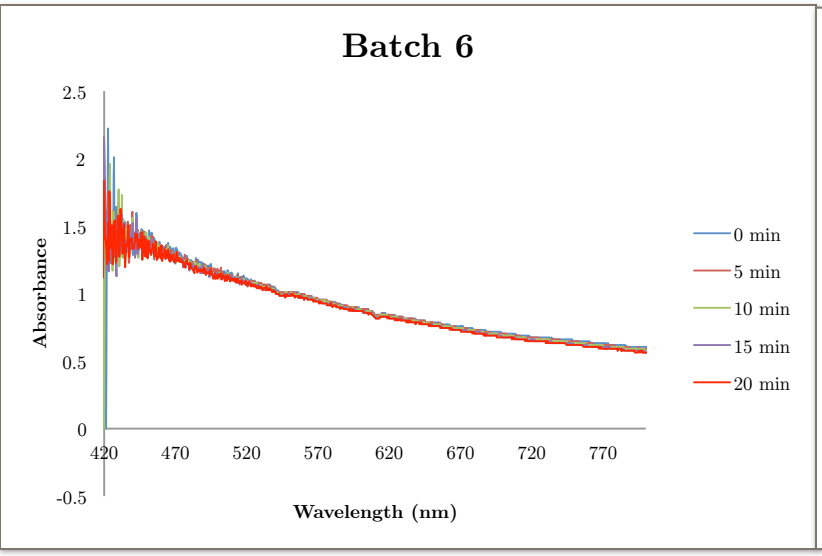

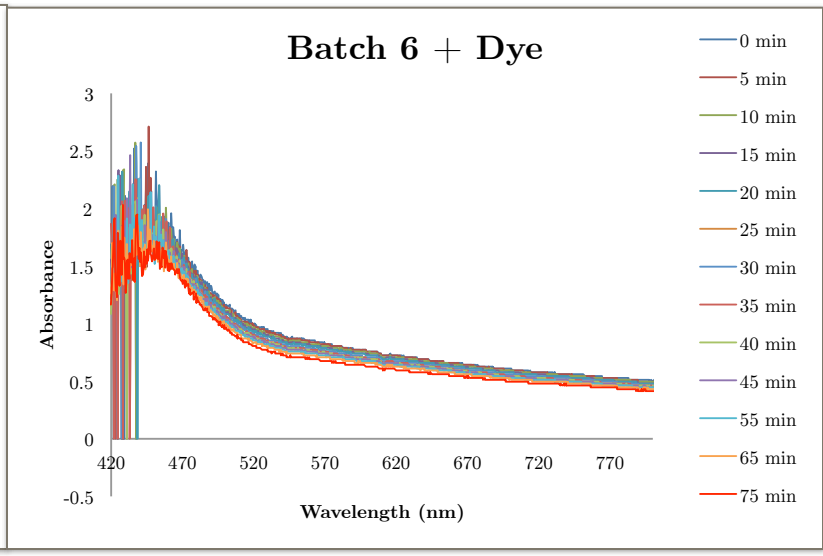

Figure S.5: Photocatalytic degradation of the photocatalyst alone and the photocatalyst with the dye for the batches that were not discarded and used for further analysis.

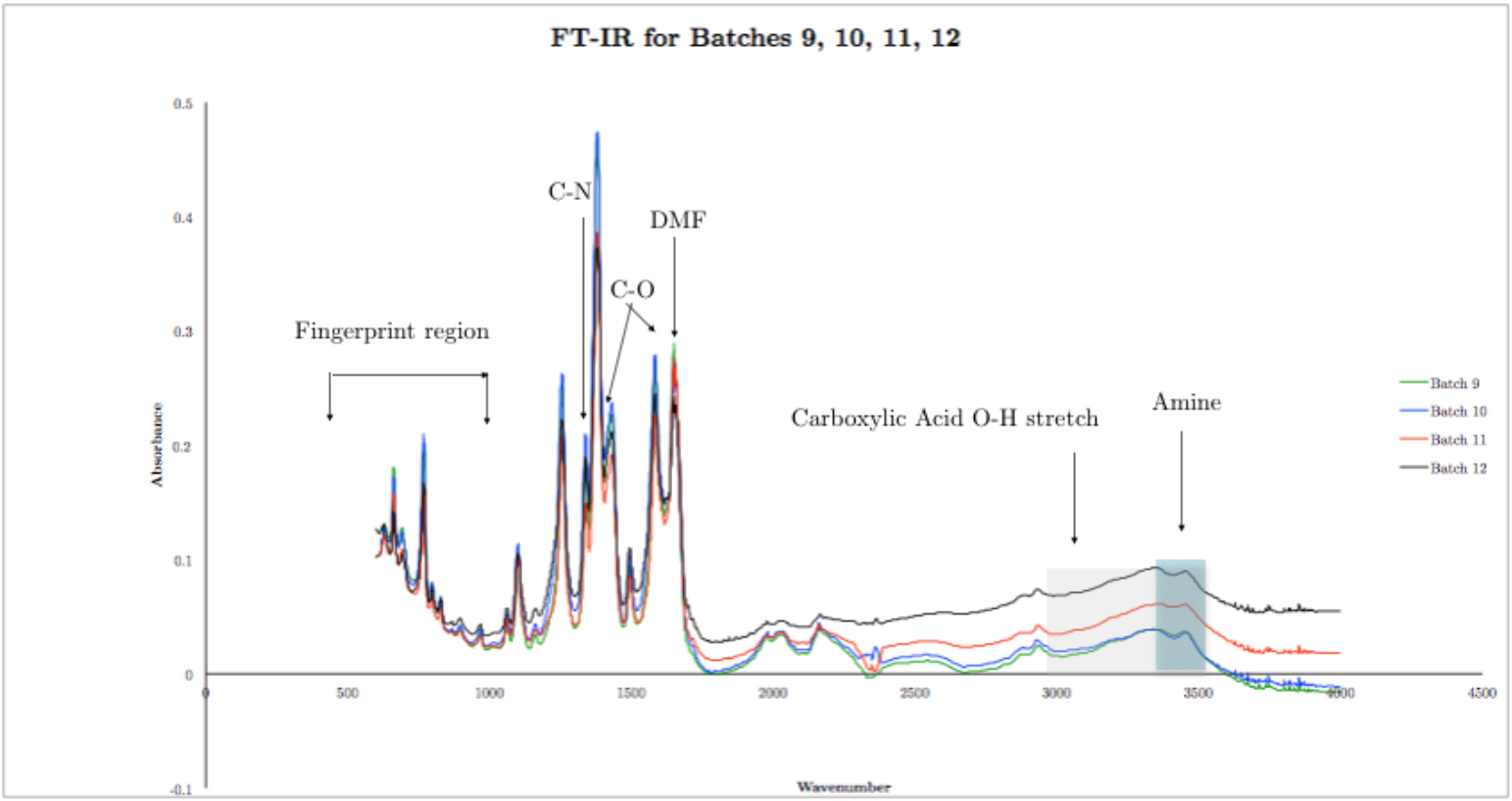

Figure S.6: Identification of major functional groups present in NH_2-MIL-101(Fe).

(a) The fingerprint region corresponds for each of the 4 batches, indicating they are the same structure, i.e. NH_2-MIL-101(Fe).

(b) A band at 1652 cm^{-1} indicates a C=O stretch, thus showing the presence of DMF molecules.

(c) The two bands at 1585cm^{-1} and 1435cm^{-1} correspond to the symmetric and asymmetric C-O stretching vibrations of carboxylates thus indicating the presence of 2-aminoterephtalic acid anions.

(d) Doublet around 3400cm^{-1} corresponds to the asymmetrical and symmetrical stretching of the amine moieties in 2-aminoterephthalic acid.

(e) Band at 1339cm^{-1} indicates the C-N stretching absorption distinctive of aromatic amines (2-aminoterephthalic acid)

(f) A wide band around 3000cm^{-1} indicates a carboxylic acid O-H stretch from the 2-aminoterephtalic acid.

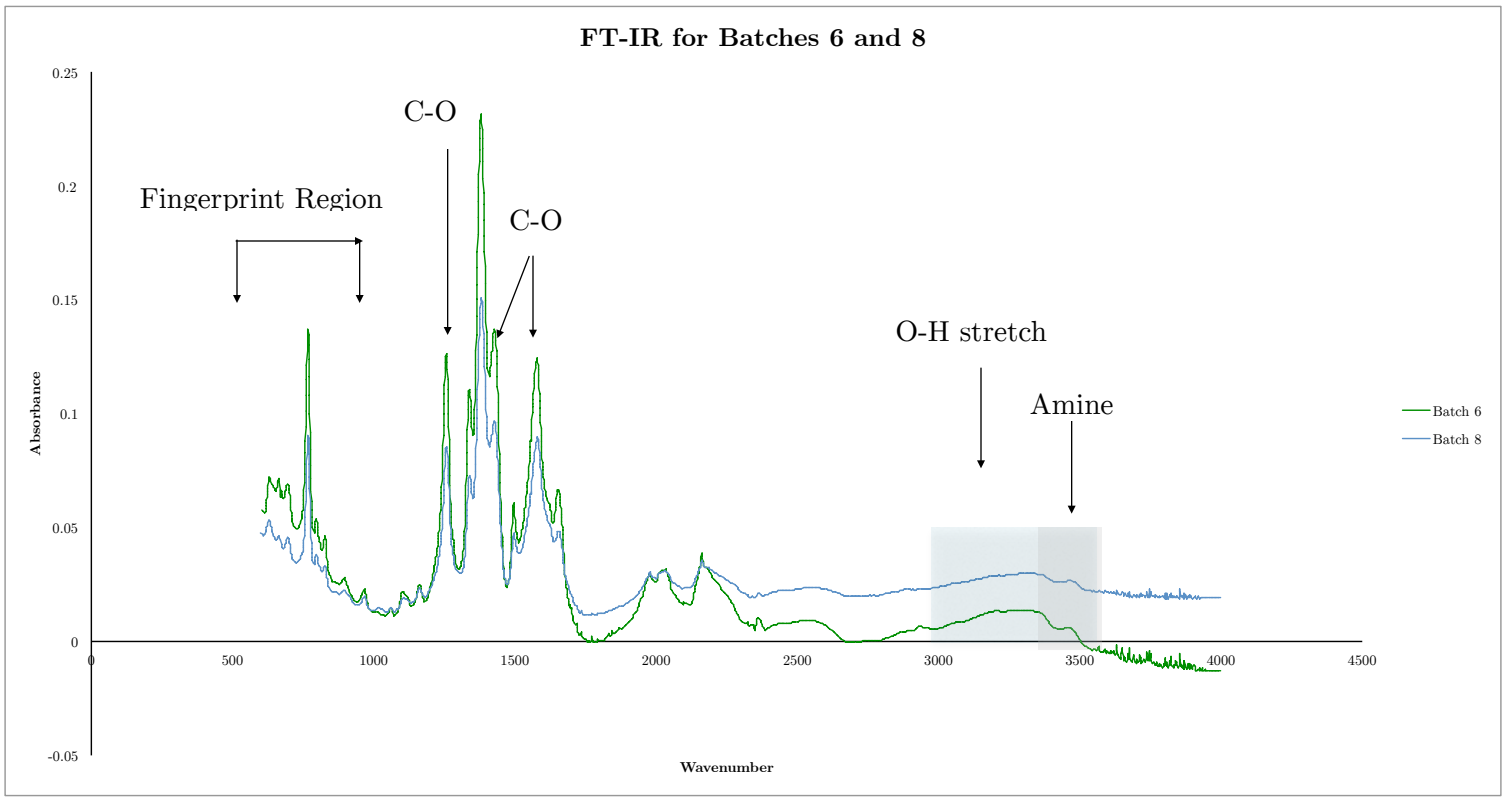

Figure S.7: Identification of major functional groups in NH_2-MIL-88(Fe).
(a) The fingerprint region is the same for both Batch 6 and Batch 8, indicating they are the same structure, i.e. NH_2-MIL-88B(Fe).
(b) A wide band around 3000cm^{-1} indicates a carboxylic acid O-H stretch from the 2-aminoterephtalic acid.
(c) Doublet around 3400cm^{-1} corresponds to the asymmetrical and symmetrical stretching of the amine moieties in 2-aminoterephthalic acid.
(d) The two bands at 1585cm^{-1} and 1435cm^{-1} correspond to the symmetric and asymmetric C-O stretching vibrations of carboxylates thus indicating the presence of 2-aminoterephtalic acid anions.
(e) A medium strength band is found at 1269cm^{-1} which is associated with the C-O stretch of H_2N-BDC.

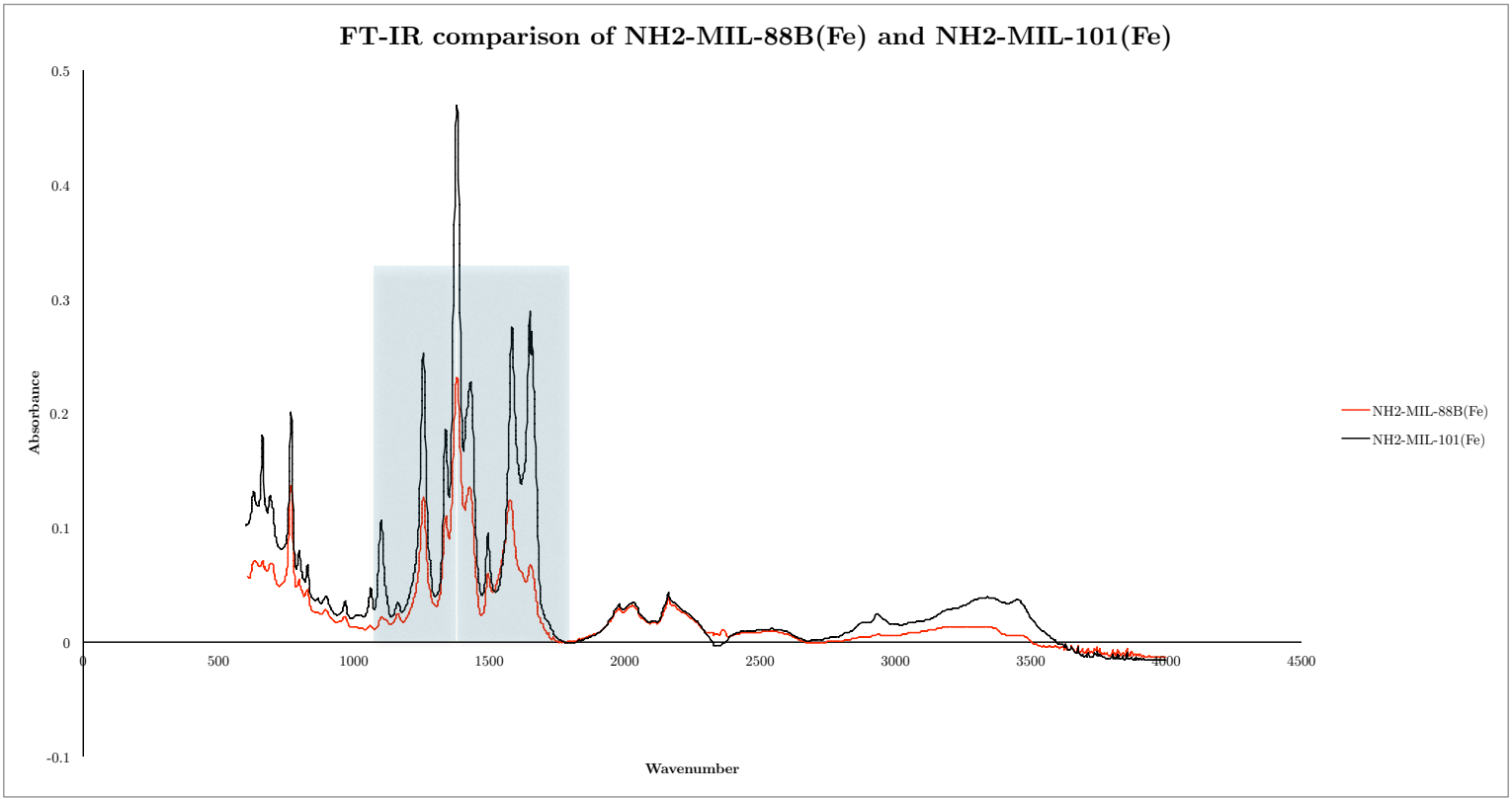

Figure S.8: The highlighted region shows the difference in the bands between NH2-MIL-88B(Fe) and NH2-MIL-101(Fe)

Iron Based Metal Organic Frameworks as Photocatalysts for Chromium (VI) Degradation

by
Deliana Dimitrova
3901599

APPENDIX 1A

Literature Review

Contents

List of Figures

List of Abbreviations

MOF-5: $Zn_4O(BDC)_3$

BDC: $C_8H_6O_4$

2,6-NDC: C10H6(CO2H)2

DMF: C_3H_7NO

UTSA-38: Zn_4O(2,6-NDC)3-(DMF)1.5(H_2O)0.5 · 4DMF·7.5H_2O

IRMOF1: $C_6H_4(CO_2H)_2$

IRMOF2: BrC_6H_3-1,4-$(CO_2H)_2$

IRMOF9: HO2CC6H4C6H4CO2H

IRMOF7: $C_{10}H_6(CO_2H)_2$

IRMOF8: $C_{10}H_6(CO_2H)_2$

MIL-53(Fe): $Fe(OH)\{O_2C–C_6H_4–CO_2\}$

MIL-100(Fe): $Fe_3O(H_2O)2F[C_6H_3(CO_2)_3)]_2$

Basolite F-300: $FeC_9H_3O_6$

MIL-101(Fe): NH_2 $Fe_3O(H_2O)2F[C_6H_4(CO_2)_2)NH_2]_3$

MIL-88B(Fe): $Fe_3O(CH_3OH)_3[C_6H_3(CO_2)_2]_3.CH_3CO_2.(CH_3OH)_{4.5}$

MIL-88B(Fe): $NH_2Fe_3O(CH_3OH)_3[C_6H_3(CO_2)2NH_2]_3.CH_3CO_2.(CH_3OH)_{4.5}$

MOF: Metal Organic Framework

OG: orange G

Rhb: rhodamine B

RBBR: Remazol Brilliant Blue R

MB: methylene blue

HOMO: highest occupied molecular orbital

LUMO: lowest occupied molecular orbital

Abstract

Metal Organic Frameworks (MOFs) are coordination polymers with interesting properties which allow for them to be applied in a variety of fields, such as drug delivery, sensor technology, gas separation, etc. One of the fields that has been particularly well-researched is photocatalysis. In fact, these compounds can be used as photocatalysts for the degradation of harmful pollutants that are released into the environment by a variety of industries. Hexavalent chromium is one such toxic heavy metal pollutant that needs to be removed from wastewater prior to its release into the environment ecosystem. The present research aims to synthesize MOFs which can function as photocatalysts for the degradation of this toxic compound, Cr(VI). In order for the research to be conducted, a thorough review of the literature on MOFs was conducted. First, the present review will describe the properties of MOFs which make them such unique structures and thus allow for their variable applications. Second, their specific application as photocatalysts for the degradation of pollutants will be explained. Next, a brief history of the MOFs that have been synthesized thus far will be provided. Subsequently, the recent boom in the synthesis of iron based MOFs will be reviewed. This literature review will thus provide a historical background of MOFs for their application in photocatalysis and will thus form the base knowledge for the present research study.

Chapter 1

Review of Metal Organic Frameworks

1.1 Introduction

Metal-Organic Frameworks (MOFs), a special group of coordination polymers, are a class of inorganic-organic hybrid porous molecules. These crystalline compounds are composed of metal nodes connected by organic bridging linkers which form strong metal-ligand interactions (Corma et al., 2010; Laurier et al., 2013; Wang et al., 2014). The design of MOFs has received great attention by the scientific community in recent years. The development of these chemical structures is moving at an extraordinary pace, as illustrated by the dramatic exponential increase in published research papers on the topic in the past two decades (Figure 1.1) (Long & Yaghi, 2009). These developments have been made due to the compounds' modular porous structure and diverse properties which make them widely applicable for gas storage, drug delivery, sensoring, and photocatalysis (Yang et al., 2014). The most extensive research on MOFs photocatalysis has been on the design of these compounds to serve as photocatalysts for the degradation of organic pollutants, which will be the main focus of this thesis (Zhang & Lin, 2014). Specifically, iron based MOFs as photocatalysts, or compounds that accelerate a photo-reaction, will be examined and their specific application in the degradation of polluting compounds in the environment. The present chapter will serve to provide a review of the literature concerning MOFs as photocatalysts which will include: (1) their unique properties, (2) their application as pollutant degraders, (3) and the history of these compounds as photocatalysts for pollutant degradation. Finally, the motivation and aim of the present research will be presented.

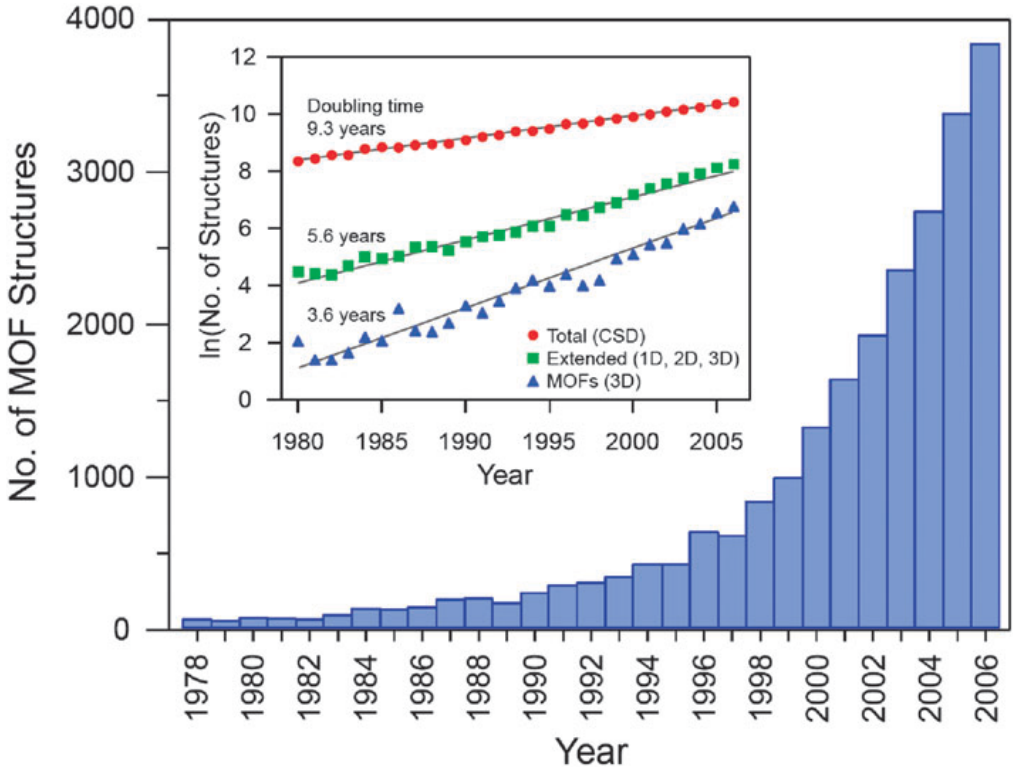

Figure 1.1 The amount of MOF structures that have been reported in the CSD (Cambridge Structural Database) in the years 1978-2006. The bar graph illustrates an exponential increase in the number of research papers of novel MOF structures. The inset shows the natural logarithm of the number of structures as a function of time (Long & Yaghi, 2009).

1.2 Properties of MOFs

MOFs, a subclass of coordination polymers, are metal-ligand 3 dimensional networks with metal nodes and bridging organic ligands with a crystalline structure and strong metal-ligand interactions (Corma et al., 2010; Laurier et al., 2013; Wang et al., 2014). The bonds linking the metal and ligand are stronger than hydrogen bonds and more directional than other weak interactions, such as π-π stacking (Corma et al., 2010). MOFs exhibit an unique combination of properties which make them a very extraordinary class of materials. They consist of a microporous structure which can have a surface area of up to $6000 m^2 g^{-1}$, thus exceeding traditional porous materials such as zeolites and carbons (Furukawa et al., 2010). Additionally, their pore volume has been measured to be up to 34Å (Férey et al., 2005; Corma et al., 2010). These values are among the highest reported for any material. Moreover, these materials are highly porous due to the presence of the strong metal-ligand interactions which allows for the removal of a solvent molecule without structural collapse of the framework. The most significant feature of MOFs is that their pore size, shape, dimensionality, and chemical environment can be finely altered by the selection of their metal and ligand building blocks. The MOF can act as a molecular sieve, by which molecules can diffuse through its pores. Alternatively, the MOF can interact with the guest molecule with transition states for the reactions formed within the scope of the pores (Corma et al., 2010). Synthesizing MOFs is usually performed by adding the molecular building blocks in solution or through hydro/solvothermal procedures as illustrated in Figure 1.2 (Janick & Vieth, 2010). Materials of this type are prepared using an approach known as "reticular chemistry" which involves linking of molecular building blocks into predetermined architectures that are held together by strong bonds (Yaghi et al., 2003). This possibility for modifying the organic ligands and consequently the pore size and shape allows tailoring the MOF material to suit the needs of a specific application. Their versatile properties (Figure 1.3) have enabled these compounds to be applied in processes including separation, drug delivery, sensor technology, and magnetism (Janick & Vieth,

2010). One particular application will be discussed in the following section — the photocatalytic degradation of dyes and heavy metal pollutants in industrial plant wastewater.

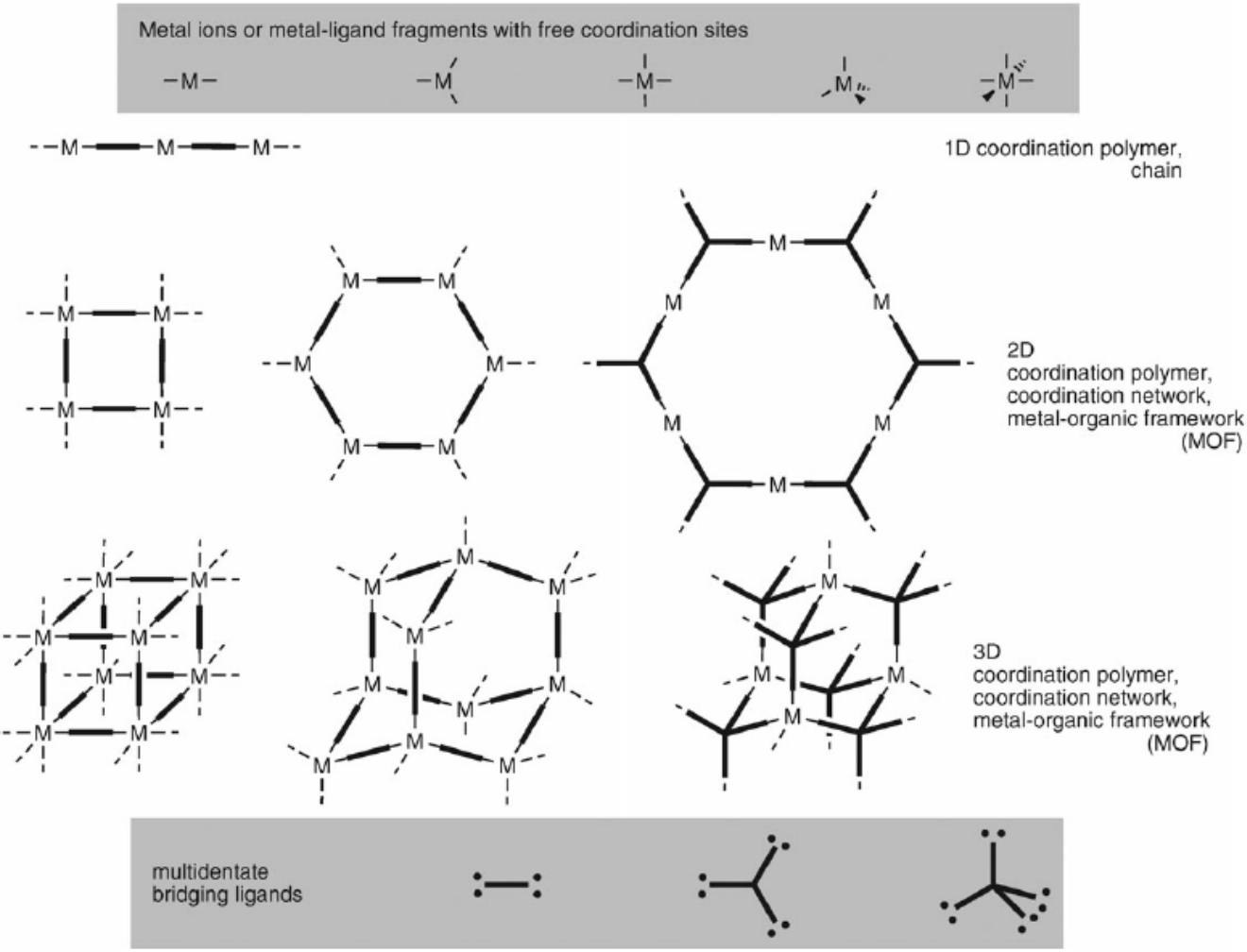

Figure 1.2 An illustration of how MOFs are constructed from molecular building blocks. MOFs can be constructed to be either 2 dimensional or 3 dimensional. (Janiak & Vieth, 2010)

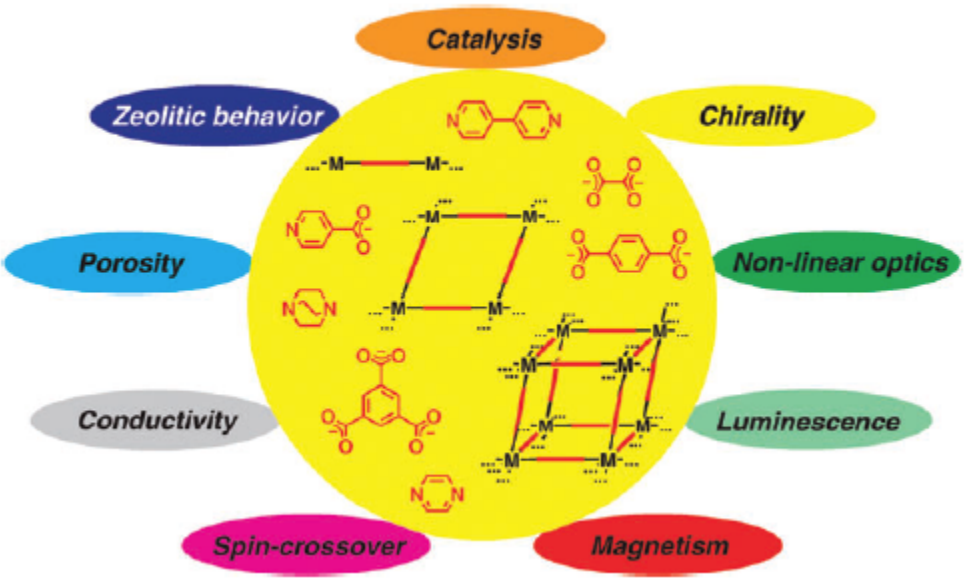

Figure 1.3 The unique properties of MOFs which can be used for a variety of applications, including catalysis, which has been a major focus in recent years. Some prototypical linkers are illustrated in the center. (Janiak & Vieth, 2010)

1.3 Photocatalytic Degradation of Organic Compounds with MOFs

Industrial plants produce high amounts of wastewater, which ultimately leads to environmental contamination. The wastewater may contain a variety of organic pollutants including organic dyes, phenols, pesticides, fertilizers, hydrocarbons, toxic heavy metals and so on. Dyes are of particular interest since there are more than 100,000 of them commercially available. Approximate 12% of synthetic dyes are lost during the manufacturing process and 20% of these end up the in industrial waste water (Hema & Arivoli, 2007). Their chemical stability and low biodegradability capacity in water makes them potentially harmful to the environment. Furthermore, dyes absorb and reflect sunlight entering the water, which interferes with the growth of bacteria to a level high enough to biologically degrade impurities in the water. Once these pollutants enter the aquatic ecosystem they may increase biochemical oxygen or interfere with aquatic biota; consequently, it is of major importance to seek a method to reduce organic pollutants in the wastewater before releasing it into the environment (Crini & Badot, 2010).

A particular chemical compound that is used in the production of textile dyes is hexavalent chromium [(Cr(VI)]. This toxic heavy metal is considered to be a primary pollutant for the environment by the U.S. Environmental Protection Agency (Testa et al., 2004). Cr(VI), as with other dyes, is released into the environment from industrial wastewater, including dye, leather, and wood manufacturing (Owlad et al., 2009). Unlike Cr(III), its natural chemical counterpart, Cr(VI) is mobile and highly toxic (Nriagu & Nieboer, 1998). In fact, long term exposure to this chemical can lead to liver damage, nerve tissue damage, and even death at extreme doses (Owlad et al., 2009). In addition, small levels of this chemical have been associated with toxic effects for bacteria, plants, and animals (Shanker et al., 2005). Cr(III) is not only less toxic, but also an essential element necessary for human metabolism (Richard & Bourg, 2001). Due to the concern for hexavalent chromium entering the ecosystem, governmental institutions worldwide

have implemented stringent laws regarding the release of these compounds (Shi et al., 2015). Industrial plants, such as the textile industry, use several conventional methods to clean the wastewater of hexavalent chromium prior to its release. These methods include chemical precipitation, membrane separation, adsorption, and ion exchange; however, these removal methods suffer a variety of limitations, such as high costs, high energy consumption, and generation of secondary pollutants (Rengaraj et al., 2007; Wang et al., 2014). A more effective method for the treatment of Cr(VI) is transforming it into its less toxic oxidation state mentioned previously, Cr(III). Fortunately, the novel of MOFs as photocatalysts can enable this conversion. A pivotal study performed by Shi et al. (2015) has recently shown that certain MOFs serve as efficient visible-light photocatalysts for the reduction of Cr(VI) to Cr(III). Thus, the reduction of Cr(VI) to Cr(III) has high potential in the field of industrial wastewater treatment and it can be achieved using MOFs as photocatalysts. Herein, the research progress of the application of MOFs in the photocatalytic degradation of industrial pollutants will be highlighted.

1.4 A Brief History

The first example of a compound with photocatalytic properties was developed by Fujishima and Honda (1972). They discovered that water can be split, i.e. simultaneously oxidized to oxygen and reduced to hydrogen. This pioneering discovery led to an increased interest by the chemical community to develop efficient photocatalysts that would be utilized for photochemical solar energy conversion. Soon, however, the focus of the research shifted to the area of environmental photocatalysis with the finding that TiO_2 can act as a photocatalyst for breaking down organic contaminants (Nasalevich et al., 2014). TiO_2 is a heterogeneous photocatalyst semiconductor and remains the most popular photocatalyst due to its low cost, low toxicity, and remarkable photochemical and chemical properties (Nath et al., 2012). The mechanism of how this particular heterogeneous photocatalyst works is illustrated in Figure 1.4. When the photocatalyst is excited by light, an electron hole pair is generated. Unlike metals which have a variety of electronic state, semiconductors (such as TiO_2) have an energy void, or band gap. Once excitation occurs across the band gap, the electron-hole pair undergo charge transfer to absorbed species on the semiconductor surface. Figure 1.4 shows that electron-hole pair recombination can occur at the surface or in the bulk of the semiconductor particle. Furthermore, photo-generated electrons can migrate to the surface of the semiconductor and lead to reduction of an electron acceptor or the photo-generated holes can migrate to the surface and lead to the oxidation of an electron donor. The last two processes illustrate the basic mechanism of photocatalysis (Linsebigler et al., 1995). Although TiO_2 has experienced great popularity, the catalyst suffers from several disadvantages, such as low photocurrent quantum due to electron hole recombination and low solar energy utilization resulting from its large band gap of 3.2 eV. Consequently, research has shifted to developing novel materials with a reduced band gap to enhance the response of the more abundant visible light photons (Laurier et al., 2013; Wang et al., 2014).

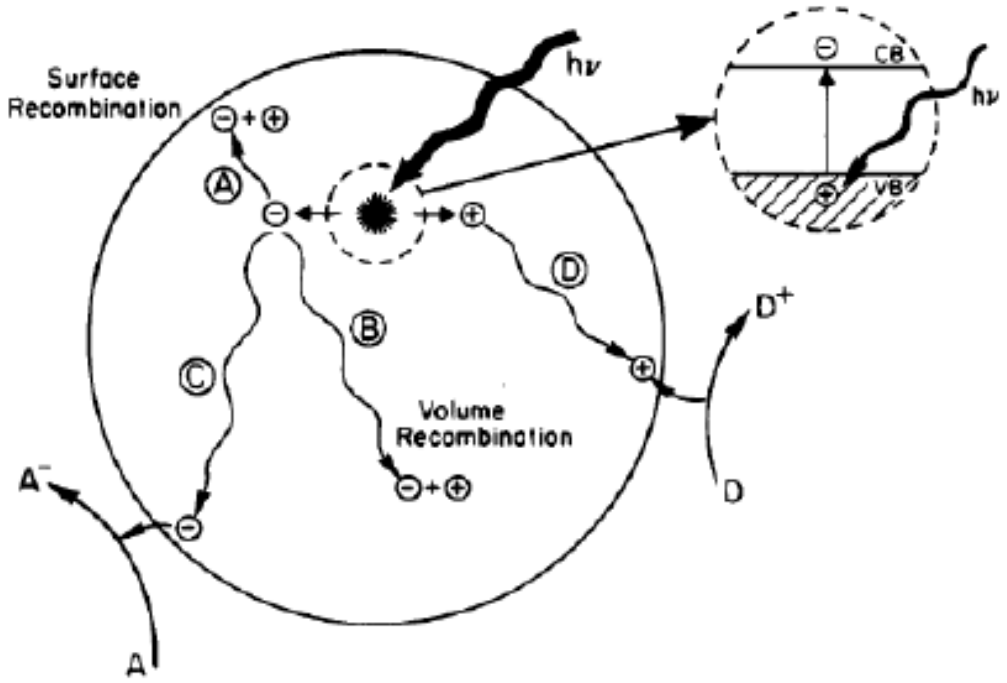

Figure 1.4 The mechanism of photo-excitation and de-excitation in a semiconductor, such as TiO_2. Four different de-excitation routes are possible (a-d). In a, recombination occurs at the surface of the particle. In b, recombination occurs in the semiconductor particle (volume recombination). In c, the photogenerated electrons migrate to the surface of the particle which consequently leads to reduction of an electron acceptor, A. Lastly, in d, the photogenerated holes can migrate to the surface leading to the oxidation of an electron donor, D.(Linsebigler et al., 1995)

Initially, a strategy employed was to dope TiO_2 with compounds such as nitrogen to enhance its optical response to the visible spectrum; however, these photocatalysts were ineffective because of their limited stability and high charge carrier recombination which is detrimental to catalytic performance (Asahi et al., 2001, Laurier et al., 2013; Rehman et al., 2009). The clear similarities between MOFs and transition metal oxides triggered the utilization of MOFs as an alternative platform for photocatalysis a decade ago (Nasalevich et al., 2014). Since some of these MOFs were proposed to act as semiconductors when exposed to light, just like TiO_2, they soon became potential candidates as photocatalysts (Wang et al., 2014). Furthermore, MOFs provide other advantages as photocatalysts, mainly due to their unique properties as discussed in the previous section. Firstly, their synthesis has high controllability and diversity due to the richness of the metal-containing nodes and organic linkers. In consequence, tailoring of the pore size or shape yields selectivity. Secondly, the separation of the heterogeneous catalyst is relatively easy (Wang et al., 2014). Third, being able to incorporate, lock, and shield the active site into a protective solid framework prevents problems that are associated with homogeneous catalysis, such as catalyst degradation and product or catalyst separation (Janiek & Vieth, 2010). Thus, d-block metal based MOFs' highly tunable properties attracted an intense interest by the scientific community to synthesize these compounds for the green degradation of industrial pollutants.

In 2007, Garcia and coworkers reported oxidative degradation of substituted phenols with MOF-5 under UV light. This pioneering study found that MOF-5, which is composed of Zn_4O tetrahedra joined by terephthalate linkers (Figure 1.5), was able to degrade phenol molecules. Furthermore, MOF-5 was found to degrade a bulkier phenolic molecule faster, indicating that the degradation process is likely to take place on the surface of the MOF. The possible mechanistic proposal by Alvaro et al. (2007) is illustrated in Figure 1.6 suggests that the degradation of phenol occurs through a series of reactions, including the initial formation of a radical cation by electron transfer from the phenol to a MOF-5 hole or the generation of oxygen reactive species by the reaction

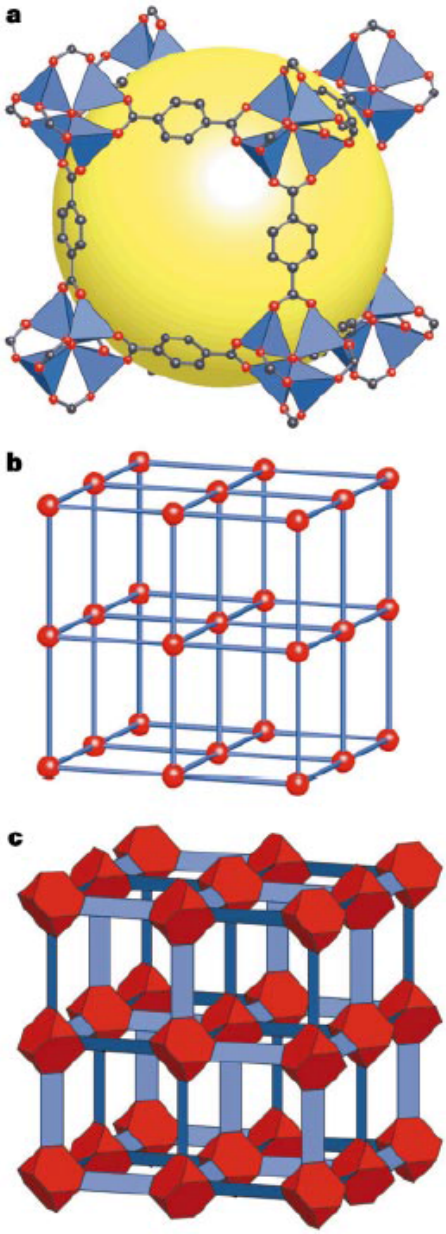

Figure 1.5 The MOF-5 structure. a) MOF-5 is composed of ZnO_4 tetrahedra (blue) connected by benzene decarboxylate linkers (O, red and C, black) to give an extended 3D cubic framework. b) The ball and stick model of the MOF-5 structure illustrating that the structure is a primitive cubic net. c) The structure shown as the envelopes of the $(OZn_4)O_{12}$ cluster (red tetrahedron) and benzene decarboxylate ion (blue slat). (Yaghi et al., 2003)

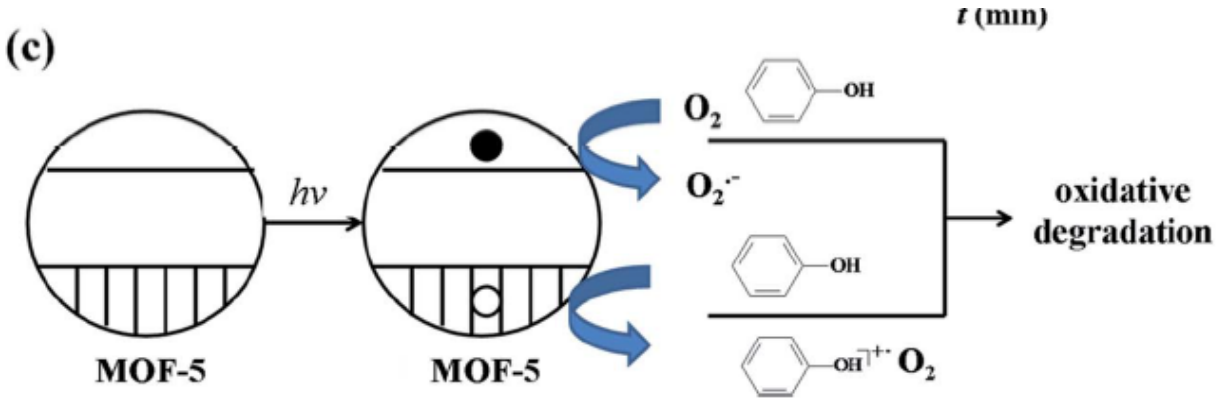

Figure 1.6 The degradation of phenol using MOF-5 as the photocatalyst. The oxidative degradation may occur through a series of reactions, including the initial formation of a radical cation by electron transfer from phenol to the MOF-5 or the generation of an oxygen reactive species by the reaction of the electrons with oxygen. (Alvaro et al., 2007)

of the ejected electrons with oxygen. Thus, MOF-5 was observed to behave as a semiconductor, similarly to TiO_2 (Alvaro et al., 2007). This initial research led to an increasing number of novel MOFs synthesized and tested as photocatalysts, as tabulated in Table 2 in Appendix 1B.

Further research tried to examine the relationship between the degradation efficiency of different organic dyes and band gap values. Mahata and co-workers (2006) synthesized three novel MOFs $[Co_2(4,40\text{-bpy})](4,40\text{-obb})_2$, $[Ni_2(4,40\text{-bpy})_2](4,40\text{-obb})_2.H2O$, and $[Zn_2(4,40\text{-bpy})](4,40\text{-obb})_2]$ with various band gap values to degrade a series of dyes including orange G (OG), rhodamine B(Rhb), Remazol Brilliant Blue R (RBBR), and methylene blue (MB). Organic dyes thus became the common method of examining photocatalytic activities of MOFs. The chemical structure of some common dyes used as surrogates for organic pollutants is illustrated in Table 1 in Appendix 1b. UV-vis absorption spectroscopy is a convenient way for monitoring dye degradation and consequently the activity of the MOF catalyst (Wang et al., 2014). The kinetic rates and degradation efficiencies of three MOFs were examined and were found to follow a reverse order with respect to their band gap values — the higher the band gap, the slower the degradation. A mechanism based on highest occupied molecular orbital (HOMO) and lowest occupied molecular orbital (LUMO) was proposed to account for this finding. In the absence of UV light, there are two electrons in the HOMO and none in the LUMO. In the presence of UV light, one electron transfers from the HOMO to the LUMO. The HOMO demands one electron to return to its stable state. The excited metal center decays to its ground state quickly. However, if some molecules are located within a reasonable range, transitional active complexes can be formed. For example, for RhB in this case one a-hydrogen atom of the methylene group bonded to the electron-withdrawing nitrogen atom in RhB would give its electron to the metal species (MOFs herein), and simultaneously form H+. This finally results in the cleavage of the C–N bond and stepwise N-deethylation of the RhB. Since the HOMO is then reoccupied, the excited electron must remain in the LUMO until it is captured by electronegative

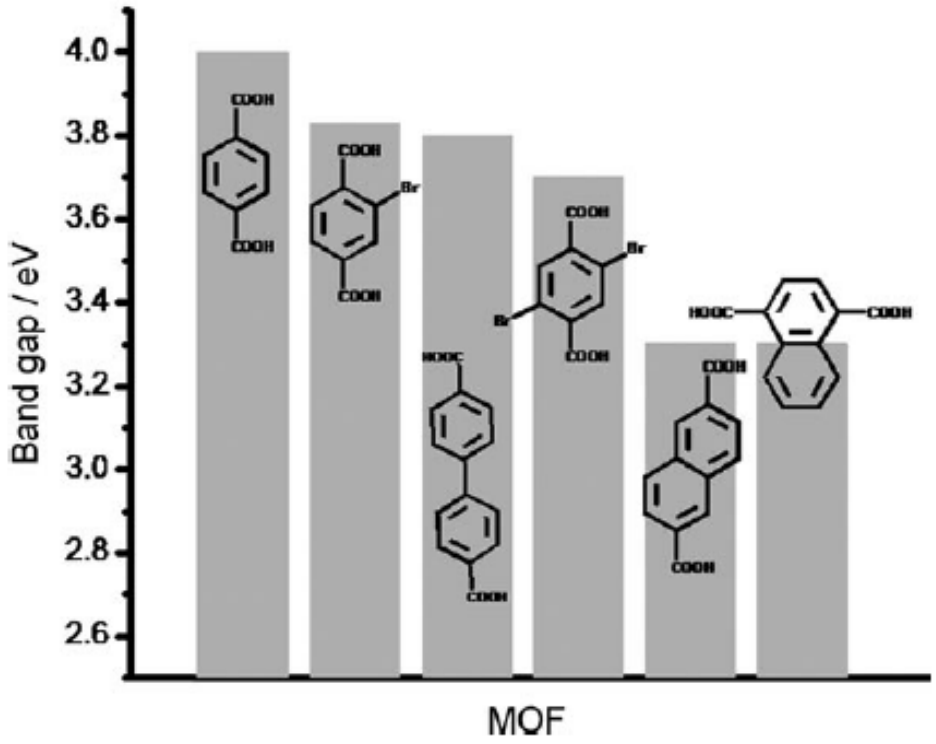

Figure 1.7 (a) The value of the band gaps for various isoreticular MOFs. This is the first evidence in the literature that the band gap energy of MOFs can be tuned by altering the organic linker (Gascon et al., 2008)

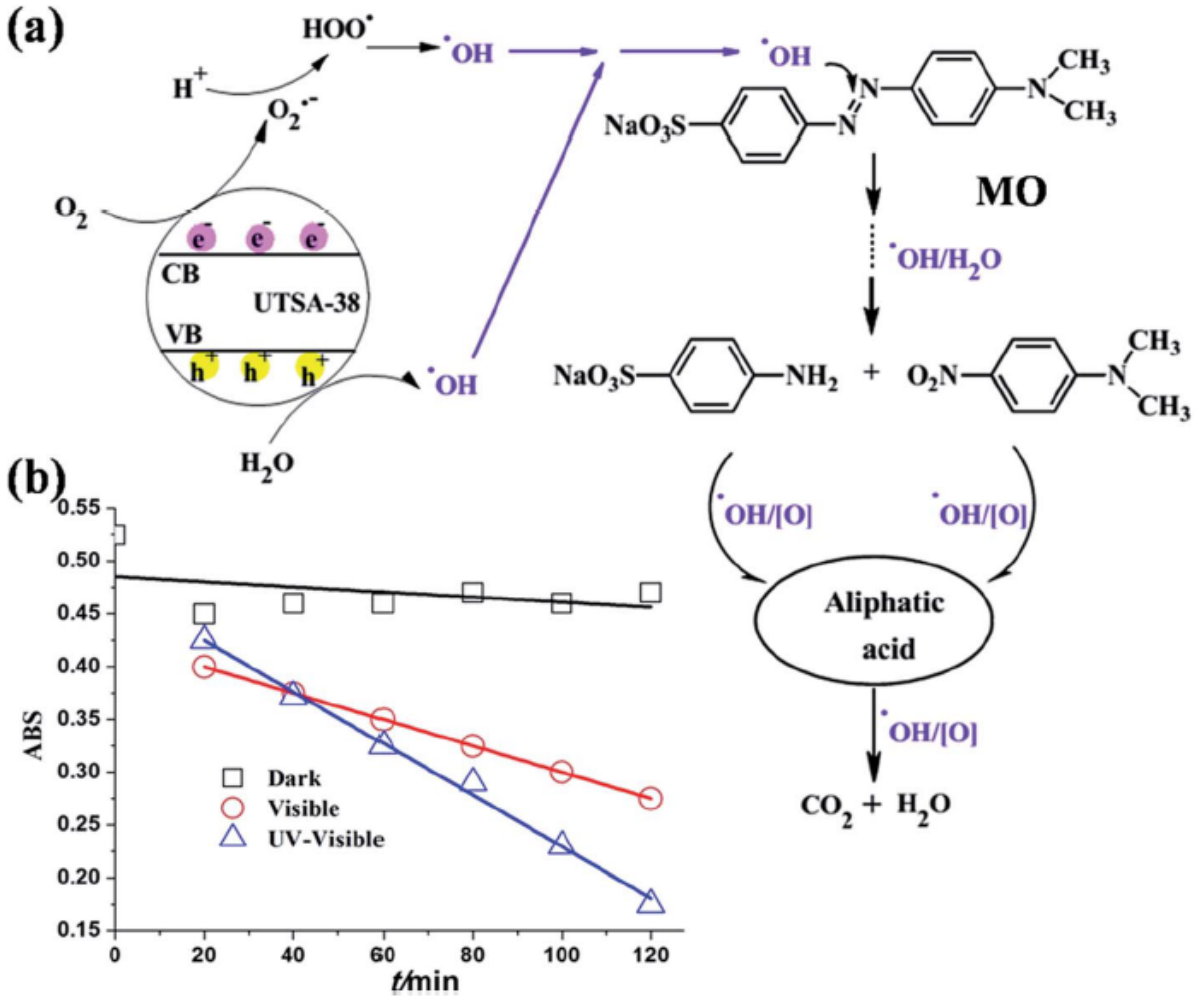

Figure 1.8 (a) The degradation of MO using UTSA-38 as the photocatalyst. First, electron hole pairs are generated in the UTSA-38. After absorption of energy equal or greater than the band gap of the photocatalyst, the electrons get excited from the valence band to the conduction band, leaving holes (h+) in the valence band. The electrons and holes migrate to the surface of the UTSA-38, then the photo-induced energy transfers to the absorbed species - electrons reduce oxygen to oxygen radicals and transform into hydroxyl radicals. In turn, holes oxidize the hydroxyl (H_2O) to hydroxyl radicals (OH). Hydroxyl radicals (OH) have the ability to decompose methyl orange effectively. (b) The absorbance of MO solution degraded by UTSA-38 as a function of irradiation time under UV-visible light, visible light and dark. (Wang et al., 2014)

substances such as molecular oxygen in solution, which would transform into the highly active peroxide anion and subsequently accomplish further oxidation and degradation of the substrate (Mahata et al., 2006; Wang et al., 2014).

Fuentes-Cabrera et al. (2005) examined the semiconductor behavior of the MOF-5 series by varying the metal (M) incorporated in the structure (M=Be, Mg, Ca, Zn, and Cd). They demonstrated that these materials theoretically have similar band gaps (3.5 eV), and hence the photo-physical properties cannot be significantly altered by variation of the composition of the inorganic corner positions. Alternatively, Gascon et al. (2008) reported the first evidence that the band gap energy of MOF-5 can be tuned by altering the organic linker (Figure 1.7). Isoreticular MOFs (same cubic symmetry but different pore sizes) were synthesized with different organic linkers; namely, IRMOF-1, IRMOF-2, 2,5-dibromoterephthalic acid, IRMOF-9, IRMOF-7, and IRMOF-8. The functional groups selected by the researchers were electron donating by the resonance effect. The researchers hypothesized that the effect of the linker could be related to resonance effects.

The discovery of the MOF-5 photocatalyst motivated Des and coworkers (2011) to design a more efficient photocatalyst. The researchers were the first to synthesize a doubly interpenetrated porous MOF, UTSA-38. UTSA-38 exhibited photocatalytic activity for the degradation of Methyl Orange (MO) in aqueous solution under both UV and visible light radiation, with the photocatalytic activity being higher when the catalyst was exposed to UV radiation. The proposed scheme for photocatalytic degradation occurred is illustrated and explained in Figure 1.8.

There is a general consensus in the research on the observation that the recombination of photo generated hole-electron pairs limits the rate of photocatalytic degradation (Sun et al., 2002; Wang et al., 2014). It has previously been found that the presence of H_2O_2 could produce hydroxyl radicals quicker thus enhancing the ability of the MOF to degrade dyes. In order to create better photocatalysts, Wen and coworkers investigated the synergistic effect of H_2O_2 and MOF $[Cd(btec)_{0.5}(bimb)_{0.5}]$ on the

degradation of the textile dye X3B. Not surprisingly the degradation rate constant was 1.8 times higher with H_2O_2 than without the H_2O_2 (Wen et al., 2012). Du and coworkers (2011) used MIL-53(Fe) to decompose MB. MIL-53(Fe) was considered to be an effective photocatalyst, since it contained empty d orbitals in Fe(III) just like the TIO2 semiconductor which contains empty 3d orbitals. The results showed that MIL-53(Fe) exhibited efficient photocatalytic properties for MB degradation under both UV-vis and visible light irradiation, even if the photo-degradation rate was relatively low. This relatively low degradation rate could potentially be attributed to the recombination of photo-generated holes and electrons, which always leads to reduced holes for the degradation of organic dyes. By introducing inorganic oxidants (H_2O_2, $KBrO_3$, and $(NH_4)_2S_2O_8$), the degradation rate increased owing to the fact that these compounds could suppress the electron-hole pair recombination.

Next, research focused on the factors that may effect degradation efficiency, such as pH, initial dye concentration, scavenging agents, anions, catalyst doses, temperature, and so on. Ai and co-workers (2014) explored the influence of pH, H_2O_2 dosage, and initial dye concentration on the degradation of RhB over the MIL-53(Fe)/H_2O_2 system. The catalyst worked effectively over a pH range from 3.0 to 9.0; however, the degradation rate degreased from 5.0-9.0 which could be attributed to the fact that H_2O_2 has low stability in alkaline medium. The optimal dye concentration ranged from 5 to 10 mgL^{-1} since increased dye concentration would enhance contact between oxidizing species and dye molecules; however, the activity decreased with a higher concentration since the solution would become less permeable to light. H_2O_2 was optimal from 5-20 Mm since more hydroxide radicals would be produced; with a higher concentration, the hydroxide radicals would generate perhydroxy radicals with lower potential.

Thus, the present section gave a brief history of MOF synthesis in the application of photocatalysis. The following section will review the recent research which specifically focuses of MOFs with iron as a metal node.

1.4.1 Iron Based MOFs

Due to its high abundance, stability, nontoxic nature, and small band gap, iron (III) has become a promising candidate for the development of photocatalysts which could capture light from the visible spectrum. One drawback of this compound is that it has high electron-hole recombination. Fortunately, this can be overcome by downsizing the photocatalytic particles through the generation of iron based MOFs built from Fe(III)-oxide clusters in combination with various organic linkers. The MOFs discussed thus far have not been efficient because they mostly function under UV light (Laurier et al., 2013). Fe(III), on the other hand, offers a novel method of capturing visible light for the application in MOF photocatalysis. For this reason, iron based MOF photocatalysts have become an interest for researchers in the past decade. Table 3 in Appendix 1B shows a compilation of some of most recent research articles which report the synthesis of iron(III) based MOFs. In the following paragraphs, a brief overview of these findings will be presented which will ultimately lead to the research question of the present thesis.

In 2005, Draznieks et al. synthesized MIL-88(Fe), which is an iron(III) carboxylate MOF. The researchers found that when water or various alcohols are absorbed within the porous structure, the crystallized framework become highly flexible. In fact, the three dimensional structure exhibited large swelling and almost a reversible doubling of its cell volume while still retaining its open-framework topology. This finding is revolutionary in the sense that it paves the way for MOFs as used for absorption of a range of organic molecules and gases. In comparison to zeolites, these structures were much more flexible and adaptable. Next, Horcajada et al. (2007) synthesized the iron (III) carboxylate MIL-100. The researchers performed Friedel-Crafts benzylation to show that this MOF is suitable as a catalyst. The results of the catalytic tests are illustrated in Figure 1.9. The figure shows the benzyl chloride conversion in the Friedel–Crafts benzylation of benzene over different catalysts, including MIL-100(Fe), MIL-100(Cr),

and 2 zeolites. It can be concluded from the figure that MIL-100(Fe) gives both activity and selectivity for this conversion. The researches hypothesize that the high benzylation activity might be due to the redox property of the trivalent iron special which could play an important role in activating both reactants.

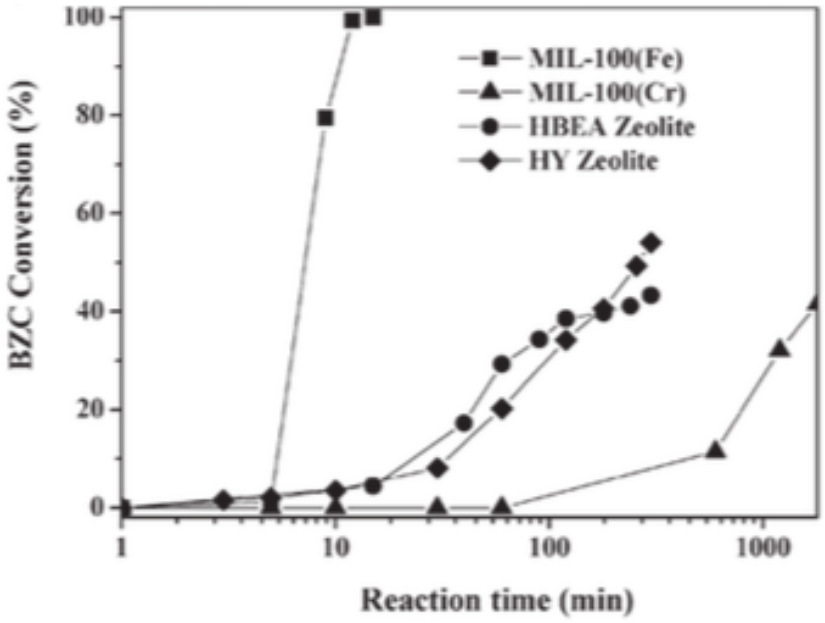

Figure 1.9: Friedel-Crafts reaction. The conversion of benzyl chloride in the liquid phase benzylation of benzene by benzyl chloride (BZC) to diphenylmethane (DPM) with MIL-100(Fe), MIL-100(Cr), and two zeolite catalysts (Horcajada et al., 2007).

With the fueled interest into these MOFs, Bauer et al. (2008) performed a high-throughput study to determine which synthesis conditions are important for the efficiency of these MOF photocatalysts. Specifically, Bauer and colleagues synthesized MIL-53, MIL-88, MIL-101, MIL-53(Fe)_NH_2 , MIL-88B(Fe)_NH_2, MIL-101(Fe)_NH_2. The synthesis of these hybrid solids is very sensitive to different parameters and leads to a formation of different hybrid phases. The nature of the reaction medium has the most profound impact on structure formation of MOFs. Additionally, the researchers reported that the concentration of the starting mixture and the temperature are both key parameters for the formation of various hybrid phases.

Laurier et al. (2013) performed a study in which they used small iron(III) oxide clusters as inorganic nodes in hybrid photocatalytic materials. They synthesized four MOFs - MIL-100(Fe), MIL-101(Fe)_NH_2, MIL-88B(Fe), and MIL-88B(Fe)_NH_2, They then compared their absorbance of light and photocatalytic activity with the standard semiconductor photocatalyst, TiO_2. RhB was successfully degraded under visible light illumination with different iron(III)-based MOFs consisting of Fe_3-μ3-oxo clusters. For the first time, the photocatalytic efficiency of such Fe(III)-based MOFs under visible light illumination was shown. Interestingly, linker modification with an amino group did not increase photocatalytic activity, Thus, these particular MOFs pose to be potentially effective photocatalysts that can function under visible light. However, the photochemical mechanism in these materials is unknown to the authors and further investigation into these coordination compounds is crucial in their understanding.

In 2015, Dadfarnia et al. reported on the photocatalytic degradation of methyl red using iron based MOFs loaded onto an iron oxide nanoparticle absorbent [Fe_3O_4@MIL-100(Fe)]. The researchers explored several parameters of the absorbent including its absorption capacity, thermodynamics, and kinetics. The effectivity of the MOF absorbent for the removal of methyl red was compared with another MOF, MIL-100(Fe) and iron-oxide nanoparticles. Overall, the results suggest that the novel absorbent nano-composite exhibits an enhanced absorption capacity and could

potentially be utilized for the removal of methyl red from aqueous solutions. Another research performed on the catalytic properties of iron based MOFs was in 2014 by Wu et al. Their aim was to improve the utilization efficiency of MOF photocatalysts by preparing an iron(III) based MOF [MIL-88(Fe)] with graphene oxide composites. The photocatalytic activity of the MIL-88(Fe)@GO catalyst were explored through the degradation of MB and RhB under the exposure of natural sunlight. The MOFs photocatalytic activity was compared to that of GO and MIL-88(Fe). The results indicated that the MIL-88(Fe)@GO completely degraded the dyes the fastest, in only 30 minutes, thus indicating that it could be used as an efficient adsorbent for environmental remediation.

The most relevant study for the present research was performed in 2015 by Shi et al. The researchers synthesized both MIL-88B(Fe) and MIL-88B(Fe)_NH_2. They found that the former MOF had both a higher stability and efficiency for the photocatalytic Cr(VI) reduction under visible-light irradiation. The photocatalytic degradation with the various MOFs tested, including MIL-88B(Fe) and MIL-88B(Fe)_NH_2 is illustrated in Figure 1.10. This figure indeed shows that the amino substituted MIL-88(B) has a better photocatalytic performance compared to the other MOFs. The researchers further proposed a mechanism for this photocatalytic reduction of Cr(VI) by this MOF (Figure 1.11). When visible light hits the MOF, both the linker and the Fe_3-μ_3-oxo clusters become excited. The electrons from the iron clusters are able to reduce the chromium from its hexavalent to its trivalent form. The photo generated electrons in the organic linker then transfer to the Fe_3-μ_3-oxo clusters, which is also responsible for the Cr(VI) reduction. Indroducting an amine group into the MIL-88B(Fe) structure is able to promote electron transfer and reduce electron-hole pairs recombination, thus resulting in superior photocatalytic performance in comparison to the MIL-88B(Fe).

Thus, iron based MOFs have become a focus of MOF photocatalysis research in the 2000s. Iron based MOFs exhibit interesting properties, are capable of absorbing

visible light irradiation, and have been documented to be efficient and stable photocatalysts.

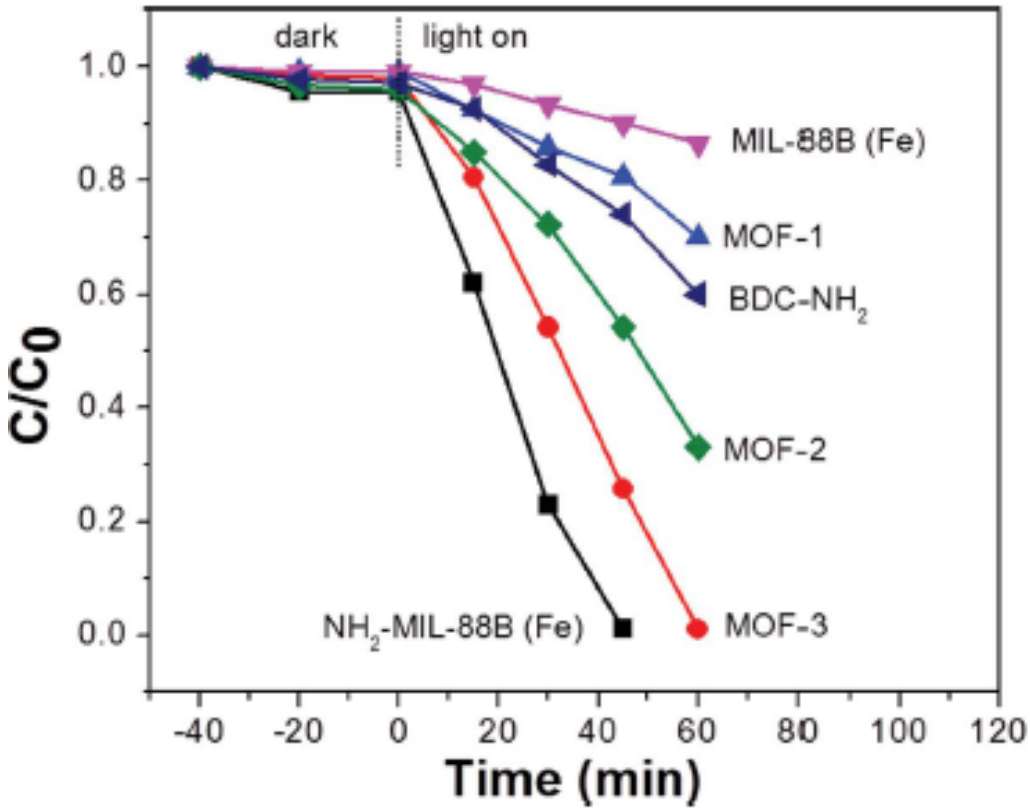

Figure 1.10: Photocatalytic reduction of Cr(VI) with several photocatalysts. These include: MIL-88B(Fe)_NH2, MOF-3, MOF-2, BDC-NH_2, MOF-1, MIL-88B(Fe). The amino substituted MIL-88B(Fe) shows the highest efficient in this reduction (Shi et al., 2015)

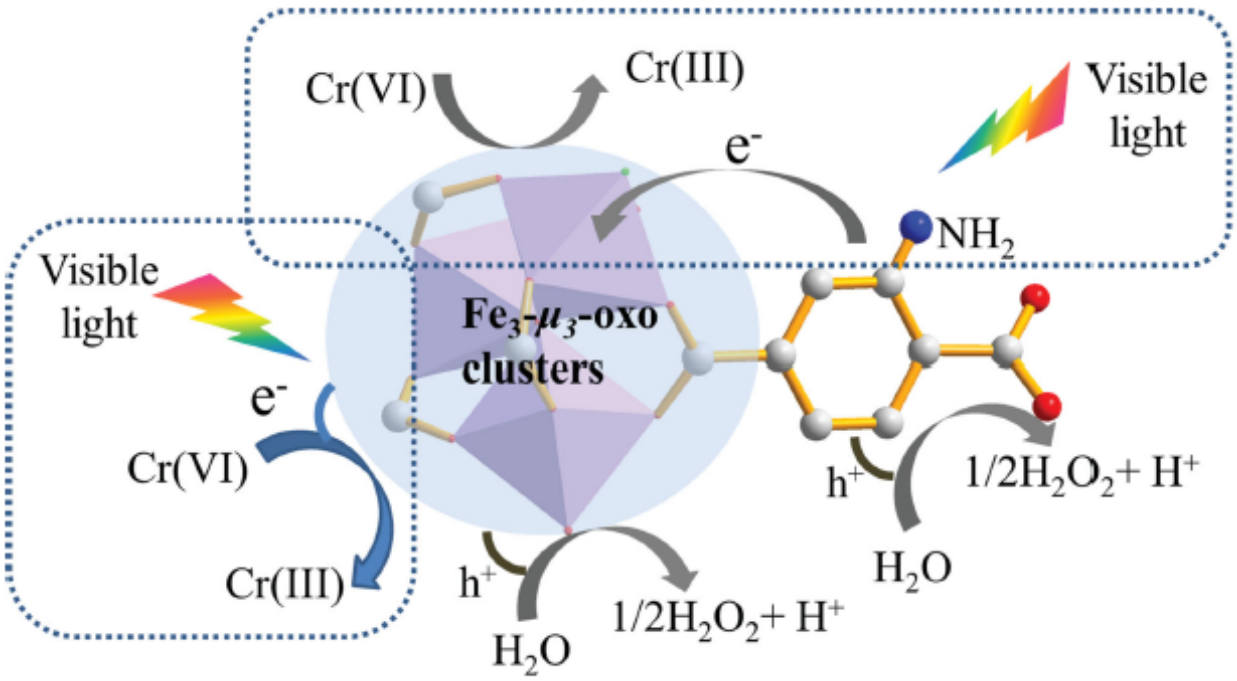

Figure 1.11: Proposed mechanism for the reduction of Cr(VI) to Cr(III) by MIL-88B(Fe)_NH_2. (Shi et al., 2015)

1.5 Discussion

The recent spur into research of MOFs for the specific application of photocatalysis has generated a multitude of findings. For researchers, the mechanism of how most MOFs degrade harmful pollutants, such as dyes, is of particular interest. This general mechanism for how most MOFs are capable of degrading harmful pollutants can be described simply through a reduction and an oxidation half reaction. Once light is absorbed, electrons and holes are generated in MOFs with reductive and oxidative power, respectively. Their charges are immobile within the structure which has implications for photocatalysis. Once the photo-generated holes and electrons are immobile, the oxidation and reduction sites stand in close proximity to the location where the photo-excited charges are generated. The spatial proximity of the photo-generated charge carriers favor charge recombination competing with the desired redox reaction. The porosity of the MOFs facilitates the diffusion of reactants and products through the crystal which might be able to compensate for the recombination (Navalevich et al., 2014). As mentioned previously, MOFs were initially labeled as semiconductors based on their optical, electrochemical, and photochemical properties. However, recently Nasalevich et al. (2014) highlighted that this semiconducting behavior is only present in a limited amount of MOFs. Rather, MOFs should be treated as catalysts rather than semiconductors and their photocatalysis mechanism should be based on HOMO-LUMO gap terminology. Thus, the band gap of MOFs is closely related to the HOMO–LUMO gap, which may be flexibly tuned through rational modification of the inorganic unit or the organic linker during synthetic procedures, thus the efficient light harvesting can be realized. However, the mechanism of how iron based MOFs function as organic compound degraders is yet to be elucidated on, which is why studying these compounds and their properties is particularly appealing.

1.6 Concluding Remarks and Aim of the Research

The recent boom in the synthesis of MOFs has largely been due to the diversity in their potential applications. In particular, these compounds have been observed to act as photocatalysts, therefore opening the gate for research into the area of pollutant degradation. Since environmental pollution, especially with dyes, is a serious problem, MOFs may indeed be the solution to cleaning up waste prior to its release into the environmental ecosystem. After the synthesis of the first MOF, MOF-5, a plethora of research has followed. The aim of most of the research has been to find a more effective photocatalyst by altering the properties of the MOF, such as its organic linkers and thus its pore size. The ability to construct a structure with such high variability makes these compounds highly attractive to researchers. The exponential growth in MOFs synthesized has largely been due to the fact that most MOFs thus far suffer from a variety of disadvantages. For instance, many MOFs have modest stability under photocatalytic conditions. Additionally, recent MOF photocatalysts mainly rely on Zr-carboxylate, Al-carboxylate, or Ti-carboxylate secondary binding units. Although they are robust enough to survive catalytic reactions, the lack of redox and photo activities limits the ability to utilize them as a functional component of in a multifunctional photocatalytic system. Expanding the SBU choices to redox and photo-active metals such as Fe will provide additional opportunities to functionalize both metal connection nodes and bridging ligands to enhance photocatalytic performances of MOFs.

In consequence, the present study's motivation stems from two recent research findings. First, Laurier and colleagues' (2013) reported that iron(III) based MOFs can function as more efficient photocatalysts than ones with other metal atom nodes. Specifically, these catalysts were seen to absorb light from the visible spectrum, which is an extraordinary finding since most previous MOFs, such as MOF-5, had their highest photocatalytic activity in the UV spectrum. Second, another study which inspired the present research is Shi et al. (2015). This study found that Fe(III) based MOFs with 2-

aminoterephthalic acid acid ligands are cable of reducing hexavalent chromium. These catalysts are yet to be further explored to optimize their linkers and consequently their photocatalytic activity. In the present study, the aim is to design several Fe(III) based MOFs with 2-aminoterephthalic acid linkers by altering the synthesis conditions. Their photocatalytic activity will subsequently be tested for the reduction of Cr(VI) which would give an indication of which MOF functions as the best catalyst. Since only a few articles have been published with these iron based MOFs, it is yet to be elucidated on what the crucial synthesis parameters are that control the photocatalytic activity of these coordination polymer. This study will thus evaluate which iron(III) MOF photocatalyst is the the most effective and further evaluate the chemical and structural reasons for the differences in photocatalytic activity between the MOFs.

1.7 Bibliography

Ai, L., Zhang, C., Li, L., & Jiang, J. (2014). Iron terephthalate metal–organic framework: Revealing the effective activation of hydrogen peroxide for the degradation of organic dye under visible light irradiation. *Applied Catalysis B: Environmental*, 148, 191-200.

Alvaro, M., Carbonell, E., Ferrer, B., Llabrés i Xamena, F. X., & Garcia, H. (2007). Semiconductor Behavior of a Metal-Organic Framework (MOF). *Chemistry-A European Journal*, 13(18), 5106-5112.

Asahi, R., Morikawa, T., Ohwaki, T., Aoki, K., & Taga, Y. (2001). Visible-light photocatalysis in nitrogen-doped titanium oxides. *Science*, 293(5528), 269-271.

Bauer, S., Serre, C., Devic, T., Horcajada, P., Marrot, J., Férey, G., & Stock, N. (2008). High-throughput assisted rationalization of the formation of metal organic frameworks in the iron (III) aminoterephthalate solvothermal system. *Inorganic chemistry*, 47(17), 7568-7576.

Corma, A., Garcia, H., & Llabrés i Xamena, F. X. (2010). Engineering metal organic frameworks for heterogeneous catalysis. *Chemical Reviews*, 110(8), 4606-4655.

Crini, G., & Badot, P. M. (2010). *Sorption Processes and Pollution: Conventional and Non-conventional Sorbents for Pollutant Removal from Wastewaters.* Presses Univ. Franche-Comté. Chicago

Dadfarnia, S., Shabani, A. H., Moradi, S. E., & Emami, S. (2015). Methyl red removal f from water by iron based metal-organic frameworks loaded onto iron oxide nanoparticle adsorbent. *Applied Surface Science,* 330, 85-93.

Das, M. C., Xu, H., Wang, Z., Srinivas, G., Zhou, W., Yue, Y. F., ... & Chen, B. (2011). A Zn_4O-containing doubly interpenetrated porous metal–organic framework for photocatalytic decomposition of methyl orange. *Chemical Communications*, 47(42), 11715-11717.

Du, J. J., Yuan, Y. P., Sun, J. X., Peng, F. M., Jiang, X., Qiu, L. G., ... & Zhu, J. F. (2011). New photocatalysts based on MIL-53 metal–organic frameworks for the decolorization of methylene blue dye. *Journal of hazardous materials*, 190(1), 945-951.

Férey, G., Mellot-Draznieks, C., Serre, C., Millange, F., Dutour, J., Surblé, S., & Margiolaki, I. (2005). A chromium terephthalate-based solid with unusually large pore volumes and surface area. *Science*, 309(5743), 2040-2042.

Fuentes-Cabrera, M., Nicholson, D. M., Sumpter, B. G., & Widom, M. (2005). Electronic structure and properties of isoreticular metal-organic frameworks: The case of M-IRMOF1 (M= Zn, Cd, Be, Mg, and Ca). *The Journal of chemical physics*, 123(12), 124713.

Fujishima, A., & Honda, K. (1972). Electrochemical photolysis of water at a semiconductor electrode. nature, (238), 37-38.

Furukawa, H., Ko, N., Go, Y. B., Aratani, N., Choi, S. B., Choi, E., ... & Yaghi, O. M. (2010). Ultrahigh porosity in metal-organic frameworks. *Science*, 329(5990), 424-428.

Gascon, J., Hernández-Alonso, M. D., Almeida, A. R., van Klink, G. P., Kapteijn, F., & Mul, G. (2008). Isoreticular MOFs as efficient photocatalysts with tunable band gap: an operando FTIR study of the photoinduced oxidation of propylene. *ChemSusChem*, 1(12), 981-983.

Hema, M., Arivoli, S. (2007) Comparative study on the adsorption kinetics and thermodynamics of dyes onto acid activated low cost carbon, *Int. J. Phys. Sci,* 2, 10–17.

Horcajada, P., Surblé, S., Serre, C., Hong, D. Y., Seo, Y. K., Chang, J. S., ... & Férey, G. (2007). Synthesis and catalytic properties of MIL-100 (Fe), an iron (III) carboxylate with large pores. *Chemical Communications*, (27), 2820-2822.

Horcajada, P., Salles, F., Wuttke, S., Devic, T., Heurtaux, D., Maurin, G., ... & Serre, C. (2011). How linker's modification controls swelling properties of highly flexible iron (III) dicarboxylates MIL-88. *Journal of the American Chemical Society*, 133(44), 17839-17847.

Janiak, C., & Vieth, J. K. (2010). MOFs, MILs and more: concepts, properties and applications for porous coordination networks (PCNs). *New Journal of Chemistry*, 34(11), 2366-2388.

Laurier, K. G., Fron, E., Atienzar, P., Kennes, K., Garcia, H., Van der Auweraer, M., ... & Roeffaers, M. B. (2014). Delayed electron–hole pair recombination in iron (iii)-oxo metal–organic frameworks. *Physical Chemistry Chemical Physics,* 16(11), 5044-5047.

Laurier, K. G., Vermoortele, F., Ameloot, R., De Vos, D. E., Hofkens, J., & Roeffaers, M. B. (2013). Iron (III)-Based Metal–Organic Frameworks As Visible Light Photocatalysts. *Journal of the American Chemical Society*, 135(39), 14488-14491.

Linsebigler, A. L., Lu, G., & Yates Jr, J. T. (1995). Photocatalysis on TiO2 surfaces: principles, mechanisms, and selected results. *Chemical reviews*, 95(3), 735-758.

Liu, Y. L., Zhao, X. J., Yang, X. X., & Li, Y. F. (2013). A nanosized metal–organic framework of Fe-MIL-88NH 2 as a novel peroxidase mimic used for colorimetric detection of glucose. *Analyst*, 138(16), 4526-4531.

Llabrés i Xamena, F. X., Corma, A., & Garcia, H. (2007). Applications for metal-organic frameworks (MOFs) as quantum dot semiconductors. *The Journal of Physical Chemistry*, 111(1), 80-85.

Long, J. R., & Yaghi, O. M. (2009). The pervasive chemistry of metal–organic frameworks. *Chemical Society Reviews*, 38(5), 1213-1214.

Ma, M., Bétard, A., Weber, I., Al-Hokbany, N. S., Fischer, R. A., & Metzler-Nolte, N. (2013). Iron-Based Metal–Organic Frameworks MIL-88B and NH2-MIL-88B: High Quality Microwave Synthesis and Solvent-Induced Lattice "Breathing". *Crystal Growth & Design*, 13(6), 2286-2291.

Mahata, P., Madras, G., & Natarajan, S. (2006). Novel photocatalysts for the decomposition of organic dyes based on metal-organic framework compounds. *The Journal of Physical Chemistry B*, 110(28), 13759-13768.

Mellot-Draznieks, C., Serre, C., Surblé, S., Audebrand, N., & Férey, G. (2005). Very large swelling in hybrid frameworks: A combined computational and powder diffraction study. *Journal of the American Chemical Society*, 127(46), 16273-16278.

Nasalevich, M. A., Van der Veen, M., Kapteijn, F., & Gascon, J. (2014). Metal–organic frameworks as heterogeneous photocatalysts: advantages and challenges. *CrystEngComm*, 16(23), 4919-4926.

Nath, R. K., Zain, M. F. M., & Kadhum, A. A. H. (2012). Photocatalysis—a novel approach for solving various environmental and disinfection problems: a brief review. *Journal of Applied Sciences Research*, 8(8), 4147-4155.

Nriagu, J. O., & Nieboer, E. (1988). *Chromium in the natural and human environments* (Vol. 20). John Wiley & Sons.

Owlad, M., Aroua, M. K., Daud, W. A. W., & Baroutian, S. (2009). Removal of hexavalent chromium-contaminated water and wastewater: a review. W*ater, Air, and Soil Pollution*, 200(1-4), 59-77.

Pham, M. H., Vuong, G. T., Vu, A. T., & Do, T. O. (2011). Novel Route to Size-Controlled Fe–MIL-88B–NH2 Metal–Organic Framework Nanocrystals. *Langmuir*, 27(24), 15261-15267.

Rehman, S., Ullah, R., Butt, A. M., & Gohar, N. D. (2009). Strategies of making TiO 2 and ZnO visible light active. *Journal of Hazardous Materials,* 170(2), 560-569.

Rengaraj, S., Venkataraj, S., Yeon, J. W., Kim, Y., Li, X. Z., & Pang, G. K. H. (2007). Preparation, characterization and application of Nd–TiO 2 photocatalyst for the reduction of Cr (VI) under UV light illumination. *Applied Catalysis B: Environmental*, 77(1), 157-165.

Richard, F. C., & Bourg, A. C. (1991). Aqueous geochemistry of chromium: a review. *Water Research*, 25(7), 807-816.

Shanker, A. K., Cervantes, C., Loza-Tavera, H., & Avudainayagam, S. (2005). Chromium toxicity in plants. *Environment international*, 31(5), 739-753. Chicago

Shi, L., Wang, T., Zhang, H., Chang, K., Meng, X., Liu, H., & Ye, J. (2015). An Amine-Functionalized Iron (III) Metal–Organic Framework as Efficient Visible-Light Photocatalyst for Cr (VI) Reduction. *Advanced Science*, 2(3).

Sun, Z., Chen, Y., Ke, Q., Yang, Y., & Yuan, J. (2002). Photocatalytic degradation of a cationic azo dye by TiO 2/bentonite nanocomposite. *Journal of Photochemistry and Photobiology A: Chemistry*, 149(1), 169-174.

Testa, J. J., Grela, M. A., & Litter, M. I. (2004). Heterogeneous photocatalytic reduction of chromium (VI) over TiO2 particles in the presence of oxalate: involvement of Cr (V) species. *Environmental science & technology*, 38(5), 1589-1594.

Wang, J. L., Wang, C., & Lin, W. (2012). Metal–organic frameworks for light harvesting and photocatalysis. *ACS Catalysis*, 2(12), 2630-2640.

Wang, C. C., Li, J. R., Lv, X. L., Zhang, Y. Q., & Guo, G. (2014). Photocatalytic organic pollutants degradation in metal–organic frameworks. *Energy & Environmental Science*, 7(9), 2831-2867.

Wen, L., Zhao, J., Lv, K., Wu, Y., Deng, K., Leng, X., & Li, D. (2012). Visible-light-driven photocatalysts of metal–organic frameworks derived from multi-carboxylic acid and imidazole-based spacer. *Crystal Growth & Design*, 12(3), 1603-1612.

Wu, Y., Luo, H., & Wang, H. (2014). Synthesis of iron (iii)-based metal–organic framework/graphene oxide composites with increased photocatalytic performance for dye degradation. *RSC Advances*, 4(76), 40435-40438.

Yaghi, O. M., O'Keeffe, M., Ockwig, N. W., Chae, H. K., Eddaoudi, M., & Kim, J. (2003). Reticular synthesis and the design of new materials. *Nature*, 423(6941), 705-714.

Yang, L. M., Fang, G. Y., Ma, J., Ganz, E., & Han, S. S. (2014). Band gap engineering of paradigm MOF-5. *Crystal Growth & Design*, 14(5), 2532-2541.

Zhang, T., & Lin, W. (2014). Metal-Organic Frameworks for Photocatalysis. *Metal-Organic Frameworks for Photonics Applications,* 157, 89-104.

Zhang, F., Shi, J., Jin, Y., Fu, Y., Zhong, Y., & Zhu, W. (2015). Facile synthesis of MIL-100 (Fe) under HF-free conditions and its application in the acetalization of aldehydes with diols. *Chemical Engineering Journal*, 259, 183-190.

Chapter 2

Review of Experimental Techniques

2.1 Introduction

In order to synthesize and characterize MOF structures, several techniques have been developed and utilized in the literature. Most commonly, a simple and relatively quick technique called solvothermal synthesis is used for the synthesis of these MOFs. For their characterization, Powder X-ray Diffraction (PXRD), Ultraviolet-visible Spectroscopy (UV-vis), and Fourier Transform Infrared Spectroscopy (FTIR) are often employed. The present research will utilize all of these techniques. The following chapter aims at reviewing the basic theory that explains these experimental techniques. This review will aid the reader in the background of the methods utilized in the present research study.

2.1 Solvothermal Synthesis

A conventional method for synthesizing MOFs is solvothermal synthesis (Tranchemontagne et al., 2008). Among the diverse synthetic methods used for the preparation and synthesis of solid materials, solvothermal methods have been the most effective and convenient, in particular for MOFs or other coordination polymers. (Zhao et al., 2010) A common definition for solvothermal reactions has not been clearly established (Stock & Biswas, 2011). Rabenau (1985) defines solvothermal reactions as reactions taking place in closed vessels under autogenous pressure above the boiling point of the solvent. The synthesis is straightforward. First, the metal salt and organic linker are placed in a polar organic solvent, typically and amine (triethylamine) or an amide (diethylformamide, dimethylformamide) (Czaja et al., 2009). The tube containing

the solution is stirred at room temperature in order to self assemble and then heated in a sealed system via conventional electric heating to solvothermal conditions for 24 hours (Czaja et al., 2009). Figure 2.1 illustrates the solvothermal synthesis method. This method yields MOF crystals that are suitable for further X-ray diffraction (XRD) analysis, but have the disadvantage of being relatively slow. Several reactions parameters have to be considered for solvothermal synthesis, including the composition of the reactions, the temperature and pressure, the concentration, reaction time, and pH to name a few. Additionally, since crystallization under these conditions is a non-equilibrium process, the cooling rate at the end of the reaction is also an important parameter. The solvent itself is also important, since some metal salts and/or organic ligands may have a low solubility and be insoluble in a given solvent. Introducing several solvents may increase the solubility (Zhao et al., 2010).

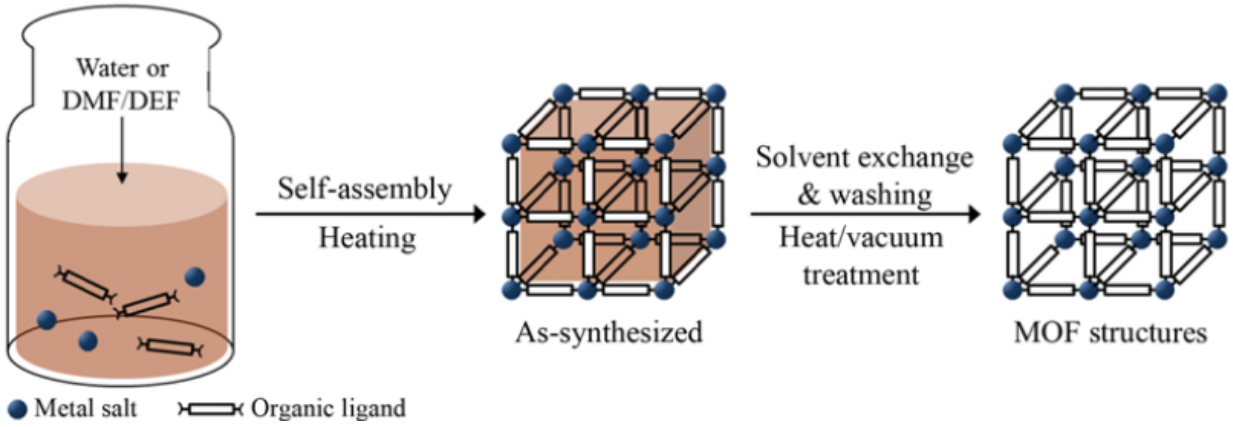

Figure 2.1 A scheme illustrating solvothermal synthesis of MOFs (Lee et al., 2013).

2.3 Powder X-ray Diffraction

PXRD is used to characterize a powdered (polycrystalline) sample containing a myriad of small crystallites typically of 0.1 to 10 μm in dimension (Atkins et al., 2010). The crystallites randomly adopt a whole range of possible orientations (Daan, 2000). When the X-ray beam strikes the polycrystalline sample, it is diffracted in all possible direction (Daan, 2000). Constructive interference occurs at some angles give by Bragg's equation (Equation 2.1) (Atkins et al., 2010). The derivation of Bragg's equation is shown in Figure 2.2. Each lattice spacing (d) gives rise to a cone of diffraction intensity (Atkins et al., 2010). Each cone is a set of closely spaced diffracted rays, where each dot represents the diffraction from a single crystallite within the powdered sample (Atkins et al., 2010). The large number of crystallites merge together to form a continuous diffraction cone, as illustrated in Figure 2.3 (Atkins et al., 2010).

$$n\,\lambda = 2\,d\,\sin\theta$$

Equation 2.1: Bragg's law, where n= an integer; λ = wavelength of rays; d = spacing between layers of atoms; ϑ = angle between the incident rays and the surface of the crystal.

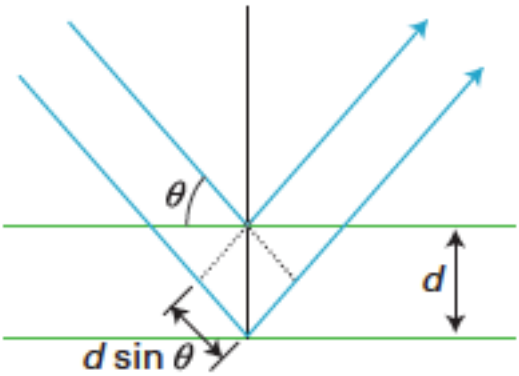

Figure 2.2: Derivation of Bragg's equation. Layers of atoms are treated as reflecting planes. X-rays interfere constructively when the path length, 2dsinϑ, equals an integral multiple of the wavelength, λ (Atkins et al., 2010).

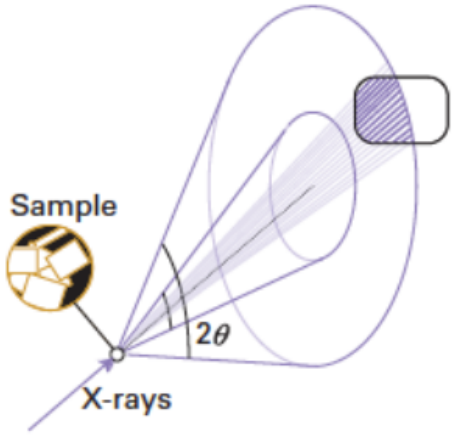

Figure 2.3: The diffraction cone that is a result of X-ray scattering by a powdered sample. The cone is made up of multiple diffraction spots from individual crystallites that merge together (Atkins et al., 2010).

In order to analyze the data, the positions of the cones need to be measured (Daan, 2000). This often done with a powder diffractometer, which an electronic detector that measures the angles of the diffracted beams (Atkins et al., 2010). A schematic diagram of the powder diffractometer is shown in Figure 2.4. The powder diffractometer consists of an X-ray tube which produces monochromatic X rays that can be rotated to produce angles from 0 to 90°. The sample is placed on a sample stage and irradiated by the X ray tube. An electronic detector detects the diffracted X-rays and it, too, is allowed to rotate to produce angles from 0 to 90° (Daan, 2000). By scanning the detector around the powdered sample along the circumference of a circle, it is made to cut through the diffraction cones at various diffraction maxima (Daan, 2000). The graph which is obtained, or the X-ray diffraction pattern, is illustrated in Figure 2.4 (Atkins et al., 2010). It displays intensity as a function of the detector angle, 2ϑ. The position and number of reflections depend on the crystal system, lattice type, cell parameters, and wavelength used to collect the data. On the other hand, the peak intensities depend on the types of atoms present in the crystal and their positions (Atkins et al., 2010). Crystalline solids have unique powder X-ray diffraction patterns in terms of the positions and intensities of the observed reflections (Daan, 2000). The effectiveness of this technique has led it to become the major technique for characterization of polycrystalline materials, such as MOFs.

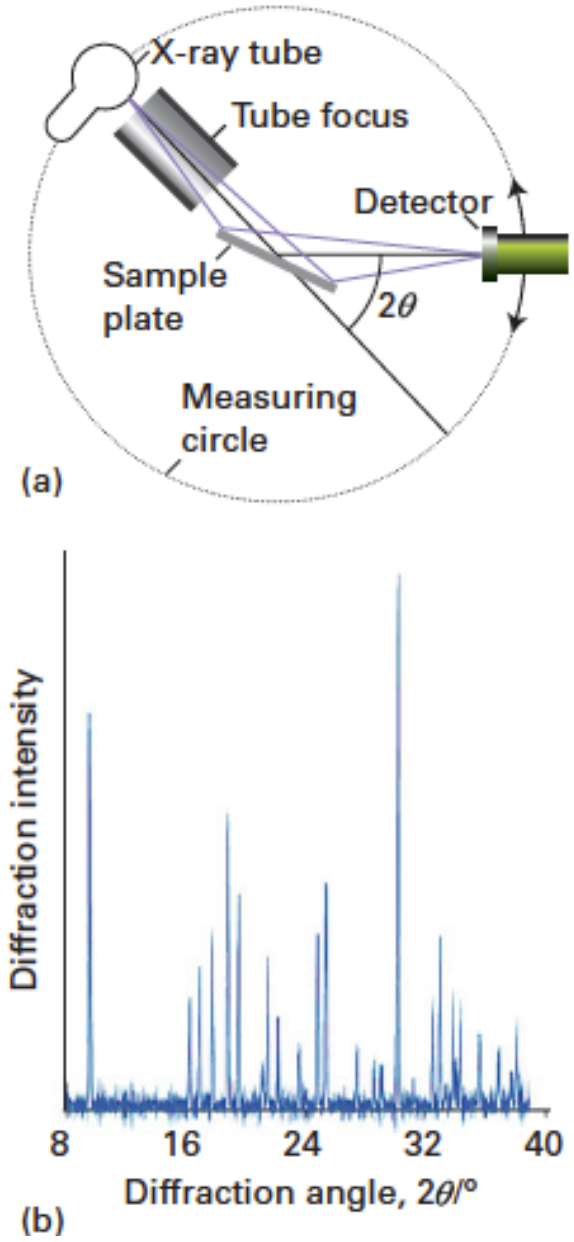

Figure 2.4: Powder diffractometer and powder diffraction pattern. (a) A schematic representation of a powder diffractometer. (b) A typical powder diffraction pattern displaying intensity as a function of the diffraction angle, 2ϑ. (Atkins et al., 2010).

2.4 Fourier Transform Infrared Spectroscopy

FTIR is a type of vibrational spectroscopy that can be used to determine the vibrational behavior of molecules. In FTIR, a molecule is irradiation with infrared light and the energy is absorbed if the frequency of the radiation matches the frequency of the vibration in the molecule. The result of this energy absorption is an increased amplitude for the vibration. Since each frequency absorbed by a molecule corresponds to a different molecular motion, it is possible to find out what the motions of the molecule are by measuring its IR spectrum. By further interpreting these motions, it is also possible to determine the kind of bonds, or functional groups, that are present in the molecule (McMurry, 2011). This is done by comparing the spectrum with reference tables, such as Table A below. FTIR can characterize compounds in terms of stiffness, number of bonds, and bond strength. This type of spectroscopy can also detect a fingerprint of compounds, determine the components of an unknown compound, and determine the structure of a compound (Atkins et al., 2010).

Table A

Functional Group	Absorption (cm^{-1})	Intensity	Functional Group	Absorption (cm^{-1})	Intensity
Alkane			Amine		
C–H	2850–2960	Medium	N–H	3300–3500	Medium
Alkene			C–N	1030–1230	Medium
–C–H	3020–3100	Medium	Carbonyl compound		
C–C	1640–1680	Medium	C–O	1670–1780	Strong
Alkyne			Aldehyde	1730	Strong
≡C–H	3300	Strong	Ketone	1715	Strong
C≡C	2100–2260	Medium	Ester	1735	Strong
Alkyl halide			Amide	1690	Strong
C–Cl	600–800	Strong	Carboxylic acid	1710	Strong
C–Br	500–600	Strong	Carboxylic acid		
Alcohol			O–H	2500–3100	Strong, broad
O–H	3400–3650	Strong, broad	Nitrile		
C–O	1050–1150	Strong	C≡N	2210–2260	Medium
Arene			Nitro		
C–H	3030	Weak	NO_2	1540	Strong
Aromatic ring	1660–2000	Weak			
	1450–1600	Medium			

Note: Characteristic IR absorption of some functional groups (McMurry, 2011)

The instrument used for FTIR is an infrared spectrometer, which consists of a light source, a sample holder, detector, and plotter. Modern spectrometers employ a single beam. First, a background scan is performed and then the sample and background is obtained. The instrument software is then able to subtract the background spectrum to give solely the sample spectrum (Anderson et al., 2011). Thus, FTIR is a method by which molecular vibrations are triggered through the irradiation of a molecule with infrared light and it provides information about the presence or absence of certain functional groups.

2.5 Ultraviolet-Visible Spectroscopy

UV-vis spectroscopy is a method which allows for the observation of the absorption of the absorption of electromagnetic radiation in the UV and visible light regions of the spectrum (Atkins et al., 2010). Generally, at room temperature molecules are in what is referred to as the ground state, or the lowest electronic energy level. Once a molecule is exposed to UV or visible light, electrons are promoted from the ground state to the excited electronic level. This electronic transition is accompanied by other transitions, such as vibrational or rotational (Anderson et al., 2004). Figure 2.5 is a schematic diagram of some of the possible molecular electronic transitions. Electron transfer processes can take place in transition metal ions (d-d transitions and ligand-to-metal or metal-to-ligand charge transfer transitions) as well and inorganic and organic molecules. Generally, energetically favored electronic promotion will occur from the HOMO to the LUMO, resulting in a species that is excited (McMurry, 2011).

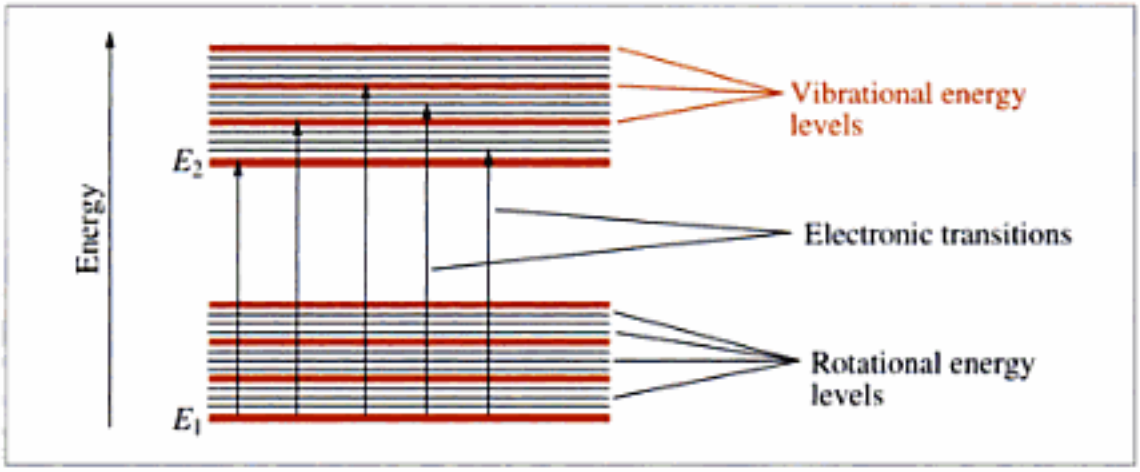

Figure 2.5: Possible molecular electronic transitions and vibrational and rotational energy levels (Anderson et al., 2004).

According to the Beer-Lambert Law (Equation 2.2), the absorbance (A) of a solution is proportional to the path length (l) and the concentration of the absorbing

molecule (c), where ε is the molar extinction coefficient, which is characteristic of the molecule (Anderson et al., 2004).

$$A = \varepsilon c l$$

Equation 2.2: Beer-Lambert Law (Anderson et al., 2004).

UV-vis is performed using an instrument called a UV-vis spectrometer. The spectrometer can be either double or single beam. In a double beam spectrometer, a beam of incident radiation is split into two. One of the beams passes through a cell that contains the sample dissolved in a solvent, whereas the other beam passes through a cell that contains only the solvent (Atkins et al., 2010). Single beam spectrometers work in a similar manner, but they measure the absorbance of a reference first, followed by the sample. A double beam spectrometer is illustrated in Figure 2.6.

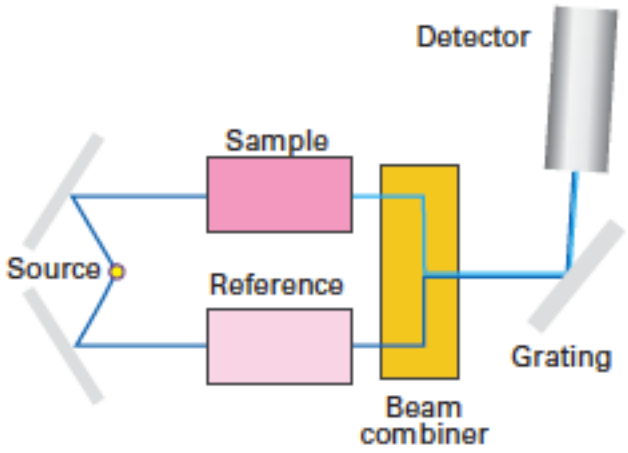

Figure 2.6: A UV-vis spectrometer (Atkins et al., 2010)

The intensity of the light transmitted through the solvent alone (Io) is compared to the intensity of the light transmitted through the sample (I). The absorbance can then be calculated with Equation 2.2 (Anderson et al., 2004):

$$A = \log_{10} \frac{I_0}{I}$$

Equation 2.3: The intensity of absorption is measured as the absorbance (A). Io is the incident intensity and I is the intensity after the light has passed through the sample (Anderson et al., 2004).

UV-vis has become an important analytic technique for MOF characterization. It allows for the measurement of the optical response of the photocatalytic materials (Laurier et al., 2013). Additionally, UV-vis spectroscopy is a convenient method of monitoring dye degradation by the MOF (Zhang & Lin, 2014). Thus, UV-vis spectroscopy is an important tool in the study of MOFs.

2.7 Bibliography

Anderson, R. J., Bendell, D. J., & Groundwater, P. W. (2004). *Organic spectroscopic analysis* (Vol. 22). Royal Society of Chemistry.

Atkins, P., Overton, T., Rourke, J., Weller, M., Armstrong, F., Hagerman, M. (2010). *Shriver & Atkins' Inorganic Chemistry*. New York, NY: W.H. Freeman and Company.

Czaja, A. U., Trukhan, N., & Müller, U. (2009). Industrial applications of metal–organic frameworks. *Chemical Society Reviews*, *38*(5), 1284-1293.

Daan, S. (2000). *Reactions and Characterization of Solids*. Cambridge, UK: The Royal Society of Chemistry.

Lee, Y. R., Kim, J., & Ahn, W. S. (2013). Synthesis of metal-organic frameworks: A mini review. *Korean Journal of Chemical Engineering*, *30*(9), 1667-1680.

McMurry, J. (2011). *Organic Chemistry*. Belmant, CA: Brooks Cole.

Rabenau, A. (1985). The role of hydrothermal synthesis in preparative chemistry. *Angewandte Chemie International Edition in English*, *24*(12), 1026-1040.

Stock, N., & Biswas, S. (2011). Synthesis of metal-organic frameworks (MOFs): routes to various MOF topologies, morphologies, and composites. *Chemical reviews*, *112*(2), 933-969.

Tranchemontagne, D. J., Hunt, J. R., & Yaghi, O. M. (2008). Room temperature synthesis of metal-organic frameworks: MOF-5, MOF-74, MOF-177, MOF-199, and IRMOF-0. *Tetrahedron*, *64*(36), 8553-8557.

Zhao, Y. G., Li, K. H., & Li, J. (2010). Solvothermal Synthesis of Multifunctional Coordination Polymers. *Z. Naturforsch., B: Chem. Sci*, *65*, 976-998.

Appendix 1B

Table 1: *Structure and nature of common organic dyes.*

Dye name	Chemical structures	Ionicity	Size (nm^3)	Absorption λ_{max} (nm)
Orange G (OG)	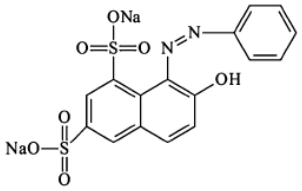	Anionic	1.62 × 0.94 × 0.29	484
Methyl Orange (MO)	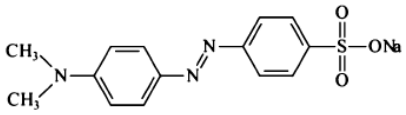	Anionic	1.54 × 0.48 × 0.28	467
Methylene Blue (MB)	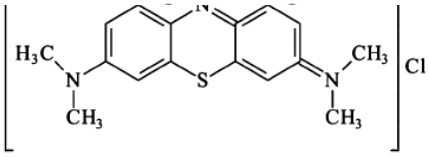	Cationic	1.38 × 0.64 × 0.21	672
Rhodamine B (RhB)	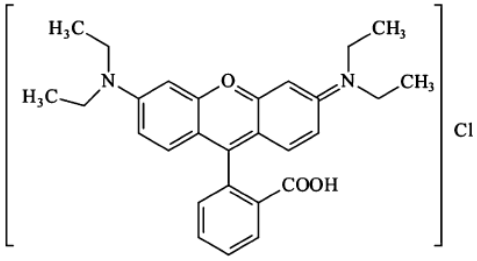	Cationic	1.56 × 1.35 × 0.42	552

Note. Common organic pollutants (Wang et al., 2014).

Table 2: Performances of some MOFs constructed with d-block metals as photocatalysts for the degradation of organic pollutants in aqueous media

MOF[a]	E_g (eV)	Irrigation	Organic pollutants	Initial concentration (mg L^{-1})	Time (min)	Degradation efficiency (%
MOF-5	3.40	UV	Phenol	40.0	180	50
MOF-5	3.40	UV	DTBP	40.0	180	100
$(emim)_2[InK(btec)_{1.5}(H_2O)_2]$	3.15	UV	MB	5	180	90
$(emim)[In_3(\mu_3\text{-}OH)_2(btec)_2]\cdot 2H_2O$	3.8	UV	MB	5	840	100
$Zn_3(btc)_2$ (thin film)	—	UV-vis	$MB(H_2O_2)$	10	60	99
MIL-88A	2.05	Vis	$MB(H_2O_2)$	32	20	100[c]
$[Zn_4(O)(tdc)_3(4,4'\text{-}bimb)_4]\cdot 5.25H_2O\cdot CH_3OH$	—	Vis	X3B	3.69	540	100[c]
NTU-9	1.74	Vis	$RhB(H_2O_2)$	47.9	80	100
NTU-9	1.74	Vis	$MB(H_2O_2)$	31.9	20	100
$[Cu^{II}(salimcy)](Cu^{I}I)_2\cdot DMF$	—	Vis	$MB(H_2O_2)$	12	22	96
$[Cu^{II}(salimcy)](Cu^{I}I)_2\cdot DMF$	—	Vis	$RhB(H_2O_2)$	12	50	95
$[Cu^{II}(salimcy)](Cu^{I}I)_2\cdot DMF$	—	Vis	$MO(H_2O_2)$	12	55	100
$Cu(Br\text{-}ip)(bitmb)(H_2O)$	—	Vis	$MY(H_2O_2)$	3.75	180	89
$(tpp)_2[Cd_3(4,4'\text{-}obb)_4]$	—	Vis	MB	3	360	98.5
$Cu(hfipbb)(2,2'\text{-}bpy)(H_2O)_2$	—	Vis	RhB	9.58	360	95
$Cu_2(hfipbb)_2(4,4'\text{-}bpy)(H_2O)$	—	Vis	RhB	9.58	360	70
$(Me_4N)_6[Cu_{12}(OMe)_6(pz)_6(btc)_6]\cdot 18H_2O$	—	UV	RhB	9.58	320	61
$(Me_4N)_6[Cu_{12}(OH)_6(pz)_6(btc)_6]\cdot 21H_2O$	—	UV	RhB	9.58	320	51
$[Cd(4,4'\text{-}bpy)(H_2O)_2(S_2O_3)]\cdot 2H_2O$	2.91	UV	MB	25	60	86[c]
$Cd_2(4,4'\text{-}bpy)_3(S_2O_3)_2$	2.75	UV	MB	25	60	84[c]
$Cd_2(4,4'\text{-}bpy)_{2.5}(S_2O_3)_2$	2.75	UV	MB	25	60	76[c]
$[Cd(4,4'\text{-}bpy)(H_2O)_2(S_2O_3)]\cdot 2H_2O$	2.91	UV	RBL	100	90	90[c]
$Cd_2(4,4'\text{-}bpy)_3(S_2O_3)_2$	2.75	UV	RBL	100	90	85[c]
$Cd_2(4,4'\text{-}bpy)_{2.5}(S_2O_3)_2$	2.75	UV	RBL	100	90	85[c]
$[Cd(4,4'\text{-}bpy)(H_2O)_2(S_2O_3)]\cdot 2H_2O$	2.91	UV	MV	100	90	99[c]
$Cd_2(4,4'\text{-}bpy)_3(S_2O_3)_2$	2.75	UV	MV	100	90	99[c]
$Cd_2(4,4'\text{-}bpy)_{2.5}(S_2O_3)_2$	2.75	UV	MV	100	90	99[c]
$[Cd(4,4'\text{-}bpy)(H_2O)_2(S_2O_3)]\cdot 2H_2O$	2.91	UV	MR	100	90	95[c]
$Cd_2(4,4'\text{-}bpy)_3(S_2O_3)_2$	2.75	UV	MR	100	90	95[c]
$Cd_2(4,4'\text{-}bpy)_{2.5}(S_2O_3)_2$	2.75	UV	MR	100	90	95[c]
$[Cd(3,3'\text{-}bpy)(H_2O)_2(S_2O_3)]\cdot 2H_2O$	2.91	UV	BBR	100	90	95[c]
$Cd_2(4,4'\text{-}bpy)_3(S_2O_3)_2$	2.75	UV	BBR	100	90	97[c]
$Cd_2(4,4'\text{-}bpy)_{2.5}(S_2O_3)_2$	2.75	UV	BBR	100	90	97[c]
$[Cd(4,4'\text{-}bpy)(H_2O)_2(S_2O_3)]\cdot 2H_2O$	2.91	Sunlight	MB	25	90	70[c]
$Cd_2(4,4'\text{-}bpy)_3(S_2O_3)_2$	2.75	Sunlight	MB	25	90	68[c]
$Cd_2(4,4'\text{-}bpy)_{2.5}(S_2O_3)_2$	2.75	Sunlight	MB	25	90	60[c]
$[Cd(4,4'\text{-}bpy)(H_2O)_2(S_2O_3)]\cdot 2H_2O$	2.91	Sunlight	RBL	100	90	95[c]
$Cd_2(4,4'\text{-}bpy)_3(S_2O_3)_2$	2.75	Sunlight	RBL	100	90	78[c]
$Cd_2(4,4'\text{-}bpy)_{2.5}(S_2O_3)_2$	2.75	Sunlight	MV	100	90	63[c]
$[Cd(4,4'\text{-}bpy)(H_2O)_2(S_2O_3)]\cdot 2H_2O$	2.91	Sunlight	MR	100	90	75[c]
$Cd_2(4,4'\text{-}bpy)_3(S_2O_3)_2$	2.75	Sunlight	MR	100	90	68[c]
$Cd_2(4,4'\text{-}bpy)_{2.5}(S_2O_3)_2$	2.75	Sunlight	MR	100	90	66[c]
$[Cd(4,4'\text{-}bpy)(H_2O)_2(S_2O_3)]\cdot 2H_2O$	2.91	Sunlight	BBR	100	90	90[c]
$Cd_2(4,4'\text{-}bpy)_3(S_2O_3)_2$	2.75	Sunlight	BBR	100	90	85[c]
$Cd_2(4,4'\text{-}bpy)_{2.5}(S_2O_3)_2$	2.75	Sunlight	BBR	100	90	84[c]
$Co_2(tkcomm)(llpd)_2$	1.98	UV	MB	16	90	81
$Mn_2(tkcomm)(llpd)_2$	3.09	UV	MB	16	90	88
$Zn_2(tkcomm)(llpd)_2$	3.26	UV	MB	16	90	78
$Cd_2(tkcomm)(llpd)_2$	3.31	UV	MB	16	90	87
Zn(1,4-bdc)(dpbpdca)·solvents	—	UV	RhB	5.0	810	85[c]
$Cu_4(dcpcpb)_2(\mu_3\text{-}OH)_2(CH_3OH)_2(H_2O)$	3.49	UV	MB	16	90	64
$Co_2(dcpcpb)(\mu_3\text{-}OH)(H_2O)_2$	2.96	UV	MB	16	90	73
$Cu_4(dcpcpb)_2(\mu_3\text{-}OH)_2(CH_3OH)_2(H_2O)$	3.49	UV	RhB	4.79	90	19
$Co_2(dcpcpb)(\mu_3\text{-}OH)(H_2O)_2$	2.96	UV	RhB	4.79	90	79
$Mn_2(ptp)_{4/3}(pbcpp)_2$	—	UV	MO	5.6	90	40
$[Cu_5(H_2tmbtmp)_2(btb)_2(OH)_2]\cdot 3H_2O$	—	UV	MB	10	120	59
Cd(tdc)(bix)(H_2O)	3.31	UV	MO	20	150	90
$Gd(H_2O)_3Co(2,3\text{-}pdc)$	—	UV	RBBR	100	90	88[c]

MOF[a]	E_g (eV)	Irrigation	Organic pollutants	Initial concentration (mg L^{-1})	Time (min)	Degradation efficiency (%)
$[Zn_2(4,4'\text{-bpy})](4,4'\text{-obb})_2$	4.02	UV	MB	100	100	72[c]
Cu(dm-bim)	2.49	Vis	MB	18.7	20	96
Cu(dm-bim)	2.49	Vis	RhB	18.7	34	100
Cu(dm-bim)	2.49	Vis	MO	18.7	45	95
$[Zn_4O(2,6\text{-ndc})_3(DMF)_{1.5}(H_2O)_{0.5}]\cdot 4DMF\cdot 7.5H_2O$	2.85	UV-vis	MO	20	120	65[c]
$[Zn_4O(2,6\text{-ndc})_3(DMF)_{1.5}(H_2O)_{0.5}]\cdot 4DMF\cdot 7.5H_2O$	2.85	Vis	MO	20	120	45[c]
$[Mn_3(btc)_2(4,4'\text{-bimb})_2]\cdot 4H_2O$	4.04	UV	X3B	3.69	600	65[c]
$[Mn_3(btc)_2(bimb)_2]\cdot 4H_2O$	4.04	Vis	X3B	3.69	600	15[c]
$[Co_3(btc)_2(bimb)_2]\cdot 4H_2O$	3.72	UV	X3B	3.69	600	100
$[Co_3(btc)_2(bimb)_2]\cdot 4H_2O$	3.72	Vis	X3B	3.69	600	70[c]
$[Zn_4(2\text{-mim})_6WO_4]\cdot 1.5DMF$ (HZIF-1W)	2.2	Vis	$MO(H_2O_2)$	16.35	120	24.5
$[Zn_4(2\text{-mim})_6MoO_4]\cdot 2DMF$ (HZIF-1Mo)	1.32	Vis	$MO(H_2O_2)$	16.35	120	81.6
Fe_3O_4@MIL-100(Fe)	—	UV-vis	MB	40	100	35
Fe_3O_4@MIL-100(Fe)	—	UV-vis	$MB(H_2O_2)$	40	100	99
Fe_3O_4@MIL-100(Fe)	—	Vis	MB	40	20	20
Fe_3O_4@MIL-100(Fe)	—	Vis	$MB(H_2O_2)$	40	200	99.77
MIL-53(Fe)	2.7	Vis	RhB	10	50	62.1
MIL-53(Fe)		Vis	$RhB(H_2O_2)$	10	50	100
$(Me_3Sn)_4Fe(CN)_6$	—	UV	MB	17.6	30	92
$[Co_2(1,4\text{-bdc})(ncp)_2]\cdot 4H_2O$	—	Vis	OG	45.2	300	67.59
$[Co_2(1,4\text{-bdc})(ncp)_2]\cdot 4H_2O$	—	Vis	RhB	47.9	300	67.52
$[Co_2(1,4\text{-bdc})(ncp)_2]\cdot 4H_2O$	—	Vis	MB	35.1	300	62.75
$[Co_2(1,4\text{-bdc})(ncp)_2]\cdot 4H_2O$	—	Vis	MV	40.8	300	33.29
$[Ni_2(4,4'\text{-bimb})_3(H_2O)_6]\cdot(aobtc)\cdot(DMF)_2\cdot(H_2O)_2$		Vis	X3B	3.69	540	70[c]
$[Cd(3,3',4,4'\text{-bptcH}_2)(H_2O)]\cdot(bimb)$		Vis	X3B	3.69	540	50[c]
$[Cu(3\text{-dpye})(3\text{-npa})(H_2O)]\cdot 3H_2O$	—	UV	MB	10	240	70[c]
$Cu(3\text{-dpye})_{0.5}(5\text{-aip})(H_2O)$	—	UV	MB	10	240	70[c]
$[Cu(3\text{-dpye})(1,3\text{-bdc})]\cdot 3H_2O$	—	UV	MB	10	240	80[c]
$Cu_3(3\text{-dpye})(1,2\text{-bdc})_2(\mu_2\text{-OH})_2$	—	UV	MB	10	240	64[c]
$Cu_3(3\text{-dpyb})(1,2\text{-bdc})_2(\mu_2\text{-OH})_2$	—	UV	MB	10	240	66[c]
$[Cu(3\text{-dpyh})_{0.5}(1,2\text{-bdc})]\cdot H_2O$	—	UV	MB	10	240	83[c]
$Cu(3\text{-dpyh})_{0.5}(5\text{-aip})(H_2O)$	—	UV	MB	10	240	66[c]
$[Co(3\text{-dpyh})(5\text{-Hip})(H_2O)_3]\cdot H_2O$	—	UV	MB	10	240	52
$[Co(3\text{-dpyh})(5\text{-nip})]\cdot H_2O$	—	UV	MB	10	240	39
$[Co(3\text{-dpyh})(5\text{-mip})]\cdot H_2O$	—	UV	MB	10	240	34
$[Co(3\text{-dpyh})_{0.5}(5\text{-aip})(H_2O)]\cdot 2H_2O$	—	UV	MB	10	240	47
$Co(btec)_{0.5}(4,4'\text{-bimb})$	2.68	Vis	X3B	3.69	540	80[c]
$Ni(btec)_{0.5}(bimb)$	2.63	Vis	X3B	3.69	540	80[c]
$Cd(btec)_{0.5}(bimb)_{0.5}$	2.32	Vis	X3B	3.69	540	90[c]
$Cd(3\text{-}NO_2\text{-bdc})(bbi)$	—	Vis	X3B	3.69	540	60
$Co(3\text{-}NO_2\text{-bdc})(bbi)$	—	Vis	X3B	3.69	540	80
$Cu(3\text{-dpyh})(3\text{-nph})(H_2O)_2$	—	UV	MB	10	120.	73
$Ni(3\text{-dpyh})(3\text{-nph})(H_2O)_2$	—	UV	MB	10	120	73
$Co(3\text{-dpyh})(3\text{-nph})(H_2O)_2$	—	UV	MB	10	120	85
$[Cu_9(OH)_6(bte)_2(sip)_4(H_2O)_3]\cdot 6H_2O$	—	UV	$MO(H_2O_2)$	10	280	76.1
$Cd(nddda)(H_2O)_2$	4.4	UV	MO	2.15	60	60[c]
Pb(nddda)(DMF)	4.3	UV	MO	2.15	60	62[c]
Cd(nddda)(phen)	3.8	UV	MO	2.15	60	81[c]
$Cd_5(nddda)_5(2,2'\text{-bpy})_2$	5.0	UV	MO	2.15	60	45[c]
$Cu_2(btec)(btx)_{1.5}$		Vis	$MO(H_2O_2)$	10	95	96.1
$Co_2(bip)_2(H_2O)$	—	UV	MB	10	180	79
$[Co(bip)(phen)(H_2O)]\cdot H_2O$	—	UV	MB	10	180	42
$[Co_2(1,4\text{-biyb})_2(2\text{-cmsn})_2(H_2O)]\cdot H_2O$	—	UV	MB	10	180	64
Cd(1,4-biyb)(2-cmsn)(H_2O)	—	UV	MB	10	180	37
[Zn(1,4-biyb)(2-cmsn)]$\cdot 2H_2O$	—	UV	MB	10	180	54
Cd(1,4-biyb)(adtz)(H_2O)	—	UV	MB	10	180	72
[Zn(1,4-biyb)(adtz)]$\cdot H_2O$	—	UV	MB	10	180	62
$[Ag_2(pdbmb)_2(CF_3SO_3)_2]\cdot H_2O$	3.03	UV-vis	MB	1000	540	90
$Fe_2(bhbdh)$	—	Vis	$RhB(H_2O_2)$	0.2	15	90
$Fe_2(bhbdh)$	—	Vis	$MB(H_2O_2)$	0.13	15	90

MOF[a]	E_g (eV)	Irrigation	Organic pollutants	Initial concentration (mg L^{-1})	Time (min)	Degradation efficiency (%)
$Pb_2(ttt)(ox)_{1/2}(H_2O)$	3.33	UV	MO	6.6	150	13
$Pb_3(ttt)_2(H_2O)_2$	3.32	UV	MO	6.6	150	13.7
$Cd(npdyda)(H_2O)_2$	4.4	UV	MO	4.9	60	60[c]
Pb(npdyda)(DMF)	4.3	UV	MO	4.9	60	60[c]
Cd(npdyda)(phen)	3.8	UV	MO	4.9	60	80[c]
$Cd_5(npdyda)_5(2,2'\text{-bpy})_2$	5.0	UV	MO	4.9	60	42[c]
$Zn(NH_2bdc)(bix)\cdot(DMF)_2$	—	Visible	X3B	3.69	540	98[c]
$[Cu_3(4\text{-bpah})_4(1,3,5\text{-btc})_2]\cdot 8H_2O$	—	UV	MB	10	240	50[c]
$[Cu_3(4\text{-bpah})_3(1,2\text{-bdc})_3(H_2O)_2]\cdot 4H_2O$	—	UV	MB	10	240	53[c]
$Cu(4\text{-bpah})(1,3\text{-bdc})(H_2O)$	—	UV	MB	10	240	54[c]
$Co(4\text{-bpah})(1,3\text{-bdc})(H_2O)$	—	UV	MB	10	240	25[c]
$Ni(4\text{-bpah})(1,3\text{-bdc})(H_2O)$	—	UV	MB	10	240	55[c]
$Zn(4\text{-bpah})(1,3\text{-bdc})(H_2O)$	—	UV	MB	10	240	55[c]
$Cd(4\text{-bpah})(1,3\text{-bdc})$	—	UV	MB	10	240	40[c]
$[Cd(3\text{-bpah})(1,3\text{-bdc}]\cdot H_2O$	—	UV	MB	10	240	65[c]
$[Cu_2(3\text{-bpah})(1,3\text{-bdc})_2]\cdot H_2O$	—	UV	MB	10	240	68[c]
$Ag_7(4,4'\text{-tmbpt})(Hcb\text{-}iso\text{-}p)_2(cb\text{-}iso\text{-}p)(H_2O)$	3.36	UV	MB	17.6	90	73
$[NaCd_3(4,4'\text{-tmbpt})(cb\text{-}iso\text{-}p)_2(OH)]\cdot H_2O$	3.44	UV	MB	17.6	90	65
$[Cd_3(3,4'\text{-tmbpt})_2(cb\text{-}iso\text{-}p)_2(H_2O)]\cdot 1.5H_2O$	3.50	UV	MB	17.6	90	54
$[Zn_4(dpcpbe)_2(\mu_3\text{-}OH)_2(H_2O)_{1.5}]\cdot 2H_2O$	3.49	UV	MB	3.2	90	32
$Zn_5Na(dpcpbe)_2(\mu_3\text{-}OH)_4(CH_3CH_2O)(H_2O)_2$	3.53	UV	MB	3.2	90	31
$[Cd_4(dpcpbe)_2(bime)_{0.5}(\mu_3\text{-}OH)_2(H_2O)_{1.5}]\cdot 2H_2O$	3.52	UV	MB	3.2	90	29
$Zn_4(dpcpbe)_2(bet)_{0.5}(\mu_3\text{-}OH)_2(H_2O)$	3.46	UV	MB	3.2	90	32
$Cu_6(\mu_3\text{-}O)(\mu_3\text{-}OH)(pz)_6(btc)$	—	UV	RhB	9.58	105	98
$Cd_2(bpe)_3(H_2O)_4(S_2O_3)_2$	2.53	UV	MR	100	90	50[c]
$Cd_2(bpe)_3(H_2O)_4(S_2O_3)_2$	2.53	UV	RBL	100	90	55[c]
$Cd(bpe)S_2O_3$	2.53	UV	MR	100	90	60[c]
$Cd(bpe)S_2O_3$	2.53	UV	RBL	100	90	62[c]
$[Co_2(tkcomm)(tkiymm)]\cdot 4.25H_2O$	3.78	UV	MB	17.6	75	95
$[Co_2(tkcomm)(tkiymm)]\cdot 4.25H_2O$	3.78	Vis	MB	3.51	300	49.6
$[Co_2(tkcomm)(tkiymm)]\cdot 4.25H_2O$	3.78	UV	RhB	9.58	600	66
$[Co_2(tkcomm)(tkiymm)]\cdot 4.25H_2O$	3.78	UV	X3B	3.69	600	56.7
$[Ni(sdb)(bitmb)(H_2O)]\cdot H_2O$	2.12	UV	$MY(H_2O_2)$	3.75	180	43.7
$[Cd(sdb)(bitmb)\cdot(H_2O)]\cdot(THF)(H_2O)$	3.89	UV	$MY(H_2O_2)$	3.75	180	24.7
$[Zn_2(sdb)_2(bitmb)]\cdot(THF)_2$	4.08	UV	$MY(H_2O_2)$	3.75	180	51.9
$Co_2(sdb)_2(bitmb)$	2.11	UV	$MY(H_2O_2)$	3.75	180	82.3
$[Cu_3(3\text{-dpsea})(1,3,5\text{-btc})_2(H_2O)_5]\cdot 4H_2O$	—	UV	MB	17.6	120	56
$[Cu(3\text{-dpyh})_{0.5}(1,4\text{-ndc})]\cdot H_2O$	—	UV	MB	17.6	120	67
Cu(ptz)(I)[b]	1.65	Vis	$MB(H_2O_2)$	18.7	24	98
Cu(ptz)(I)[b]	1.65	Vis	$RhB(H_2O_2)$	18.7	35	100
Cu(ptz)(I)[b]	1.65	Vis	$MO(H_2O_2)$	18.7	45	95
Cu(ptz)(II)[b]	2.24	Vis	$MB(H_2O_2)$	18.7	24	85[c]
Cu(ptz)(II)[b]	2.24	Vis	$RhB(H_2O_2)$	18.7	35	70[c]
Cu(ptz)(II)[b]	2.24	Vis	$MO(H_2O_2)$	18.7	45	70[c]
MIL-53(Fe)	2.72	UV-vis	MB	140	40	11
MIL-53(Fe)	2.72	Vis	MB	140	40	30
MIL-53(Fe)	2.72	UV-vis	$MB(H_2O_2)$	140	20	99
MIL-53(Fe)	2.72	Vis	$MB(H_2O_2)$	140	20	20
MIL-53(Al)	3.87	UV-vis	MB	140	60	30
MIL-53(Cr)	3.20	UV-vis	MB	140	60	32
Cu/ZIF-67	1.95	Vis	MO	16.35	25	100
$[Co_2(4,4'\text{-bpy})](4,4'\text{-obb})_2$	3.11	UV	OG	100	100	90[c]
$[Co_2(4,4'\text{-bpy})](4,4'\text{-obb})_2$	3.11	UV	RhB	100	100	62[c]
$[Co_2(4,4'\text{-bpy})](4,4'\text{-obb})_2$	3.11	UV	RBBR	100	100	100[c]
$[Co_2(4,4'\text{-bpy})](4,4'\text{-obb})_2$	3.11	UV	MB	100	100	85[c]
$[Ni_2(4,4'\text{-bpy})](4,4'\text{-obb})_2\cdot 2H_2O$	3.89	UV	OG	100	100	85[c]
$[Ni_2(4,4'\text{-bpy})](4,4'\text{-obb})_2\cdot 2H_2O$	3.89	UV	RhB	100	100	47[c]
$[Ni_2(4,4'\text{-bpy})](4,4'\text{-obb})_2\cdot 2H_2O$	3.89	UV	RBBR	100	100	95[c]
$[Ni_2(4,4'\text{-bpy})](4,4'\text{-obb})_2\cdot 2H_2O$	3.89	UV	MB	100	100	80[c]
$[Zn_2(4,4'\text{-bpy})](4,4'\text{-obb})_2$	4.02	UV	OG	100	100	70[c]
$[Zn_2(4,4'\text{-bpy})](4,4'\text{-obb})_2$	4.02	UV	RhB	100	100	43[c]
$[Zn_2(4,4'\text{-bpy})](4,4'\text{-obb})_2$	4.02	UV	RBBR	100	100	80[c]

Note. Some examples of MOFs as photocatalysts (Wang et al., 2014).

Table 3: *Iron(III) based MOFs.*

MOF	Linker	Finding	Reference
MIL-53, MIL-88, MIL-101, MIL-53(Fe)_NH2 , MIL-88B(Fe)_NH 2, MIL-101(Fe)_NH2	2-aminoterephthalic acid	Found the most important conditions for the synthesis of different hybrid phases. These included: the nature of the reaction medium, concentration of the solvent, the temperature.	(Bauer et al., 2008)
MIL-88(Fe)	Fumeric acid	Report very large swelling of the structure.	(Draznieks et al., 2005)
MIL-100(Fe)	benzene tricarboxylic or trimesic acid	Friedel–Crafts benzylation catalytic tests indicate a high activity and selectivity for this MOF.	(Horcajada et al., 2007)
MIL-88B, MIL-88D	Terephtalic acid, 4,40 -biphenyl dicarboxylate	Swelling behavior is affected in two ways. There is a decrease in breathing amplitude proportional to the size and number of functional groups. Second, introducing functional groups facilitates swelling in liquid phases.	(Horcajada et al., 2011)
MIL-100(Fe), MIL-101(Fe)_NH_2, MIL-88B(Fe), MIL-88B(Fe)_NH_2	Terephtalic Acid, 2-aminoterephtalic acid	Degradation of Rhodamine 6G. Amino substitution of the linker did not result in enhanced photocatalytic activity.	(Laurier et al., 2013)
MIL-88B, NH_2 - MIL-88B	Terephtalic Acid, 2-aminoterephthalic acid	Flexibility in both frameworks was observed; however, it differed for the two materials depending on the solvent.	(Ma et al., 2013)
MIL-88B(Fe)_NH 2	2-aminoterephthalic acid	Acetic acid found to control the size and aspect ratio of the materials.	(Pham et al., 2011)
MIL-100(Fe)	trimesic acid	MOF shows some excellent catalytic properties in acetalization.	(Zhang et al., 2015)
MIL-88B(Fe)_NH_2	2-aminoterephthalic acid	MOF showed high stability and efficiency for the photocatalytic Cr(VI) reduction under visible-light irradiation	(Shi et al., 2015)

MOF	Linker	Finding	Reference
MIL-88(Fe)_NH2	2-aminoterephthalic acid	The MOF exhibited peroxidase activity. It was used to quickly catalyze oxidation of the peroxidase substrate to produce a colored product. This is a simple, sensitive and selective method for the colorimetric detection of glucose.	(Liu et al., 2013)

Note: Some recent research on iron based MOFs with iron(III) metal nodes.